Tesis Doctoral

Estudio de la tasa de reacción 30P(alfa, p)33S de interés astrofísico en erupciones de rayos X

Figueira, Juan Manuel

2012

UNIVERSIDAD DE BUENOS AIRES

Facultad de Ciencias Exactas y Naturales

Departamento de Física

Estudio de la tasa de reacción ^{30}P(α,p)^{33}S de interés astrofísico en erupciones de rayos X

Tesis presentada para optar por el título de Doctor
de la Universidad de Buenos Aires en el área Ciencias Físicas

Juan Manuel Figueira

Director de Tesis: Dr. Jorge O. Fernández Niello

Consejera de Estudios: Dra. Cristina Caputo

Lugar de Trabajo: Laboratorio TANDAR, Comisión Nacional de Energía Atómica

Buenos Aires, 2012

Estudio de la tasa de reacción ^{30}P(α,p)^{33}S de interés astrofísico en erupciones de rayos X

RESUMEN

Los procesos que ocurren en la superficie de una estrella de neutrones durante erupciones de rayos X incluyen cientos de reacciones (p, γ) y (α, p) diferentes, la mayoría de las cuales involucran núcleos radiactivos de corta vida media. Las estimaciones de la mayoría de las tasas de reacción están aún basadas en cálculos realizados utilizando el modelo estadístico de Hauser-Feshbach, ya que en el pasado no eran posibles las mediciones directas de estas reacciones. Sin embargo, la aplicabilidad de un tratamiento estadístico con núcleos de masa liviana y media es cuestionable. Únicamente en los últimos años los haces de núcleos radioactivos se han vuelto accesibles experimentalmente y se han llevado a cabo las primeras mediciones directas de este tipo de reacciones. Debido a que las intensidades de los haces disponibles en las instalaciones actuales de haces radiactivos siguen siendo 3–5 órdenes de magnitud menores que las disponibles con haces estables, estas mediciones no pueden aún llevarse a cabo en el rango de energías astrofísicas. En consecuencia los experimentos son realizados a mayores energías, y luego se extrapolan a la región de interés. Otras dificultades se originan debido la a presencia de impurezas en el haz, que a veces pueden incluso ser la parte dominante del mismo. Por estas razones es necesario que sean desarrolladas técnicas experimentales novedosas. En este trabajo se desarrolló una nueva técnica utilizando un espectrómetro magnético lleno de gas, la cual permite el estudio de reacciones (α, p) de interés astrofísico en cinemática inversa y por medio de las reacciones temporales inversas. Además se midieron las secciones eficaces de la reacción ^{30}P$(\alpha, p)^{33}$S, de relevancia en modelos de nucleosíntesis en explosiones de rayos X, en el rango de energía $E_{\mathrm{c.m.}} = 2{,}83$ a $4{,}38$ MeV y se compararon con cálculos de Hauser-Feshbach. Las secciones eficaces experimentales resultaron ser un factor de alrededor de 7 a 8 menores que los resultados teóricos. A partir de estas secciones eficaces experimentales, se calculó

la tasa de reacción estelar en función de la temperatura en el rango de aproximadamente 0,1–10 GK relevante para las erupciones de rayos X. Se discuten las posibles consecuencias para la nucleosíntesis en ese tipo de erupciones.

Palabras claves: Tasa de la reacción ^{30}P(α,p)^{33}S; Sección eficaz de la reacción ^{30}P(α,p)^{33}S; nucleosíntesis explosiva; erupciones de rayos X; técnica de espectroscopía de partículas.

Study of the ^{30}P(α,p)^{33}S reaction rate of astrophysical interest in X-ray bursts

ABSTRACT

The processes occurring on the surface of a neutron star during X-ray bursts usually include hundreds of different (p, γ) and (α, p) reactions, the majority involving short-lived radioactive nuclei. The estimates of most reaction rates are based on statistical Hauser-Feshbach calculations since direct measurements of these reactions were not possible in the past. The applicability of a statistical treatment for light and medium mass nuclei, however, is questionable. Only in recent years have beams of short-lived nuclei become experimentally accessible and the first direct measurements of these reactions been performed. Because the beam intensities available at existing radioactive beam facilities are still 3–5 orders of magnitude smaller than what is available with stable beams, these measurements can not yet be done at astrophysical energies. Consequently experiments are usually studied at higher energies, which are then extrapolated into the region of interest. Other difficulties originate from the presence of beam impurities which sometimes can be the dominant part of the incident beam. For these reasons novel experimental techniques need to be developed. In this work, a new technique has been developed using a gas-filled magnetic spectrograph which enables the study of (α, p) reactions of astrophysical interest in inverse kinematics and by means of the time-reverse reactions. Using this technique, cross sections of the ^{30}P$(\alpha, p)^{33}$S reaction, relevant to X-ray burst nucleosynthesis models, were measured in the energy range $E_{\mathrm{c.m.}} = 2.83$–4.38 MeV and compared with Hauser-Feshbach calculations. The experimental cross sections were found to be a factor of around 7–8 smaller than the theoretical results. From these experimental cross sections, the stellar reaction rate was calculated as a function of temperature in the range relevant to X-ray bursts of about 0.1–10 GK. Possible implications for nucleosynthesis in X-ray bursts are discussed.

Keywords: ^{30}P(α,p)^{33}S reaction rate; ^{30}P(α,p)^{33}S cross section; explosive nucleosynthesis ; X-ray bursts; particle spectroscopy technique.

ACKNOWLEDGMENTS

Firstly, I would like to thank Jorge Fernández Niello, my director, for giving me the opportunity to do this work and having confidence in me. It is also a pleasure to thank Ernst Rehm, who supervised me during my stay at Argonne National Laboratory. Without their knowledge and guidance this work would not have been possible. They transmitted to me their continued enthusiasm and provided support on many occasions. I am indebted to them for all they have taught me. It was a pleasure to have shared these years with them.

I am deeply grateful to Cristina Caputo for her advice and Anna Elizabeth Woodard for her insightful comments and invaluable help.

I would also like to thank the operation staff of ATLAS accelerator and collaborators who participated in the experiment at ANL, Catherine Deibel, John Greene, Cheng-Lie Jiang, Hye Young Lee, Scott Marley, Richard Pardo, Nidhi Patel, Michael Paul, Claudio Ugalde and Gary Zinkann. Also to Andrés Arazi, Christian Balpardo, Oscar Capurro, María Angélica Cardona, Patricio Carnelli, Ezequiel de Barbará, Daniel Hojman, Guillermo Martí, Diego Martinez Heimann, Alberto Pacheco, and Darío Rodrigues, all of whom are from the Department of Experimental Physics at TANDAR Laboratory, and Paulo Gomes and Jesus Lubian from the Department of Physics at Fluminense Federal University, who have helped me numerous times.

Finally, I thank my family, friends and colleagues for the support they have given to me throughout my PhD.

This work was supported by the *Consejo Nacional de Investigaciones Científicas y Técnicas* (Argentina), by the *Comisión Nacional de Energía Atómica* (Argentina), by the US Department of Energy, Office of Nuclear Physics under contract No. DE-AC02-06CH11357, and by the National Science Foundation JINA Grant No. PHY0822648.

CONTENTS

I. INTRODUCTION

Explosive nucleosynthesis in the Universe takes place in very different kinds of astrophysical environments. These explosive events cover a huge range in energy release and are characterized by large amounts of expelled matter, extreme physical conditions of temperature and density, and relatively short durations, which may vary from seconds to a few hours or days. They involve solitary stars in different stages of their evolution (e.g., stellar outbursts, eruptive supergiants, core-collapse supernovae) or binary systems of stars bound by gravitational attraction (e.g., novae, type I supernovae, X-ray bursts and γ-ray bursts).

Whereas nuclear reactions in quiescent stars like the Sun are accountable for the synthesis of most elements up to iron [1], those occurring in explosive conditions contribute considerably to the overall nucleosynthesis of the heavy elements from iron to uranium in the Universe. Indeed, the National Research Council of the National Academy of Sciences (USA) has recently stated in a report [2] that the origin of heavy nuclei in the mass region beyond iron remains one of the eleven greatest unanswered questions of modern physics.

Although the general mechanisms of most explosive events are well understood, many important questions remain unanswered. In the case of X-ray bursts (hereafter, XRBs), for example, much work remains to fully explain the time length of the burst, the way and degree to which they contribute to galactic nucleosynthesis, and the cause of superbursts (which are up to a thousand times

more powerful and longer than normal XRBs). Finding solutions to these problems will require a collective effort from both the astrophysical and the nuclear physics communities.

The past twenty years has seen rapid evolution in observational astronomy, including ground-based telescopes with improved spectroscopic resolution and new space-based instruments. At the same time, the development of radioactive ion beam facilities and other advances in experimental nuclear physics have provided new tools for examining the properties of exotic nuclei, and crucial progress has been made in stellar modelling. Taken together, these advances have made possible an era of unprecedented progress in nuclear astrophysics.

A large part of the about 3000 known nuclides are implicated in nuclear processes occurring in explosive events. From an astrophysical perspective not all of these nuclear reactions have the same importance. Key processes are recognized by studying the sensitivity of astrophysical models to nuclear input parameters, particularly reaction rates [3].

Reactions in the intermediate-mass region $A \sim 20$–40 are of interest to nuclear astrophysics for studies of novae and XRBs. Specifically in XRBs, the nuclear flow is driven by the triple-α reaction, the rp-process and the αp-process toward the proton-drip line [4]. As the nuclear flow occurs far from the valley of stability, there is little to no experimental information available on many of the reaction rates of these processes.

The αp-process, sequences of (α, p) and (p, γ) reactions in the $A \sim 20$–40 region, is strongly temperature (energy) dependent due to the large Coulomb barriers involved. As a result, the cross sections and the related reaction rates can have a large effect on nucleosynthesis in XRBs. Parikh *et al.* [5] have shown that models which predict the isotopic abundances of nuclei created in XRBs

are very sensitive to variations in specific reaction rates. Specifically, some (α, p) reactions on intermediate-mass waiting points (e.g., ^{22}Mg, ^{26}Si, ^{30}S, and ^{34}Ar) may significantly affect XRB nucleosynthesis [6]. These reactions involve short-lived nuclei in both the entrance and exit channel and, therefore, they have not been studied extensively in the laboratory since radioactive ion beams with sufficient intensity are not yet available. In order to measure these reaction rates time-inverse (p, α) reactions in inverse kinematics can be employed, using radioactive beams of ^{25}Al, ^{29}P, ^{33}Cl and ^{37}K.

In this work, the reaction $^{33}\mathrm{S}(p, \alpha)^{30}\mathrm{P}$ has been employed for the development of a technique to be used in the measurement of reactions involving radioactive beams. The benefit of using the $^{33}\mathrm{S}(p, \alpha)^{30}\mathrm{P}$ reaction stems from two facts: *i*) the technique can be developed using a ^{33}S stable beam and *ii*) the reverse reaction $^{30}\mathrm{P}(\alpha, p)^{33}\mathrm{S}$, which plays an important role in XRB nucleosynthesis, has not yet been studied experimentally. Sensitivity studies showed that varying the nominal rate of this reaction by a factor of ten up or down affects the yield of four different nuclei, ^{30}Si, ^{31}P, ^{33}S and ^{36}Cl, by at least a factor of two [5]. Because of the lack of experimental data, the $^{30}\mathrm{P}(\alpha, p)^{33}\mathrm{S}$ reaction rate used in XRB calculations so far is based only on theoretical estimates, which may be incorrect. It was therefore important to obtain cross sections of this reaction experimentally.

In the next chapter, the main features of the astrophysical scenarios of interest to this work, X-ray bursts, and the explosive nucleosynthesis taking place in them, are described. General characteristics of thermonuclear reactions are outlined in Chapter III. The technique developed to measure (α, p) reactions is presented in Chapter IV. The obtained cross sections for the ground-state-to-ground-state $^{33}\mathrm{S}(p, \alpha)^{30}\mathrm{P}$ and $^{30}\mathrm{P}(\alpha, p)^{33}\mathrm{S}$ reactions are given

in Chapter V. In Chapter VI the stellar rate for the latter reaction is presented. Finally, a conclusion is given in Chapter VII.

II. TYPE I X-RAY BURSTS

II.1. Characteristics

Type I X-ray bursts are thermonuclear explosions which take place in binary systems, pairs of bound stars that orbit around a common center of gravity. X-ray binaries are among the brightest extra-solar objects and constitute the brightest class of X-ray sources in the sky. They are characterized by a dramatic variation in brightness on timescales ranging from seconds to minutes, in contrast to standard transient sources characterized by lifetimes ranging from weeks to months. These bursts have typical durations of about 10–100 s with recurrence times on the order of a few hours to several days. Their main source of power is the gravitational energy released by matter accreted from a companion star and falling onto a neutron star in a close binary system. As the accreted hydrogen-rich matter builds up on the surface of the neutron star the temperature increases and a thermonuclear runaway occurs reaching peak temperatures of $T_9 = 1$–2 (where T_9 stands for the temperature given in 10^9 K). Type I XRBs are the most frequent type of thermonuclear stellar explosion in the galaxy, the third in terms of total energy output after supernovae and classical novae [4, 7–11].

Belian *et al.* [12] and Grindlay *et al.* [13] independently discovered XRBs in 1975. Belian *et al.* reported bursting events from X-ray observations of sources located in the Norma constellation using the two military Vela-5 satellites. Sim-

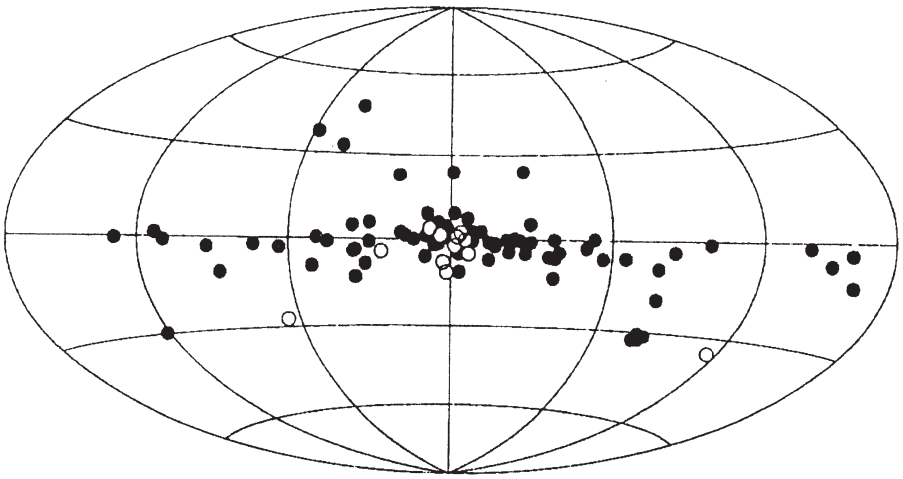

FIG. 1: Sky map (in galactic coordinates) of the LMXBs. Globular cluster sources are indicated by open circles. The 27 LMXBs within 2° of the galactic center have not been included to avoid congestion of the map. The map is based on the catalog of Van Paradijs (1995) [19]. Figure taken from Ref. [20]

ilarly, Grindlay *et al.* reported two events on the X-ray source 3U 1820-30, situated in the globular cluster NGC 6624, which were observed using the Astronomical Netherlands Satellite. A year later, three other burst sources were identified within a few degrees of the galactic center by Lewin *et al.* [14], one of them the enigmatic Rapid Burster (XBT 1730-335). To date, more than 90 galactic X-ray bursters have been identified [15].

The possibility that XRBs are caused by thermonuclear runaways occurring on the surface of an accreting neutron stars was suggested by Woosley and Taam [16], and independently by Maraschi and Cavaliere in 1976 [17]. However, the rapid progression of flashes shown by the Rapid Burster, with recurrence times as short as about 10 s, could not be explained by means of thermonuclear explosions and were found to have a different nature [18]. Thus, a classification of type I and type II bursts was established for events originated by thermonuclear runaways and accretion instabilities, respectively.

Type I XRBs are a subset of low mass X-ray binaries (LMXBs). Type I XRBs and LMXBs have the same spatial distribution, both being concentrated towards the galactic center as shown in Fig. 1. XRBs are also found in globular clusters. Recently, the first extragalactic XRBs were discovered in two candidates for globular cluster sources in the Andromeda galaxy (M31) [21]. As they are located outside regions of active star formation, these XRBs have been identified as members of an old stellar population [7]. This is also consistent with the fact that the donor transferring matter onto the neutron star is a faint, low-mass star ($M \lesssim 1\ M_{\odot}$), either a main sequence or a red giant star.

When a binary system is described using a coordinate system which rotates fixed to the line joining the objects, the gravity and centrifugal force cause that the maximum of the potential energy is reached on a figure-eight equipotential surface with one of the two stars at the center of a lobe, as shown schematically in Fig. 2(a). These lobes are called Roche lobes, which represent the gravitational domain of each star. When the donor star fills its Roche lobe, it begins to transfer matter to the neutron star, as represented in Fig. 2(b). The falling matter comes from the envelope of the donor star and is rich in hydrogen and helium. Due to angular momentum conservation, the falling material establishes an accretion disk surrounding the neutron star, as represented artistically in Fig. 3. Due to the high gravitational fields of compact stars, the accreted material accelerates rapidly as it spirals down to the surface of the neutron star. The falling matter collects on the surface and is compressed as additional material falls on top of it. It changes state, first forming part of a liquid ocean on the surface of the star, and eventually joining the solid crust beneath it. Due to the degenerate conditions prevailing on the surface of the neutron star, another consequence of the high gravitational fields, matter does not follow the ideal gas law. Hence,

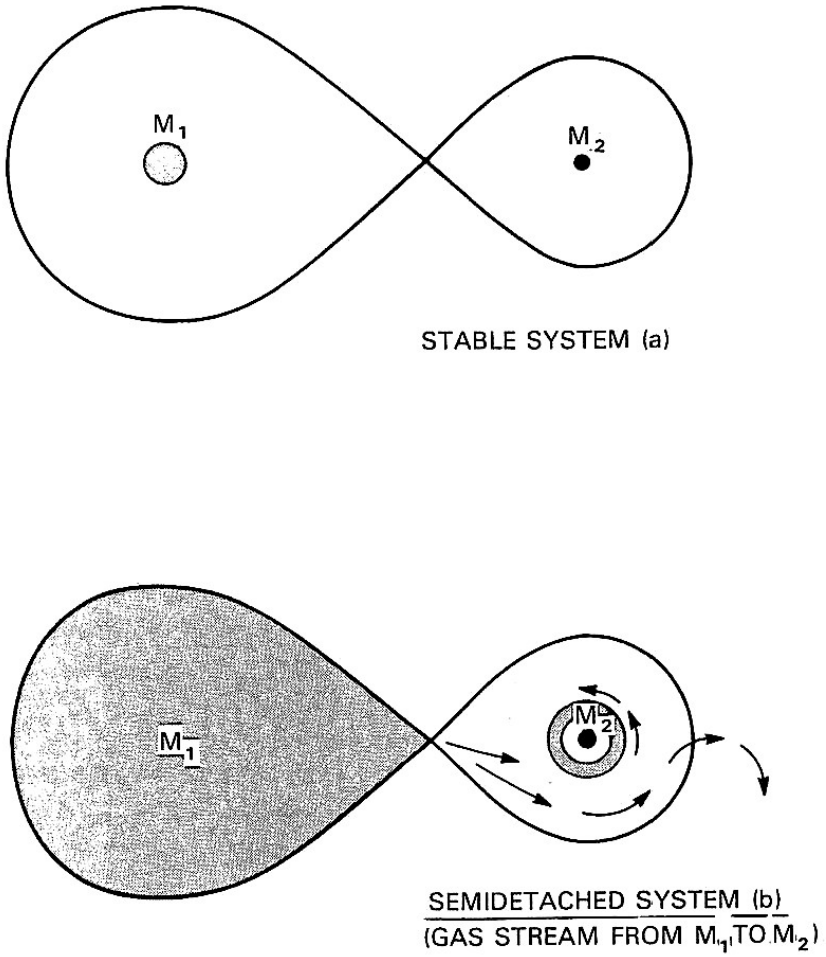

FIG. 2: Schematic diagrams of a binary system formed by two stars of masses M_1 and M_2, with $M_1 > M_2$. The solid line is the critical Roche surface, where the attraction towards the two stars is equal. (a) Top: If the stellar matter is within the critical surface, the system is stable and there is no material transfer. (b) Bottom: If the more massive star expands so as to fill its Roche lobe, the system is semidetached, and further expansion produces a material flow towards the less massive star. Figure taken from Ref. [22]

the accumulation of matter causes a temperature increase. Eventually a thermal instability in a thin shell is produced by the ignition of very temperature sensitive fusion reactions and the heating from these exothermic thermonuclear reactions cannot be compensated by readjusting the stellar structure or cooling through the surface [23].

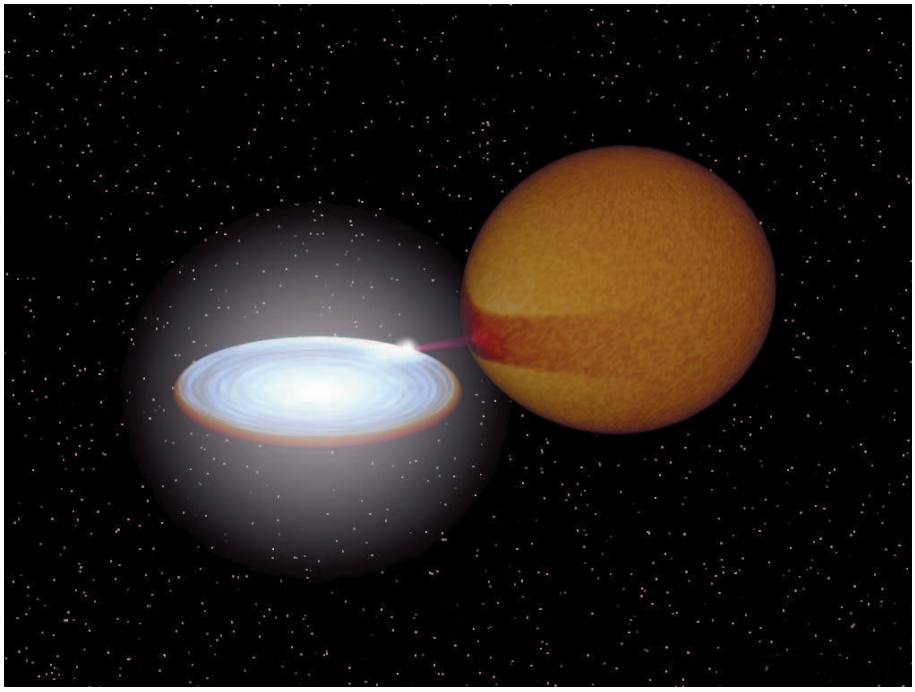

FIG. 3: Artistic impression of an X-ray binary. Taken from Ref. [20].

As a result a thermonuclear runaway takes place: rising temperatures accelerate the thermonuclear reaction rates leading to more rapid temperature rises, still faster thermonuclear reactions and so on [4]. During the thermonuclear explosion, densities and temperatures of $\rho \sim 10^6$ g/cm^3 and $T_9 \sim 1$–2 can be reached, respectively [24–26], and an XRB is produced by thermal emission. As accretion resumes, the process is repeated and bursts are recurrent.

Observationally, the XRB is characterized by a fast rise in luminosity lasting 1–10 s, followed by a slower exponential-like decline lasting 10–100 s, as shown in Fig. 4. Typically, the peak luminosity is about 3×10^{38} erg/s and the total energy release is about 10^{39-40} erg [7, 27–29]. The burst repetition times are of the order of hours to days and long successions of bursts can be observed [4].

The first evidence of the thermonuclear origin of type I XRBs came from lightcurve analysis, in particular the so-called α value, which is the ratio of en-

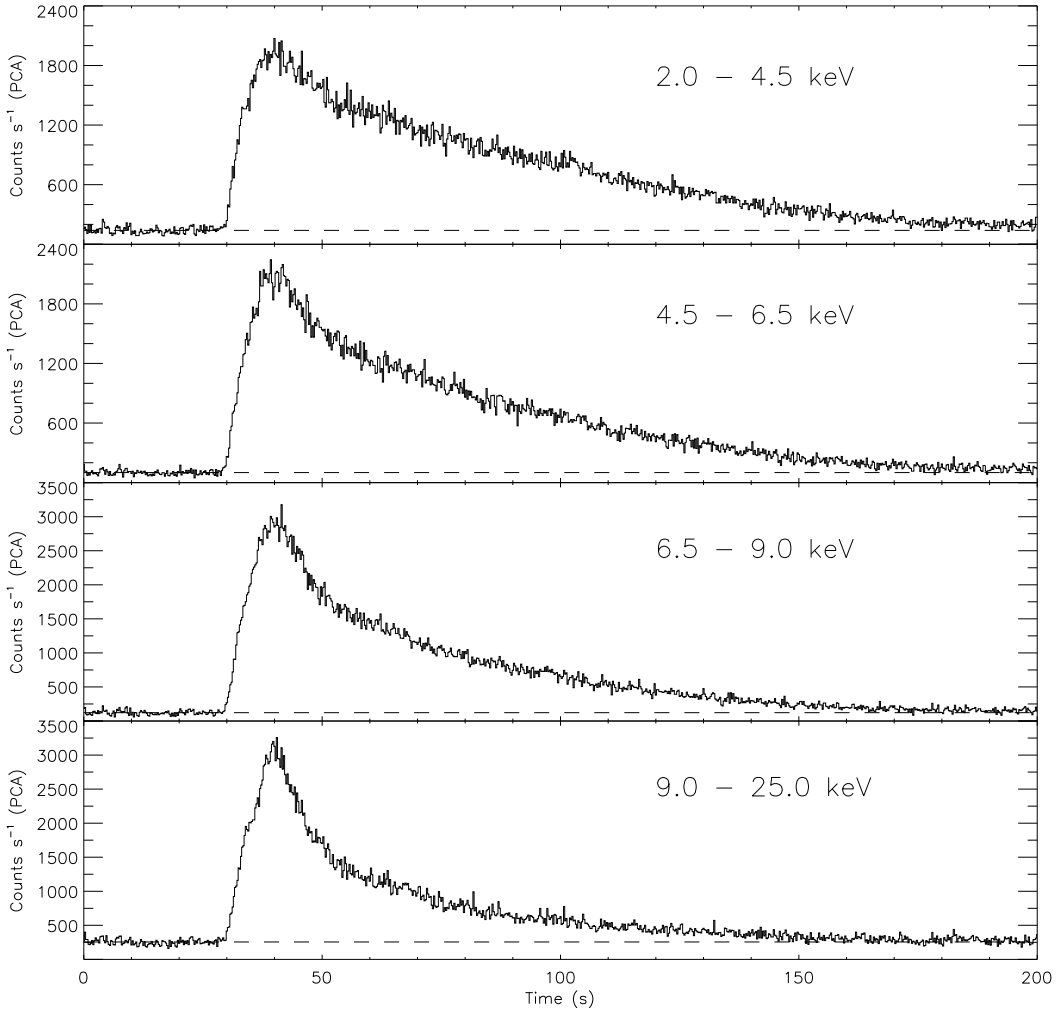

FIG. 4: X-ray burst from the source GS 1826-238 seen with the satellite Rossi X-ray Timing Explorer (RXTE) shown in four different energy bands: 2.0–4.5 keV, 4.5–6.5 keV, 6.5–9.0 keV and 9.0–25.0 keV. The dashed lines indicate the persistent flux levels in between bursts. Figure taken from Ref. [10]

ergy released in between bursts ($E_{\rm persistent}$) to the energy released during bursts ($E_{\rm burst}$). The gravitational potential energy released by matter falling onto a neutron star during the accretion stage, which causes the persistent X-ray emission, can be estimated by $E_{\rm persistent} \sim GM_{\rm NS}/R_{\rm NS}$ (where G corresponds to the universal gravitation constant, and $M_{\rm NS}$ and $R_{\rm NS}$ to the mass and radius of the neutron star, respectively), typically about 200 MeV/nucleon. The nuclear en-

ergy released during the XRB is $E_{\rm busrt} \sim 5$ MeV/nucleon for a solar mixture transformed into Fe-group nuclei. The ratio $E_{\rm persistent}/E_{\rm burst}$ match the values measured for α, in the range of about 40–100.

It has been shown that XRBs have thermal blackbody spectra [30, 31]. Hence, measurement of the bolometric fluxes and blackbody temperatures can be used to deduce radii if the distance is known. Radii obtained in this way are typically in the range of about 10 km, consistent with the theoretical size of a neutron star. Although XRB spectra are well described by the Planck function, they are theoretically expected to be harder than a blackbody at the effective temperature of its surface due to the dominance of scattering in the atmosphere of the neutron star [32–36].

II.2. X-ray burst nucleosynthesis

The main nuclear reaction path in XRB nucleosynthesis has been largely discussed in the literature [4, 6, 26, 37–44]. The most interesting nucleosynthesis is attained for mixed hydrogen–helium bursts due to the complex nuclear reaction interplay that the mixture causes [6, 42].

During hydrostatic burning, if several different nuclei are present in the stellar plasma, usually those reactions with the smallest Coulomb barrier will account for the majority of the nuclear energy generation and nucleosynthesis. As will be seen in this section, in explosive environments such as XRBs, where the stellar temperature is large enough for hydrogen and helium to burn in the same place, interesting effects occur. At such high temperatures the nucleosynthesis is sensitive to several effects which do not play a central role in hydrostatic

burning.

Most X-ray binaries accrete a blend of hydrogen, helium and some heavy metals most likely in solar proportions $X_{\rm H} = 0.71$; $X_{\rm He} = 0.271$; $X_{\rm O} = 0.0097$; $X_{\rm C} = 0.0040$; $X_{\rm N} = 0.00096$; $X_{\rm Si} = 0.00099$; $X_{\rm Mg} = 0.00076$, $X_{\rm Ne} = 0.00058$; $X_{\rm Fe} = 0.0014$; $X_{\rm S} = 0.00040$ (where X_i stands for the mass fraction of the element i in the sun [45, 46]) at mass accretion rates larger than $4.4 \times 10^{-10} M_{\odot}$/yr. In these cases, XRBs are triggered by the temperature-sensitive triple-α reaction, igniting helium in a hydrogen rich surface layer where the hot CNO (hereafter, HCNO) cycles are operating. The helium ignition increases the temperature above $T_9 = 0.5$, the HCNO breakout [47–50] makes the production of nuclei in the region $A \geq 20$ possible, and the αp- and rp-processes [37, 51, 52] drive the nucleosynthesis through paths between the group of stable nuclei and the proton drip line while peak temperatures of $T_9 \sim 1$–2 are reached [4].

The explosive nucleosynthesis in hydrogen–helium rich environments at elevated temperatures involves many nuclear processes and is very complex. For illustrative purposes, the most important nuclear activity attained for typical XRB conditions will be described in the two subsequent sections. Section II.2.1 explains the breakout sequences that process nuclei from the HCNO region to the $A = 20$–21 mass range with increasing temperature. Section II.2.3 contains an example of a post-processing network calculation that is characteristic of the nucleosynthesis taking place during a type I XRB, based on the case given in Ref. [41].

II.2.1. Breakout from the hot CNO cycle

For stellar temperatures lower than $T_9 = 0.4$, most of the catalyst nuclei in the CNO and the HCNO cycles never exit the cycle. This occurs because the heaviest isotopes processed in the CNO and the HCNO cycles are ^{19}F and ^{18}F, respectively, which in the temperature ranges of those cycles ($T_9 < 0.1$ and $T_9 =$ 0.1–0.4 respectively) have branching ratios $B_{p\alpha/p\gamma}$ of the order of around 10^3–10^4 [53, 54]. Hence, both ^{19}F and ^{18}F are mostly recycled to lighter nuclei via (p,α) reactions instead of being processed to heavier nuclei via (p,γ) reactions.

Things are radically different at higher temperatures. At $T_9 > 0.5$, ^{14}O and ^{15}O nuclei, which act as catalysts in the HCNO cycles, are transmuted by means of a number of reaction sequences to nuclei in the mass range $A = 20$–21. And since there are no nuclear processes that can convert them back to the HCNO mass range, ^{14}O and ^{15}O nuclei are therefore consumed and permanently lost from the cycles. The three most important breakout sequences from the HCNO cycles are tabulated in Table I and shown in Fig. 5.

TABLE I: Main breakout sequences from the HCNO cycle.

Sequence 1	Sequence 2	Sequence 3
^{15}O$(\alpha,\gamma)^{19}$Ne	^{14}O$(\alpha,p)^{17}$F	^{14}O$(\alpha,p)^{17}$F
^{19}Ne$(p,\gamma)^{20}$Na	^{17}F$(p,\gamma)^{18}$Ne	^{17}F$(\gamma,p)^{16}$O
	^{18}Ne$(\alpha,p)^{21}$Na	^{16}O$(\alpha,\gamma)^{20}$Ne

The temperature–density (T–ρ) conditions for the competition between β^+-decay and proton- or α-particle-induced reaction for the nuclides involved in the three HCNO-breakout sequences are given in Fig. 6. The locations in the T–ρ plane at which the decay constants λ of the two competing processes are of equal magnitude (i.e., $\lambda_{\rm Z}({\rm Y}) = \lambda_\beta({\rm Y})$ where Y denotes the nuclide of

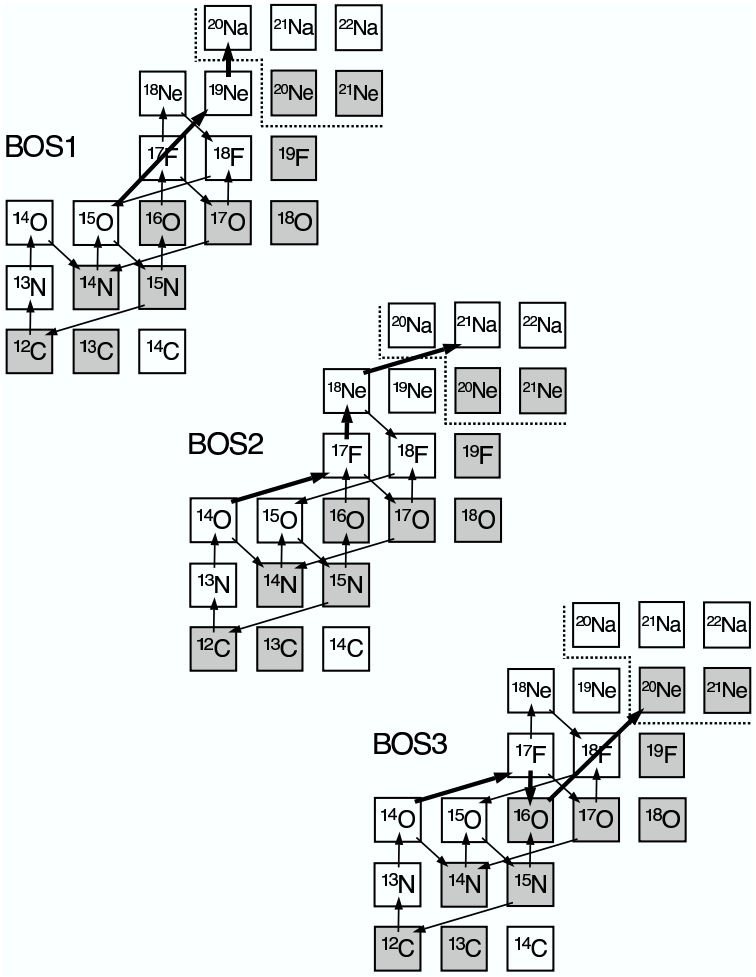

FIG. 5: The three breakout sequences (BOS) from the HCNO cycles (thick arrows) during hydrogen–helium burning. Nuclear interactions that are part of the HCNO1, HCNO2 and HCNO3 cycles are also shown (thin arrows). Stable nuclides are shown as shaded squares. Nuclei processed to species beyond the dotted line ($A = 20$) are permanently eliminated from the HCNO cycles since there are no processes that can convert those species back to the $A < 20$ region. Figure from Ref. [41].

interest and Z symbolizes either proton or α-particle, depending on the kind of reaction) are indicated by the solid and dashed curves. On the left-hand side of a solid or dashed curve the β^+-decay is more likely to occur, while on the right-hand side the competing proton- or α-particle-induced reaction is more significant. The dotted line shows the location in the T–ρ plane for which the

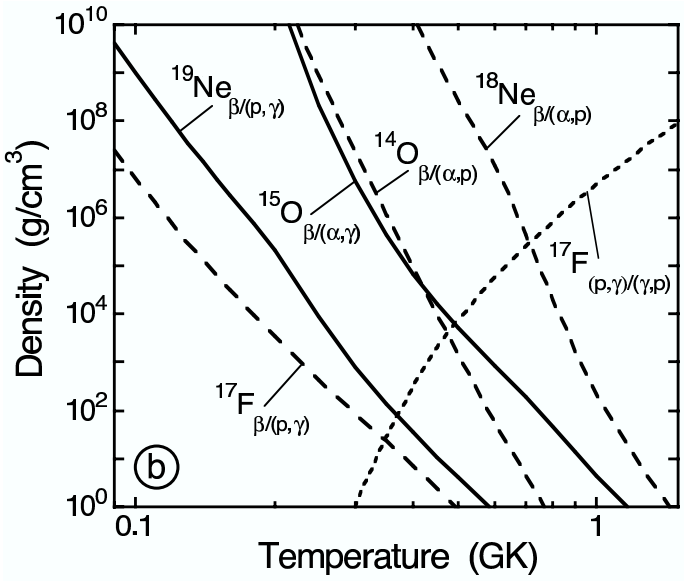

FIG. 6: Temperature-density conditions for the competition between β^+-decay and nuclear reaction for unstable nuclides that participate in the three breakout sequences (solid and dashed lines). The β^+-decay dominates on the left-hand side of a solid or dashed line, while on the right-hand side the competing proton- or α-particle-induced reaction is more likely to occur. The dotted line shows the conditions at which the decay constants for the competing ^{17}F(p,γ)^{18}Ne and ^{17}F(γ,p)^{16}O reactions are of equal magnitude, ^{17}F(p,γ)^{18}Ne being dominant on the left-hand side and ^{17}F(γ,p)^{16}O dominant on the right-hand side. All curves are calculated assuming $X_{\rm H} = 0.7$ and $X_{^4{\rm He}} = 0.3$. Figure from Ref. [41].

decay constants for the competing ^{17}F$(p,\gamma)^{18}$Ne and ^{17}F$(\gamma,p)^{16}$O reactions are of equal magnitude (i.e., $\lambda_p(^{17}{\rm F}) = \lambda_\gamma(^{17}{\rm F})$). The curves were determined by using mass-fractions of $X_{\rm H} = 0.7$ and $X_{^4{\rm He}} = 0.3$.

In the subsequent discussion of the three HCNO-breakout sequences, the characteristic density value will be taken as $\rho = 10^6$ g/cm^3, and it will be assumed that, as a result of previous HCNO cycle operation, the most abundant CNO nuclei are ^{14}O and ^{15}O [41]. The flow driven from those two nuclides, when the temperature is slowly increased and the HCNO breakout is initiated, will be considered.

The two solid curves in Fig. 6 have to be taken into account for describing breakout sequence 1. As can be seen on the T–ρ plane, moving through the line $\rho = 10^6$ g/cm^3 and slowly increasing the temperature from $T_9 \approx 0.1$ (the operation temperature range for the HCNO cycles), the competing processes ^{19}Ne$(\beta^+\nu)^{19}$F and ^{19}Ne$(p,\gamma)^{20}$Na become of equal magnitude at $T_9 \approx 0.17$, where the curve associated with the condition $\lambda_p(^{19}\mathrm{Ne}) = \lambda_\beta(^{19}\mathrm{Ne})$ is crossed. Hence, at $T_9 \gtrsim 0.17$ the ^{19}Ne$(p,\gamma)^{20}$Na reaction becomes more likely to occur than the competing ^{19}Ne β^+-decay. However, the breakout from the HCNO cycles does not occur yet because the previous step in the breakout sequence, the ^{15}O$(\alpha,\gamma)^{19}$Ne reaction which drives the flow towards ^{19}Ne, is still bypassed by the competing ^{15}O β^+-decay (i.e., $\lambda_\alpha(^{15}\mathrm{O}) < \lambda_\beta(^{15}\mathrm{O})$). Increasing the temperature further, the competing processes ^{15}O$(\beta^+\nu)^{15}$N and ^{15}O(α,γ) ^{19}Ne become of equal magnitude at $T_9 \approx 0.31$, where the curve corresponding to the condition $\lambda_\alpha(^{15}\mathrm{O}) = \lambda_\beta(^{15}\mathrm{O})$ is crossed. Hence, the breakout sequence 1 begins to operate at $T_9 \gtrsim 0.31$ by eliminating ^{15}O nuclei from the HCNO cycles and driving the flow to the mass range $A = 20$.

The dashed and dotted curves in Fig. 6 have to be taken into account for describing breakout sequences 2 and 3. For constant $\rho = 10^6$ g/cm^3 and temperatures higher than $T_9 \approx 0.11$, the nuclide ^{17}F is primarily destroyed by the (p,γ) reaction rather than by β^+-decay since the curve corresponding to the condition $\lambda_p(^{17}\mathrm{F}) = \lambda_\beta(^{17}\mathrm{F})$ is passed over. If the temperature is increased, the curve associated with the condition $\lambda_\alpha(^{14}\mathrm{O}) = \lambda_\beta(^{14}\mathrm{O})$ is crossed at $T_9 \approx 0.33$. Hence, from this temperature, the flow is preferentially driven via the ^{14}O$(\alpha,p)^{17}$F reaction which becomes more likely to occur than the competing ^{14}O β^+-decay. While the breakout sequences 2 and 3 are not operating yet, an additional connection between the HCNO1 and HCNO3 cycles is created

by the $^{14}O(\alpha,p)^{17}F$ reaction: ^{14}O is processed to ^{15}O through the sequence $^{14}O(\alpha,p)^{17}F(p,\gamma)^{18}Ne(\beta^+\nu)^{18}F(p,\alpha)^{15}O$. Thus, at $T_9 > 0.31$ the $^{14}O(\alpha,p)^{17}F$ reaction enlarges the fraction of CNO nuclei that is eliminated via breakout sequence 1.

Increasing the temperature further, the $^{18}Ne(\alpha,p)^{21}Na$ reaction dominates over the competing ^{18}Ne β^+-decay once the curve associated with the condition $\lambda_\alpha(^{18}Ne) = \lambda_\beta(^{18}Ne)$ is passed over at $T_9 \approx 0.65$. Therefore, at this temperature the breakout sequence 2 is initiated and takes away ^{14}O nuclei from the HCNO cycles.

The dotted curve corresponding to the condition $\lambda_p(^{17}F) = \lambda_\gamma(^{17}F)$ is crossed at $T_9 \approx 0.8$. At higher temperatures ^{17}F is preferentially destroyed by the $^{17}F(\gamma,p)^{16}O$ reaction. Because of the low Q-value of the $^{16}O(p,\gamma)^{17}F$ reaction ($Q = 0.600$ MeV) the equilibrium between the $^{17}F(\gamma,p)^{16}O$ and the time reverse $^{16}O(p,\gamma)^{17}F$ reactions is rapidly reached. The breakout sequences 2 and 3 must then advance from the equilibrium abundances of ^{17}F and ^{16}O. However, the breakout sequence 3 does not operate yet since the last step in the breakout sequence, the $^{16}O(\alpha,\gamma)^{20}Ne$ reaction responsible for driving the flow towards ^{20}Ne, is still less likely to occur than the competing $^{16}O(p,\gamma)^{17}F$ reaction. The rate at which ^{14}O nuclei will be eliminated from the HCNO cycles via breakout sequence 3 will depend on the equilibrium number of ^{16}O nuclei, specified by the temperature, and the ratio between the $^{16}O(\alpha,\gamma)^{20}Ne$ and the competing $^{16}O(p,\gamma)^{17}F$ reaction rates. This ratio continuously increases with the temperature [41]. Consequently, breakout sequence 3 will turn out to be more and more important for higher temperatures and will operate at $T_9 > 1.0$.

II.2.2. Example of network calculations

As discussed previously, explosive hydrogen–helium burning takes place in type I XRBs at temperatures higher than $T_9 = 0.5$. An example of an XRB nucleosynthesis calculation will be presented in this section. For illustrative proposes, a thermonuclear runaway caused by the accretion of hydrogen and helium onto the surface of a 1.3-$M_\odot$ neutron star with a radius of 8 km will be considered. The temporal evolution of the temperature and density in the hottest nuclear burning zone that was used in the numerical network calculation is shown in the inset of Fig. 7. The curves are like those obtained in hydrodynamic simulations of XRBs [55]. The nuclear burning starts with temperature and density values of $T_9 = 0.4$ and $\rho = 10^6$ g/cm^3. At $t = 4$ s, a maximum temperature of $T_9 = 1.36$ and a minimum density of $\rho = 5 \times 10^5$ g/cm^3 are reached. Once $t = 100$ s, the temperature falls to $T_9 = 0.7$ and the density increases to $\rho = 1.4 \times 10^6$ g/cm^3.

In order to account for all possible nuclear processes at such high temperatures about 520 nuclides were considered in the network, containing all the stable and proton-rich β^+-unstable (but proton-stable) nuclides up to palladium ($Z = 46$). Neutron-rich β^--unstable nuclides were not incorporated as part of the network since they cannot be synthesized by means of hydrogen- or helium-induced reactions on stable or proton-rich β^+-unstable nuclei. About 5500 nuclear processes were used to connect the different nuclei in the network, including, e.g., β^+-decays, (p,γ), (p,α), (α,γ) reactions and inverse processes such as photodisintegrations, (α,p) reactions, etc. Mass fractions of $X^0_{\rm H} = 0.73$, $X^0_{^4{\rm He}} = 0.25$, $X^0_{^{14}{\rm O}} = 0.01$ and $X^0_{^{15}{\rm O}} = 0.01$ were assumed as the initial composition, since ^{14}O and ^{15}O are the most abundant products of the HCNO cycle

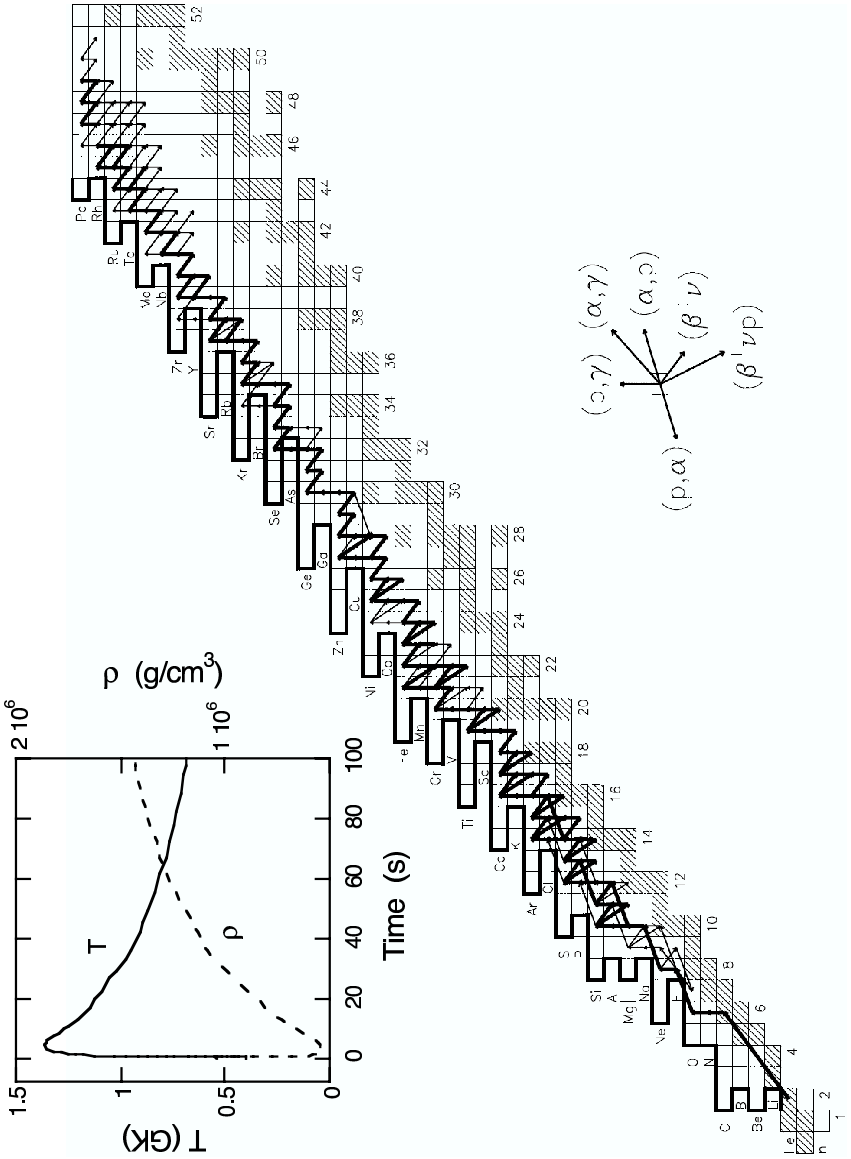

FIG. 7: Time-integrated net abundance flows during a thermonuclear runaway caused by the accretion of H and He onto the surface of a 1.3-$M_\odot$ neutron star with a radius of 8 km. The evolution of temperature and density in the nuclear burning zone, shown in the inset, is typical of the results obtained from hydrodynamic simulations of type I X-ray bursts [55]. The reaction network consists of the nuclides shown as squares (stable isotopes are shaded). Nuclides can be identified from the element symbol (vertical axis) and neutron number (horizontal axis). The arrows represent net (forward minus reverse) abundance flows, integrated over the entire computation time of $t = 100$ s. Thick arrows show the strongest flows. Thin arrows represent flows that are weaker by an order of magnitude. The key indicates the kind of reaction represented by each type of arrow. The proton drip line is shown as a heavy solid line. Figure from Ref. [41]

operation through the rise to temperatures $T_9 \geq 0.5$ [41]. The network calculation was performed until a time of $t = 100$ s was reached, consistent with the short timescales observed in XRBs.

Experimental rates from Refs. [56] and [57] were used for most reactions in the $A \leq 40$ mass range. Since for $A > 40$ the majority of the nuclear reactions have not been experimentally studied yet, theoretical estimations of the reaction rates obtained by using the Hauser-Feshbach statistical model have been employed. Hence, for the largest part of the reactions involved in the nucleosynthesis of this astrophysical site, theoretical rather than experimental rates have been used even though, in most of the cases, reaction rates based purely on theory have much larger uncertainties than those based on experimental data.

The time-averaged abundance flows for each nuclear process involved in the network were obtained by integrating over the entire computation time. Net abundance flows, obtained as the difference between those of the forward and reverse processes, are shown in Fig. 7. Major and minor net flows are shown as thick and thin solid arrows respectively, with the direction of the flows represented by the direction of the arrows. Stable nuclides are shaded and the proton drip line is shown as a heavy solid line. As shown in Fig. 7, the main paths followed by the abundance flow in XRB nucleosynthesis are located between the group of stable nuclei and the proton drip line.

As can be seen, in the $A \leq 14$ region the flow is mainly driven through the triple-α reaction up to ^{12}C, after which $^{12}\mathrm{C}(p,\gamma)^{13}\mathrm{N}(p,\gamma)^{14}\mathrm{O}$ dominates. Consequently, breakout from the CNO mass region mostly takes place through sequence 2 (i.e., via $^{14}\mathrm{O}(\alpha,p)^{17}\mathrm{F}(p,\gamma)^{18}\mathrm{Ne}(\alpha,p)^{21}\mathrm{Na}$), while a small fraction proceeds through sequence 1 (i.e., via $^{15}\mathrm{O}(\alpha,\gamma)^{19}\mathrm{Ne}(p,\gamma)^{20}\mathrm{Na}$). After exiting the cycle, matter is synthesized through the αp-process (sequences of (α,p) and

(p,γ) reactions in the $20 \leq A \leq 33$ region) and the *rp*-process (sequences of (p,γ) reactions and β^+-decays in the $A \geq 34$ region) [37, 51, 52]. Together, those processes transform CNO catalysts into heavier nuclei within $t = 100$ s.

At temperatures lower than $T_9 = 1$ photodisintegration impedes further proton captures. Hence, the abundance flow in the $A \leq 33$ region is stalled because it has to wait for slow β^+-decays of those nuclides that are most abundant at any given time (the so-called "waiting point nuclei"). Since β^+-decay half-lives are not sensitive to temperature and density, the mean lifetime of the waiting point nuclei, and thus the overall time scale of the nucleosynthesis at $T_9 \leq 1$ and $A \leq 33$, is not influenced by changes in temperature and density. At higher temperatures the αp-process bypasses the slow β^+-decay and hence, its importance lies in the fact that it makes the nucleosynthesis in the $A \leq 33$ region sensitive to temperature due to the high Coulomb barrier of (α,p) reactions. For the burning conditions considered in this example, above mass $A = 33$ the Coulomb barrier obstructs α-particle-induced reactions and hence the αp-process is replaced by the *rp*-process.

The nucleosynthesis path in the *rp*-process is defined by the competition between β^+-decays, and both (p,γ), and (γ,p) reactions. Along with the αp-process, the *rp*-process is essential since it makes it possible to bypass the slow β^+-decays via sequential two-proton capture. In the *rp*-process, successive sequential two-proton captures drive the flow towards the proton drip line and, thus, nuclei far away from the valley of stability are synthesized. As nuclides move away from the valley of stability and approach the proton drip line, their β^+-decay half-lives gradually shorten, decreasing the probability of proton capture relative to β^+-decay. Eventually, β^+-decay turns out to be more probable than proton capture, i.e., $\lambda_\beta > \lambda_{p\gamma}$. Moreover, nuclei located exactly at the pro-

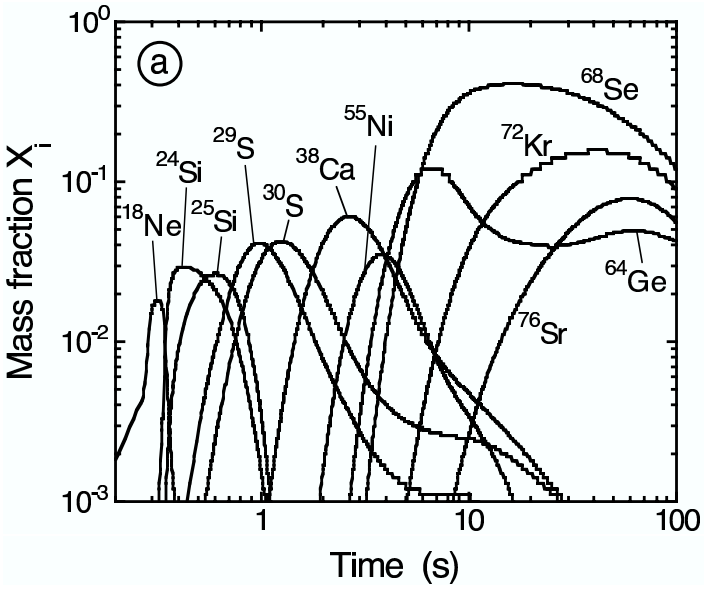

FIG. 8: Abundance time evolutions of the most significant waiting point nuclei for the example of numerical reaction network calculation shown in Fig. 7. Taken from Ref. [41].

ton drip line have by definition negative Q-values and some nuclei in the vicinity of the drip line have small positive Q-values. In either case, proton capture is inhibited by photodisintegration and the nucleosynthesis must proceed via a β^+-decay even if the condition $\lambda_\beta < \lambda_{p\gamma}$ remains valid. As seen from Fig. 7, the abundance flow arrives at the drip line at several points over the entire region used for the calculation, where in most cases the major flow is delayed before continuing via β^+-decay.

A considerable fraction of ^{1}H and ^{4}He nuclei is converted into heavier nuclei during the thermonuclear explosion. ^{1}H and ^{4}He abundances gradually decrease with time until they finally reach mass fractions of $X_{\rm H} = 0.16$ and $X_{^4{\rm He}} = 0.02$. The abundance time-evolution of the most significant waiting point nuclei is shown in Fig. 8. It can be seen that the abundance of a specific waiting point nucleus increases with time until a maximum is attained, and then falls. Maximums are reached in sequence for nuclides such as ^{18}Ne, ^{24}Si, ^{25}Si, ^{29}S, ^{30}S,

^{38}Ca, ^{55}Ni, ^{64}Ge, ^{68}Se, ^{72}Kr, ^{76}Sr. In each case, the abundance flow is stalled by processes that slowly consume the waiting point nucleus (e.g., the (α, p) reaction on ^{18}Ne, both β^+-decay and β-delayed proton emission of ^{24}Si, both the (α, p) reaction on and β^+-decay of ^{25}Si, the sequential two-proton captures on ^{64}Ge, etc.). At $t = 4$ s, when the highest temperature is reached, ^{60}Zn, ^{55}Ni, ^{38}Ca, ^{59}Zn, and ^{64}Ge (in addition to ^{1}H and ^{4}He) are the most abundant nuclides with similar mass fractions of $X \approx 0.03$. At $t = 10$ s, since the abundance flow must wait for its slow β^+-decay, ^{68}Se is by far the most abundant nucleus ($X_{^{68}\mathrm{Se}} = 0.35$) among all nuclides excluding ^{1}H. The $Q_{p\gamma}$-values for the waiting point nuclei ^{64}Ge, ^{68}Se, ^{72}Kr, and ^{76}Sr are predicted to be negative [58], while their β^+-decay half-lives amount to $T_{1/2} = 64$ s, 36 s, 17 s, and 9 s, respectively. At ^{64}Ge the major flow proceeds through sequential two-proton capture rather than the very slow β^+-decay which otherwise would have terminated the nucleosynthesis. For ^{68}Se, ^{72}Kr, and ^{76}Sr, the other three waiting point nuclei, the β^+-decay dominates over the competing sequential two-proton capture. For this reason, the abundance flow is considerably reduced and hence an accumulation of material is expected near the end of the calculation, particularly at ^{68}Se and ^{72}Kr. ^{68}Se is slowly exhausted with time, causing an increase in the abundances of some nuclides in the $A > 68$ region. As seen from Fig. 8, at the end of the calculation ^{68}Se, ^{72}Kr, ^{76}Sr, and ^{64}Ge are (besides ^{1}H) the most numerous nuclei, which will rapidly decay to ^{68}Ge ($T_{1/2} = 271$ d), ^{72}Se ($T_{1/2} = 8.4$ d), ^{76}Kr ($T_{1/2} = 14.8$ h), and ^{64}Zn (stable), respectively, once the thermonuclear explosion ends and the *rp*-process is terminated. An important part of the matter ($\sum X_i = 0.20$) has been transformed from ^{1}H and ^{4}He to nuclides in the region between the elements zirconium and ruthenium. The total mass fraction of nuclei accumulated at the elements rhodium and palladium ($\sum X_i = 0.16$), the end of the network,

would have been processed to even heavier nuclides if the network had not been artificially truncated. For a discussion of abundance time-evolutions in the proton-number range above palladium see, for instance, Refs. [6, 38, 55].

An extensive study of type I XRB nucleosynthesis can be found in Ref. [39], while a discussion of thermally stable hydrogen–helium burning on accreting neutron stars is well described in Ref. [26].

II.2.3. Sensitivity studies in X-ray burst nucleosynthesis and the $^{30}P(\alpha,p)^{33}S$ reaction

Most of the nuclear reaction rates needed for nucleosynthesis calculations are based on theoretical estimates from statistical models. These theoretical reaction rates are affected by significant uncertainties, which may considerably impact on the final abundances of nucleosynthesis calculations. To date, Parikh *et al.* [5] have done the most extensive sensitivity study in order to quantify the effects of the reaction rate uncertainties on XRB nucleosynthesis models. In that work, the nuclear processes for which variations in reaction rate produce the largest impact on the final isotopic abundances of type I XRB nucleosynthesis were identified. These processes are of particular importance and their reaction rates deserve further improvement through nuclear physics experiments.

They carried out a series of about 40,000 postprocessing calculations requiring 14 CPU-months, in which each nuclear rate was varied individually by a factor of 10 up and down.

They used three different temperature-density vs. time profiles extracted from the literature:

i) model K04, based on an accretion rate of 2.3×10^4 g cm^{-2} s^{-1} onto a 1.3-$M_\odot$ neutron star with a radius of 8.1 km, characterized by a peak temperature of $T_9 = 1.36$, densities in the range (0.54–1.44) $\times 10^6$ g cm^{-3}, a burst duration of around 100 s, and an initial composition with $X = 0.73$, $Y = 0.25$, and $Z = 0.02$ (roughly solar);

ii) model F08, based on a neutron star of 1.4 $M_\odot$ with a radius of 11 km, a mass accretion rate of 0.66×10^4 g cm^{-2} s^{-1}, a peak temperature of only $T_9 = 0.993$, densities in the range (2.07–5.14) $\times 10^6$ g cm^{-3}, a burst duration of around 50 s, and an initial composition with $X = 0.40$, $Y = 0.41$, and $Z = 0.19$ (a metallicity about 10 times solar);

iii) model S01, which achieves the largest temperature with a peak of $T_9 = 1.907$, a mass accretion rate of 8.8×10^4 g cm^{-2} s^{-1}, densities in the range (0.54–1.73) $\times 10^6$ g cm^{-3}, a burst duration of around 300 s, and an initial composition with $X = 0.718$, $Y = 0.281$, and $Z = 0.001$ (a metallicity about 20 times lower than solar).

They also generated additional models through parameterizations of the model K04 temperature-density-time profiles, to account the role played by the initial metallicity, the peak temperature achieved, and the duration of the bursts. Together, these models partially cover the parameter space in XRB nucleosynthesis calculations.

They used a nuclear network of 606 nuclides ranging from ^{1}H to ^{113}Xe and included all charged-particle induced reactions between these isotopes, as well as their corresponding reverse processes. For the weak interactions, they used laboratory decay rates and took into account the influence of β-delayed nucleon emission. Neutron captures were not considered, as previous test calculations have shown that they play a minor role in XRB nucleosynthesis. In that way,

more than 3500 nuclear processes were included.

Experimental rates were only available for a small subset of reactions, for all other reactions they used theoretical estimates from the Hauser-Feshbach code NONSMOKER [59]. They used stellar reaction rates, i.e., the effects of thermal excitations in the target nuclei were taken into account.

TABLE II: Most influential reactions in X-ray burst nucleosynthesis models. They affect the final abundances of at least three isotopes by no less than a factor of two up or down when their nominal rates are varied by a factor of 10 up or down.

$^{12}\mathrm{C}(\alpha,\gamma)^{16}\mathrm{O}$
$^{18}\mathrm{Ne}(\alpha,p)^{21}\mathrm{Na}$
$^{25}\mathrm{Si}(\alpha,p)^{28}\mathrm{P}$
$^{26g}\mathrm{Al}(\alpha,p)^{29}\mathrm{Si}$
$^{29}\mathrm{S}(\alpha,p)^{32}\mathrm{Cl}$
$^{30}\mathrm{P}(\alpha,p)^{33}\mathrm{S}$
$^{30}\mathrm{S}(\alpha,p)^{33}\mathrm{Cl}$
$^{31}\mathrm{Cl}(p,\gamma)^{32}\mathrm{Ar}$
$^{32}\mathrm{S}(\alpha,\gamma)^{36}\mathrm{Ar}$
$^{56}\mathrm{Ni}(\alpha,p)^{59}\mathrm{Cu}$
$^{57}\mathrm{Cu}(p,\gamma)^{58}\mathrm{Zn}$
$^{59}\mathrm{Cu}(p,\gamma)^{60}\mathrm{Zn}$
$^{61}\mathrm{Ga}(p,\gamma)^{62}\mathrm{Ge}$
$^{65}\mathrm{As}(p,\gamma)^{66}\mathrm{Se}$
$^{69}\mathrm{Br}(p,\gamma)^{70}\mathrm{Kr}$
$^{75}\mathrm{Rb}(p,\gamma)^{76}\mathrm{Sr}$
$^{82}\mathrm{Zr}(p,\gamma)^{83}\mathrm{Nb}$
$^{84}\mathrm{Zr}(p,\gamma)^{85}\mathrm{Nb}$
$^{84}\mathrm{Nb}(p,\gamma)^{85}\mathrm{Mo}$
$^{85}\mathrm{Mo}(p,\gamma)^{86}\mathrm{Tc}$
$^{86}\mathrm{Mo}(p,\gamma)^{87}\mathrm{Tc}$
$^{87}\mathrm{Mo}(p,\gamma)^{88}\mathrm{Tc}$
$^{92}\mathrm{Ru}(p,\gamma)^{93}\mathrm{Rh}$
$^{93}\mathrm{Rh}(p,\gamma)^{94}\mathrm{Pd}$
$^{96}\mathrm{Ag}(p,\gamma)^{97}\mathrm{Cd}$
$^{102}\mathrm{In}(p,\gamma)^{103}\mathrm{Sn}$
$^{103}\mathrm{In}(p,\gamma)^{104}\mathrm{Sn}$
$^{103}\mathrm{Sn}(\alpha,p)^{106}\mathrm{Sb}$

From the several thousand nuclear processes involved in XRB nucleosynthesis,

they found that only about 50 reactions (as well as the corresponding reverse reactions) have a significant impact on the final products when their rates were varied by a factor of 10 up and down. A list of the most influential reactions (defined as those which affect the final abundances of at least three isotopes by more than a factor of two up or down when their nominal rates are varied by a factor of 10 up or down) is given in Table II. As can be seen, most of them are proton captures, a few are (α, p) reactions and only two are α-captures. Most of these key reactions affect the final abundances of nuclides in the surrounding area of the target nuclei.

The ^{30}P(α, p) ^{33}S reaction is one of these most influential processes in XRB nucleosynthesis, and its cross section and stellar rate are studied in this thesis. Figure 9 shows the nuclide chart around the target nucleus of the ^{30}P$(\alpha, p)^{33}$S reaction. When the nominal rate of this reaction is varied by a factor of 10 up and down the affected nuclides are ^{30}Si (by a factor of about 20 up and a factor of about 30 down), ^{31}P (by a factor of about 2 up), ^{33}S (by a factor of about 4 down), and ^{36}Cl (by a factor of about 3 down).

In summary, through sensitivity studies Parikh *et al.* identified a very limited number of reactions that play a significant role in XRB nucleosynthesis. Their results can motivate future measurements by experimental nuclear physicists. In Chapter IV of this thesis a technique developed to measure the ^{30}P$(\alpha, p)^{33}$S reaction will be presented. The cross section and the stellar reaction rate were obtained and are given in Chapters V and VI, respectively. A major advantage of this technique is that it can also be employed in experiments involving radioactive ion beams, therefore making possible the measurement of (α, p) reactions involving short-lived nuclei in both the entrance and exit channels in the medium mass range, most of which have not been studied yet.

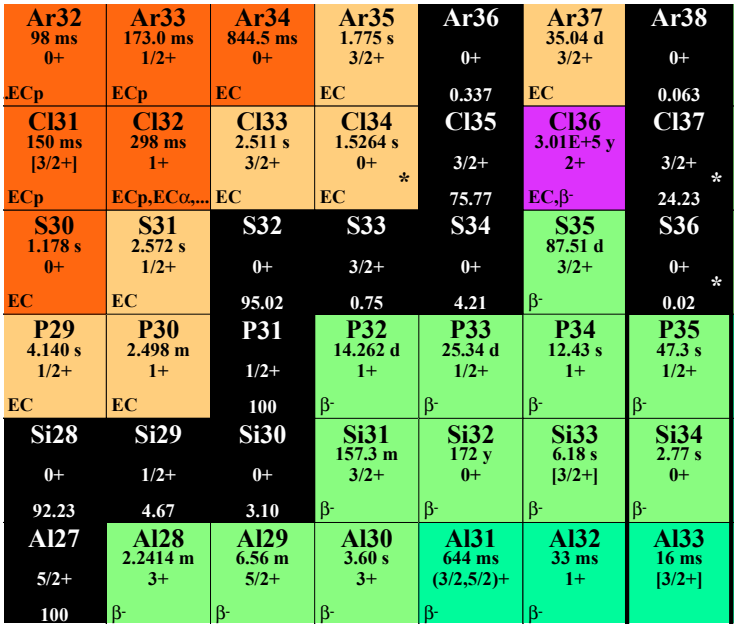

FIG. 9: Vicinity in the nuclide chart for the target nucleus of the $^{30}\mathrm{P}(\alpha, p)^{33}\mathrm{S}$ reaction. Sensitivity studies in X-ray burst nucleosynthesis showed that variations in the nominal rate of that reaction by a factor of 10 up or down affect the final abundances of the stable ^{30}Si, ^{31}P, ^{33}S and the long-lived ^{36}Cl nuclei deeply.

III. THERMONUCLEAR REACTIONS BACKGROUND

III.1. Cross sections

In nuclear and particle physics, a quantitative measure of the probability that a certain reaction $A(a,b)B$ takes place is given by means of the cross section σ, which is defined by [60]

$$\sigma_{aA} = \frac{R}{J}\,, \tag{1}$$

where R is the number of particles of type b produced per unit time per nucleus of type A in the target, and J is the number of incident particles of type a per unit time per unit area.

The differential cross section $\left(\frac{d\sigma}{d\Omega}\right)_{aA}(\theta,\phi)$ is defined by the number of reactions per unit time with the particles of type b emitted within an element of solid angle $d\sigma$ in the direction with polar angles (θ,ϕ) with respect to the incident beam.

For the reaction studied in this work, the spins of the particles are not polarized and therefore the scattering process is symmetrical about the direction of the incident beam, i.e., the differential cross section does not depend on the azimuthal angle ϕ.

Experimentally, the differential cross section can be measured with a detector placed at the polar angle θ which covers a small solid angle $\Omega_{\rm det}$, using the

approximation

$$\left(\frac{d\sigma}{d\Omega}\right)_{aA}(\theta) \cong \frac{R_{\rm det}}{J}\frac{1}{\Omega_{\rm det}}\,, \tag{2}$$

where in this case $R_{\rm det}$ is associated with the number of particles of type b emitted in the direction of the detector per unit time per nucleus of type A in the target.

III.2. Conversion between parameters in the center-of-mass and laboratory systems

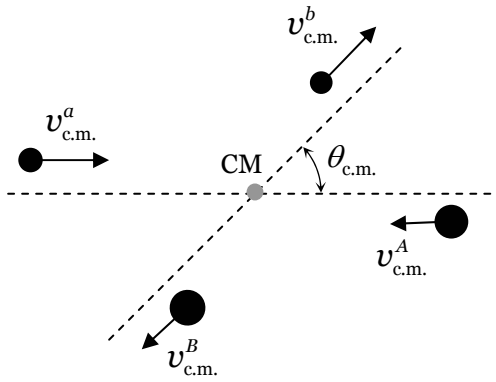

FIG. 10: Schematic illustration of a collision in the center-of-mass system. The projectile nucleus (a) collides with the target nucleus (A) and the ejectil (b) and the residual nuclei (B) are obtained as reaction products. The center-of-mass velocity vectors of each nucleus are designated by $v^i_{\rm c.m.}$ ($i = a, A, b, B$) and $\theta_{\rm c.m.}$ is the center-of-mass scattering angle.

A schematic illustration of a collision as seen from the center-of-mass system is shown in Fig. 10. Before the collision, the projectile a and the target nucleus A with center-of-mass velocities $\boldsymbol{v}^a_{\rm c.m.}$ and $\boldsymbol{v}^A_{\rm c.m.}$ are approaching each other at the relative velocity $\boldsymbol{v} = \boldsymbol{v}^a_{\rm c.m.} - \boldsymbol{v}^A_{\rm c.m.}$ and initial kinetic energy in the center-of-mass

system $E_{\text{c.m.}} = \frac{1}{2}m^a \left(v^a_{\text{c.m.}}\right)^2 + \frac{1}{2}m^A \left(v^A_{\text{c.m.}}\right)^2 = \frac{1}{2}\mu \boldsymbol{v}^2$ where $\mu = \frac{m^a\, m^A}{m^b + m^B}$ is the reduced mass and m^a, m^A, m^b y m^B are the masses of the projectile, target, ejectile and residue nuclei, respectively. After the collision the ejectile b and the residue B exit at the relative velocity $\boldsymbol{v}^b_{\text{c.m.}} - \boldsymbol{v}^B_{\text{c.m.}}$ and center-of-mass scattering angle $\theta_{\text{c.m.}}$.

From kinematical considerations, it is possible to obtain that the differential solid angles in the center-of-mass and laboratory systems, $d\Omega_{\text{c.m.}}$ and $d\Omega_{\text{lab.}}$ respectively, are related by [61, 62]

$$d\Omega_{\text{lab.}} = \kappa\, d\Omega_{\text{c.m.}}\,, \tag{3}$$

where

$$\kappa = \frac{1 + \tau\cos\left(\theta_{\text{c.m.}}\right)}{\left(1 + \tau^2 + 2\tau\cos\left(\theta_{\text{c.m.}}\right)\right)^{3/2}} = \frac{\left(1 - \tau^2\sin^2\left(\theta^b_{\text{lab.}}\right)\right)^{1/2}}{\left[\tau\cos\left(\theta^b_{\text{lab.}}\right) + \left(1 - \tau^2\sin^2\left(\theta^b_{\text{lab.}}\right)\right)^{1/2}\right]^2} \tag{4}$$

and

$$\tau = \frac{V_{\text{c.m.}}}{v^b_{\text{c.m.}}} = \sqrt{\frac{m^a\, m^b}{m^A\, m^B}\frac{E_{\text{c.m.}}}{\left(E_{\text{c.m.}} + Q\right)}}\,. \tag{5}$$

In these expressions, $\theta^b_{\text{lab.}}$ is the ejectile laboratory scattering angle, $V_{\text{c.m.}}$ is the velocity of the center of mass and $Q = \left(m^a + m^A - m^b - m^B\right)c^2$ is the Q-value of the reaction.

Therefore, from Eq. 3 one can see that the relation between the differential cross sections in the center-of-mass and laboratory systems is given by

$$\left(\frac{d\sigma}{d\Omega}\right)_{\text{c.m.}} = \kappa \left(\frac{d\sigma}{d\Omega}\right)_{\text{lab.}} . \tag{6}$$

It is also possible to deduce (see Ref. [61, 62]) that the relation between the initial kinetic energy in the center-of-mass and laboratory systems is given by

$$E_{\text{c.m.}} = \frac{m^A}{m^a + m^A} E_{\text{lab.}} , \tag{7}$$

and that the ejectile scattering angles in the center-of-mass and laboratory systems are related by the expression

$$\cos\left(\theta_{\text{c.m.}}\right) = \cos\left(\theta^b_{\text{lab.}}\right) \sqrt{1 - \tau^2 \sin^2\left(\theta^b_{\text{lab.}}\right)} - \tau \sin^2\left(\theta^b_{\text{lab.}}\right) . \tag{8}$$

III.3. The reciprocity theorem

The cross section of the $A(a,b)B$ reaction, σ_{aA}, is related to that of the time-reverse $B(b,a)A$ reaction, σ_{bB}, by means of the reciprocity theorem [41, 63, 64], since the nuclear processes involving strong and electromagnetic interactions are invariant under time-reversal (i.e., the direction of time does not enter explicitly in the equations describing these processes). At a given total energy (i.e., rest mass plus center-of-mass kinetic energy), the corresponding cross sections σ_{aA} and σ_{bB} are not equal but are simply related by the phase space available in the exit channel or, equivalently, by the number of final states per unit energy interval in each case. For particles with spins J_a and J_A and relative momentum $\hbar k_{aA}$, the number of states available between k_{aA} and $k_{aA} + dk_{aA}$ is proportional to $k^2_{aA}(2J_a+1)(2J_A+1)$ [65]. Hence, for non-identical particles the

theorem states that

$$\frac{\sigma_{aA}}{k_{bB}^2(2J_b+1)(2J_B+1)} = \frac{\sigma_{bB}}{{k_{aA}}^2(2J_a+1)(2J_A+1)}\,. \tag{9}$$

In terms of the center-of-mass kinetic energies, and written for the specific case of the $^{33}\mathrm{S}(p,\alpha)^{30}\mathrm{P}$ reaction, this expression becomes [41]

$$\frac{\sigma_{\alpha^{30}\mathrm{P}}}{\sigma_{p^{33}\mathrm{S}}} = \frac{\mu_{p^{33}\mathrm{S}}}{\mu_{\alpha^{30}\mathrm{P}}}\frac{E_{p^{33}\mathrm{S}}}{E_{\alpha^{30}\mathrm{P}}}\frac{(2J_p+1)(2J_{^{33}\mathrm{S}}+1)}{(2J_\alpha+1)(2J_{^{30}\mathrm{P}}+1)}\,, \tag{10}$$

where

$$\mu_{p^{33}\mathrm{S}} = \frac{m_p m_{^{33}\mathrm{S}}}{m_p + m_{^{33}\mathrm{S}}} \tag{11}$$

and

$$\mu_{\alpha^{30}\mathrm{P}} = \frac{m_\alpha m_{^{30}\mathrm{P}}}{m_\alpha + m_{^{30}\mathrm{P}}} \tag{12}$$

are the reduced masses, and $E_{p^{33}\mathrm{S}}$ and $E_{\alpha^{30}\mathrm{P}}$ are related either by

$$E_{\alpha^{30}\mathrm{P}} = E_{p^{33}\mathrm{S}} + Q_{[^{33}\mathrm{S}(p,\alpha)^{30}\mathrm{P}]} \tag{13}$$

or

$$E_{\alpha^{30}\mathrm{P}} = E_{p^{33}\mathrm{S}} + Q_{[^{33}\mathrm{S}(p,\gamma)^{34}\mathrm{Cl}]} - Q_{[^{30}\mathrm{P}(\alpha,\gamma)^{34}\mathrm{Cl}]} \tag{14}$$

as can be seen from the energy level scheme for the $^{33}\mathrm{S}(p,\alpha)^{30}\mathrm{P}$ reaction shown in Fig. 11.

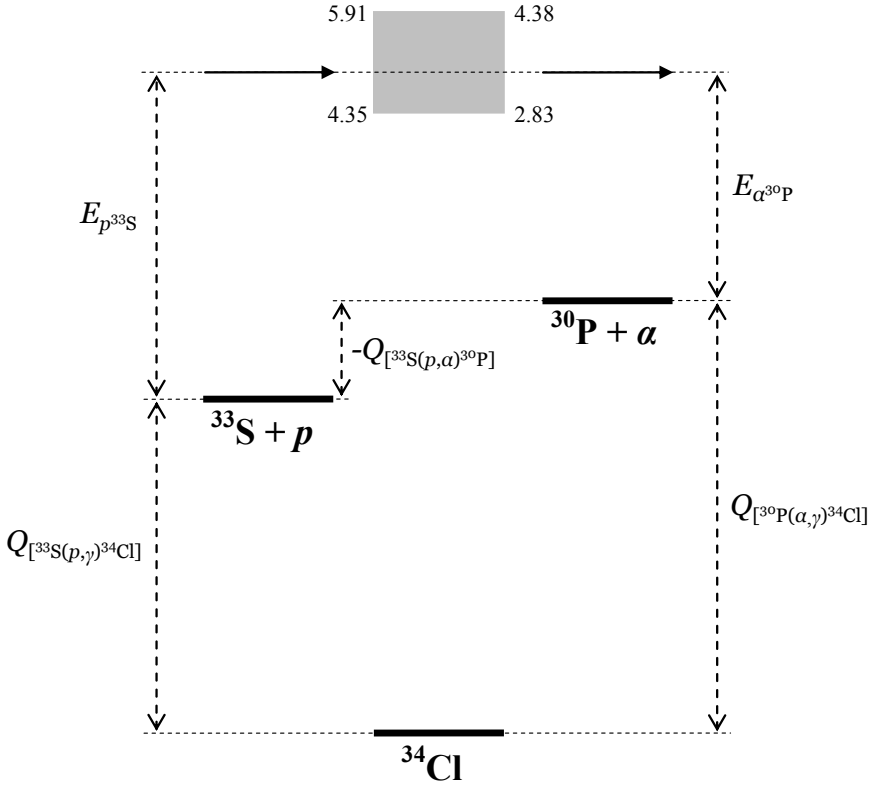

FIG. 11: Energy level scheme for the $^{33}\mathrm{S}(p,\alpha)^{30}\mathrm{P}$ reaction. Horizontal arrows represent total energies (rest masses plus kinetic energies) in the $^{33}\mathrm{S}+p$ and $^{30}\mathrm{P}+\alpha$ channels. Vertical arrows indicate: Q-values of the $^{33}\mathrm{S}+p$ channel with respect to the ground states of the $^{30}\mathrm{P}+\alpha$ channel and the compound nucleus $^{34}\mathrm{Cl}$ ($Q_{[^{33}\mathrm{S}(p,\alpha)^{30}\mathrm{P}]}$ and $Q_{[^{33}\mathrm{S}(p,\gamma)^{34}\mathrm{Cl}]}$, respectively), Q-value of the $^{30}\mathrm{P}+\alpha$ channel with respect to the ground state of $^{34}\mathrm{Cl}$ ($Q_{[^{30}\mathrm{P}(\alpha,\gamma)^{34}\mathrm{Cl}]}$), and center-of-mass kinetic energies in the $^{33}\mathrm{S}+p$ and $^{30}\mathrm{P}+\alpha$ channels ($E_{p^{33}\mathrm{S}}$ and $E_{p^{30}\mathrm{P}}$, respectively). The shadowed region above $^{34}\mathrm{Cl}$ represents the energy range studied in this work (4.35–5.91 MeV and 2.83–4.38 MeV in the $^{33}\mathrm{S}+p$ and $^{30}\mathrm{P}+\alpha$ channels, respectively).

III.4. Reaction rate

In nuclear astrophysics the quantity of importance for nucleosynthesis and energy-release calculations is the reaction rate, which is the number of times that a specific nuclear reaction $A(a,b)B$ occurs per unit time and per unit volume in an stellar environment at a given temperature T. This stellar reaction

rate depends on two factors: 1) the distribution $\phi(v)$ of the relative velocity of particles of types a and A in the environment, which is a function of T, and 2) the cross sections $\sigma(v)$ of the reaction $A(a,b)B$, which is a function of the relative velocity. If N_a and N_A are the numbers of particles of types a and A per unit volume in the stellar gas, particles of type a see an effective reaction area per unit volume which is given by $F = N_A\sigma(v)$, while particles of type A see a flux of particles of type a which is given by $J = vN_a$. Therefore, the rate of nuclear reactions $A(a,b)B$ occurring at a certain relative velocity v is given by the product FJ [22], i.e.,

$$r(v) = N_a N_A \, v\sigma(v) \, . \tag{15}$$

Since the product N_aN_A accounts for the total number of pairs of particles of types a and A, the product must be divided by two for identical particles. Thus, a more general expression which takes into account the case of identical particles can be written as

$$r(v) = \frac{N_a N_A}{(1+\delta_{aA})} v\sigma(v) \, , \tag{16}$$

where δ_{aA} is the Kronecker symbol.

In normal stellar matter, the nuclei move non-relativistically and the stellar gas is in thermodynamic equilibrium. The probability distributions for the velocities of particles of types a and A are therefore given by Maxwell-Boltzmann velocity distributions [22]

$$\phi(v_a) = 4\pi v_a^2 \left(\frac{m_a}{2\pi kT}\right)^{3/2} \exp\left(-\frac{m_a v_a^2}{2kT}\right)$$
$$\phi(v_A) = 4\pi v_A^2 \left(\frac{m_A}{2\pi kT}\right)^{3/2} \exp\left(-\frac{m_A v_A^2}{2kT}\right), \tag{17}$$

where k is the Boltzmann constant, and v_a, v_A, m_a and m_A are the velocities and masses, respectively. These velocity distributions are normalized to unity and, of course, dependent on the temperature T.

The total reaction rate r at a given temperature is therefore the weighted average of $r(v)$ over the velocity distributions, i.e.,

$$r = \int_0^\infty \int_0^\infty \phi(v_a)\phi(v_A) r(v) dv_a dv_A \,, \tag{18}$$

where v still represents the relative velocity between the interacting nuclei.

The product $\phi(v_a)\phi(v_A)dv_a dv_A$ can be written in terms of v and the center-of-mass velocity V as $\phi(V)\phi(v)dVdv$ [22], where these transformed velocity distributions are

$$\phi(V) = 4\pi V^2 \left(\frac{M}{2\pi kT}\right)^{3/2} \exp\left(-\frac{MV^2}{2kT}\right) \tag{19}$$

$$\phi(v) = 4\pi v^2 \left(\frac{\mu}{2\pi kT}\right)^{3/2} \exp\left(-\frac{\mu v^2}{2kT}\right) , \tag{20}$$

with

$$M = m_a + m_A \tag{21}$$

the total mass and

$$\mu = \frac{m_a m_A}{m_a + m_A} \tag{22}$$

the reduced mass.

Hence, the total reaction rate can be written as

$$r = \int_0^\infty \int_0^\infty \phi(V)\phi(v)r(v)dV\,dv \tag{23}$$

which can be factorized into two parts. Using $\int_0^\infty \phi(V)dV = 1$ and Eq. 20, the total reaction rate finally becomes

$$r = \frac{N_a N_A}{(1+\delta_{aA})} \int_0^\infty \phi(v)\sigma(v)v\,dv\,. \tag{24}$$

The integral in Eq. 24,

$$\langle \sigma v \rangle = \int_0^\infty \phi(v)\sigma(v)v dv = \frac{r}{N_a N_A (1+\delta_{aA})^{-1}}\,, \tag{25}$$

represents the reaction rate per particle pair since, as mentioned above, the product $N_a N_A (1+\delta_{aA})^{-1}$ is the total number of pairs of particles of types a and A. The reaction rate per particle pair $\langle \sigma v \rangle$ contains the nuclear physics information, while the total reaction rate r also depends on stellar gas properties through the particle densities N_a and N_A.

Inserting the velocity distribution of Eq. 20 into Eq. 25, the reaction rate per particle pair $\langle \sigma v \rangle$ as a function of temperature can be finally expressed as

$$\langle \sigma v \rangle = 4\pi \left(\frac{\mu}{2\pi kT}\right)^{3/2} \int_0^\infty v^3 \sigma(v) \exp\left(-\frac{\mu v^2}{2kT}\right) dv\,, \tag{26}$$

which in terms of the center-of-mass energy $E = \frac{1}{2}\mu v^2$ can be written as

$$\langle \sigma v \rangle = \left(\frac{8}{\pi \mu} \right)^{1/2} \frac{1}{(kT)^{3/2}} \int_0^\infty \sigma(E) E \exp\left(-\frac{E}{kT} \right) dE \,. \tag{27}$$

In practice, the reaction rate per particle pair is presented in the literature in units of $\mathrm{cm}^3\,\mathrm{mole}^{-1}\,\mathrm{s}^{-1}$ by means of the quantity $N_{\mathrm{Av}} \langle \sigma v \rangle$, where N_{Av} stands for the Avogadro constant, rather than $\langle \sigma v \rangle$ in units of $\mathrm{cm}^3\ \mathrm{s}^{-1}$.

III.5. The astrophysical S-factor

The energy dependence of cross sections in charged-particle induced nuclear reactions at energies E less than and close to the Coulomb barrier energy E_C can be described by two contributions which do not involve the internal nuclear structure. These contributions arise from the fact that at those energies nuclei primarily interact like sub-atomic charged spheres governed by the laws of quantum mechanics.

One of the contributions depends on the effective geometrical area $\tilde{A}$ of the interacting nuclei, the cross section σ being proportional to $\tilde{A}$. Due to wave aspects of quantum mechanical processes this area can be approximated as $\tilde{A} \sim \pi\lambda^2$, where λ stands for the de Broglie wavelength. Because for non-relativistic particles $\lambda^2 = \frac{h^2}{2\mu E}$, the energy dependence of this geometrical contribution to the cross section becomes

$$\sigma \propto \frac{1}{E} \,. \tag{28}$$

The other contribution depends on the tunneling probability for the interact-

ing nuclei to penetrate the Coulomb barrier, which can be approximated by the so-called Gamow factor [66]

$$\sigma \propto \exp(-2\pi\eta)\,, \tag{29}$$

where

$$\eta = \frac{Z_a Z_A e^2}{\hbar}\sqrt{\frac{\mu}{2E}} \tag{30}$$

is the Sommerfeld parameter.

It is useful to express the cross section as

$$\sigma(E) = \frac{1}{E}\exp(-2\pi\eta)S(E)\,, \tag{31}$$

where $S(E)$ is the so-called astrophysical S-factor. In this way, all of the strictly nuclear effects on the energy dependence of the cross section are exclusively included in $S(E)$. For non-resonant reactions the S-factor has a smooth behavior and is much less dependent on the energy than the cross section. For this reason, the S-factor is valuable for extrapolations of experimental cross sections to lower astrophysical energies, making it possible to calculate the reaction rate per particle pair as

$$\langle\sigma v\rangle = \left(\frac{8}{\pi\mu}\right)^{1/2}\frac{1}{(kT)^{3/2}}\int_0^\infty S(E)\exp\left(-\frac{E}{kT}\right)\exp\left(-\frac{b}{E^{1/2}}\right)dE\,, \tag{32}$$

where

$$b = \sqrt{2\mu}\pi \frac{Z_a Z_A e^2}{\hbar} \,. \tag{33}$$

The product of the two terms $\exp\left(-\frac{E}{kT}\right)$ from the Maxwell-Boltzmann distribution and $\exp\left(-\frac{b}{E^{1/2}}\right)$ from the tunneling through the Coulomb barrier in the integrand acts as a weight $w(E)$ for $S(E)$. This function $w(E)$, called the Gamow peak, is shown in Fig. 12 for the reaction and temperature of interest in this work, i.e., the ^{30}P(α,p)^{33}S reaction at an XRB temperature $T_9 = 1$. As can be seen, at a given temperature T the Gamow peak acts as a narrow energy window where most of the thermonuclear reactions take place. It has a maximum at

$$E_0 = \left(\frac{bkT}{2}\right)^{2/3} \tag{34}$$

and a relative narrow width

$$\Delta = \left(\frac{4}{3^{1/2}}\right)(E_0 kT)^{1/2} \,. \tag{35}$$

It is therefore E_0, instead of the energy corresponding to maximum of the Maxwell-Boltzmann distribution kT, which is the most effective energy for non-resonant thermonuclear reactions, whereas Δ is the effective width of the energy window. Moreover, $E_0 \gg kT$ when at least one of the interacting nuclei has a proton number $Z \gtrsim 6$. For the ^{30}P(α,p)^{33}S reaction at $T_9 = 1$, as shown in Fig. 12, the most effective energy for non-resonant thermonuclear reactions is $E_0 = 1800$ keV, a much higher value than the maximum of the

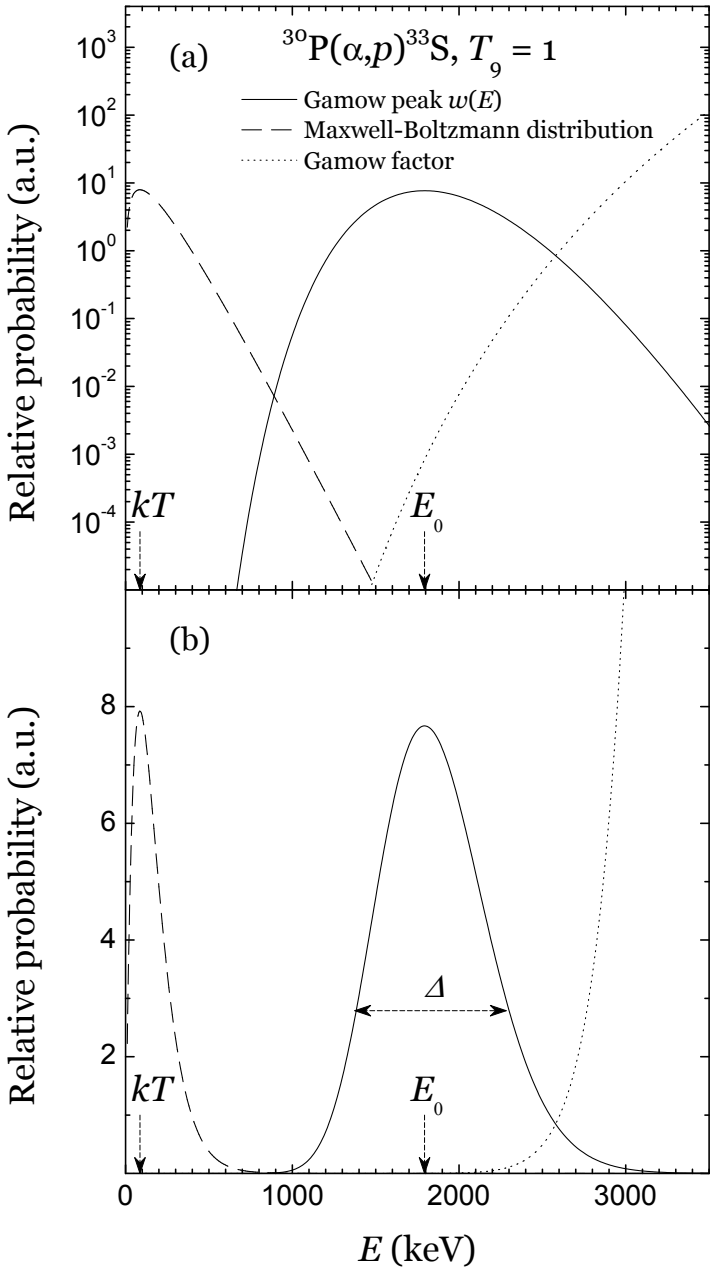

FIG. 12: Gamow peak $w(E)$ for the ^{30}P(α,p)^{33}S reaction at $T_9 = 1$ plotted in logarithmic and linear scales in panels (a) and (b), respectively. This function $w(E)$, the product of the exponential term of the Maxwell-Boltzmann distribution and the exponential term of the Coulomb-barrier tunneling probability (Gamow factor), acts as a weight in the integrand of the reaction rate per particle pair (Eq. 32) and therefore represents the energy window over which most of the non-resonant thermonuclear reactions occur. In panel (a) the contributions of each term to the Gamow peak can be seen, while in panel (b) it is possible to distinguish the maximum of the peak at E_0 and its $1/e$ width Δ.

Maxwell-Boltzmann distribution $kT = 86.2$ keV, while the effective width of the energy window is $\Delta = 908$ keV.

IV. THE DETECTION TECHNIQUE

The advent of radioactive ion beams makes it possible to address many new questions in nuclear structure and nuclear astrophysics. When compared to measurements with stable beams, however, reactions induced by radioactive beams suffer from three difficulties: (1) low beam intensities, (2) large kinematic shifts, which occur through the need to use inverse reaction kinematics, i.e., heavier beams bombarding lighter targets, and (3) contaminants from neighboring elements or isotopes which are often present in radioactive ion beams. To eliminate some of these difficulties next-generation radioactive beam facilities with higher beam intensities are being built and new spectrometers optimized for inverse kinematic reactions are being developed. This chapter describes a method to address the difficulties that arise when secondary radioactive ion beams with contaminants from the primary stable ion beam (so-called 'cocktail beams') are used, through the simultaneous identification of the heavy reaction products with respect to mass and/or nuclear charge at very small scattering angles.

The use of inverse kinematics in studies with radioactive beams results in the beam-like reaction products being emitted at small angles. For some studies, such as measurements of (p, α) reactions at small angles, these products need to be separated from more abundant scattered beam particles. In experiments involving beams up to about mass 20 (e.g., $p(^{17}\mathrm{F},\alpha)^{14}\mathrm{O}$ [67]), where the opening angles for the beam-like particles are $\theta_{\mathrm{lab.}} \geq 6.5^{\circ}$, Si-strip detectors can be

used for detecting and identifying the outgoing particles. However, in experiments involving heavier beams (e.g., ^{4}He(^{44}Ti,p)^{47}V [68]), the opening angles are smaller and recoil separators have to be employed. While this technique provides excellent mass- and Z-identification the fact that only one charge state can be measured in the focal plane reduces the detection efficiency by a factor of about 5. In this work, a novel technique has been developed to address this challenge in the intermediate-mass regime ($A \sim 20$–40).

The possibility of using a magnetic spectrometer operating in the so-called gas-filled magnet (hereafter, GFM) mode for detecting the medium-mass recoil particles at very small scattering angles was therefore studied. In order to test this technique beams of stable nuclei (^{27}Al, ^{28}Si, ^{29}Si and ^{33}S) were first employed. Then, a ^{33}S beam was used for a first measurement of the p(^{33}S,α)^{30}P reaction, followed by a similar experiment with a low-intensity radioactive ^{37}K beam.

The principle of the GFM technique will be described in Sec. IV.1. The Split-Pole Spectrograph (hereafter, SPS) and its focal plane detector system which have been used in these experiments are explained in Sec. IV.2. The results obtained with medium mass ion beams are presented in Secs. IV.2.2, IV.2.3 and IV.2.4.

IV.1. The gas-filled magnet technique

The GFM technique has been used for several applications in the past. It was originally developed by Fulmer and Cohen [69, 70] for the separation of fission fragments and further refined by Armbruster and collaborators [71–73].

It has also been used in studies of heavy element production [74–77], for isobar separation in accelerator mass spectrometry [78–82], in sub-barrier fusion reactions in direct and inverse kinematics [83–85], and for light ion identification in (p, α) reactions [86]. In the present work the GFM method is applied for the first time to the identification of medium mass ions in measurements of (p, α) reactions of astrophysical interest.

The GFM technique consists of the deflection of charged particles moving through a magnetic field region which is filled with a gas at low pressure.

Incident ions of mass m and velocity v passing through matter (e.g., the target and foil window) emerge with a distribution of ionic charge states q [88]. After entering a magnetic spectrograph operated in vacuum ($\sim 10^{-6}$ Torr), the ions turn with a radius ρ given by the expression

$$B\rho = \frac{mv}{qe}, \tag{36}$$

where q is the charge state of the ion, B is the strength of the magnetic field and e is the elementary charge. Hence, nuclei of the same atomic number Z, mass number A and energy E but different q will have different magnetic rigidities $B\rho$, following different trajectories and being spatially distributed at the focal plane detector of the device as shown in Fig. 13(a). However, if the magnetic spectrograph is filled with a gas at low pressure ($\sim$ 10 Torr), an incident ion collides with the gas atoms several times along its trajectory, causing the charge state of each single ion to fluctuate due to electron capture and loss processes. If the number of collisions is high enough ($\gtrsim 10^4$, depending on the gas pressure and the atomic collision cross sections), the mean charge state $\bar{q}$ and average velocity

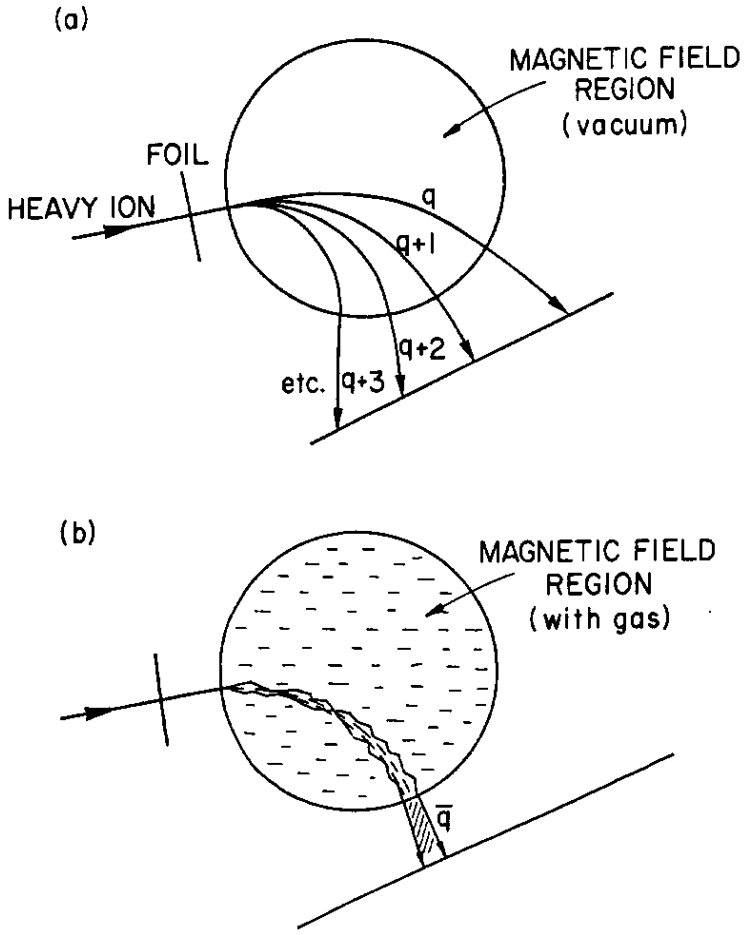

FIG. 13: Schematic illustration of the trajectories followed, after passing through a foil, by nuclei of the same Z, A and E in a magnetic field region: (a) in vacuum; (b) filled with gas. In vacuum, ions with different charge states will turn with different radii. In a gas-filled region, the ions will turn with a radius $\bar{\rho}$ associated to the mean charge state $\bar{q}$ and the average velocity $\bar{v}$. Taken from Ref. [87].

$\bar{v}$ of ions with same Z, A and E will be practically the same. Therefore, they will follow a trajectory with a radius $\bar{\rho}$, given by $B\bar{\rho} = m\bar{v}/(\bar{q}e)$, as is schematically represented in Fig. 13(b). Various semiempirical parameterizations have been derived for $\bar{q}$ which are summarized in Ref. [88, 89] and some of which are discussed in more detail in Sec. IV.2.2.

For particles in the velocity range $1 < v/v_0 < Z^{2/3}$ (where $v_0 = 2.19 \times 10^6$

m/s is the Bohr velocity) the average charge state $\bar{q}$ is in first order given by $\bar{q} \sim v/Z^{\alpha}$ with $\alpha \sim 0.4$ [88, 89]. Thus, a GFM disperses ions with different A and Z in the focal plane according roughly to $A/Z^{0.4}$. Due to their different path lengths in the magnetic field and their different specific energy loss (for ions with a different Z) the particles also experience a different time-of-flight between target and focal plane detector. Therefore, in a plot of time-of-flight vs. magnetic rigidity ions with different A and Z end up in different 'islands'. As an example, the distribution of several ion recoils in the time-of-flight vs. magnetic rigidity plane is shown in Fig. 14 as measured by K. E. Rehm *et al.* [86] with ^{16}O, ^{18}O and ^{18}F/^{18}O beams bombarding a CH_2 target, using a gas-filled magnetic spectrograph filled with N_2 at $P = 0.5$ Torr, and placed at $\Theta_{\text{lab.}} = 13^{\circ}$ ($B = 0.4544$ T). Groups of ^{12}C, ^{15}N, ^{15}O, ^{16}O, ^{18}O and ^{18}F ions are indicated.

Due to linear momentum conservation, in inverse kinematic reactions the heavy reaction products are constrained to very forward angles, and hence the spectrograph entrance window must be placed close to 0° to detect them. In such a situation, the beam also enters the spectrograph and after its separation from the beam-like reaction products of interest it must be blocked before reaching the focal plane detector to avoid the excessively high count rate that it would produce. With the spectrograph operated in vacuum mode, beam particles with different charge states follow different trajectories and arrive at different positions along the focal plane. Some trajectories originating from the different charge states of the reaction products could overlap with trajectories associated with some of the charge states of the beam. In this way, it would be impossible to block the higher-intensity beam particles without also blocking some of the reaction products of interest. Also, some charge states of these reaction products of interest would not be detected at the focal-plane detector because of its finite

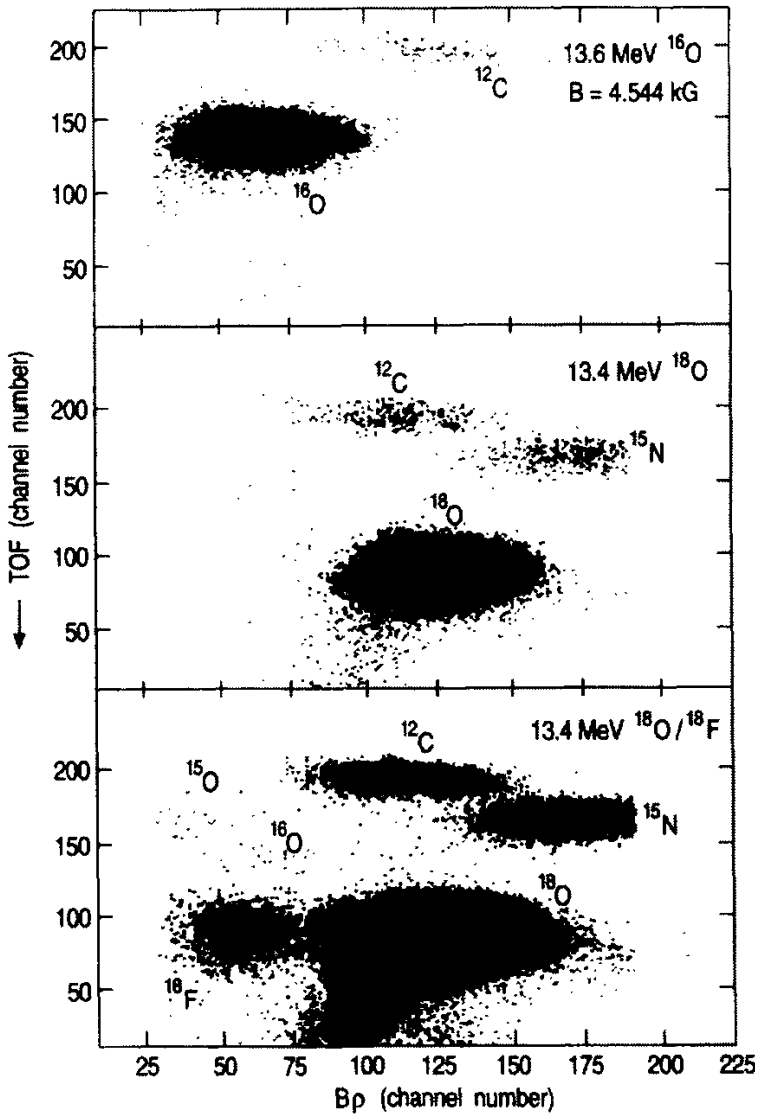

FIG. 14: Distribution of several elements and isotopes in the time-of-flight (TOF) vs. magnetic rigidity ($B\rho$) plane measured with ^{16}O (top), ^{18}O (middle) and ^{18}F/^{18}O (bottom) beams bombarding a CH_2 target, using a magnetic spectrograph filled with N_2 gas at $P = 0.5$ Torr, $\Theta_{\text{lab.}} = 13°$ and $B = 0.4544$ T. Taken from Ref. [86].

momentum acceptance.

The GFM method resolves those disadvantages when it is applied e.g. to the measurement of (p, α) transfer reactions with medium mass ion beams: all charge states of the same nuclear species are grouped at the focal plane, increasing the

detection efficiency which is essential in low-intensity radioactive experiments. Moreover, the magnetic rigidities of the beam particles and some of the reaction products of interest are sufficiently different to result in a spatial separation both groups in the focal plane. Therefore, through a proper selection of the magnetic field and/or partial shielding of the focal plane it is possible to focus the reaction products of interest onto the focal plane without detecting the beam particles, thereby avoiding prohibitively high counting rates.

Full advantage of the gas-filled spectrograph placed at 0° can be taken by using annular double-sided Si detectors (hereafter, DSSD) for the detection of the angular distributions of light reaction products. These annular detectors are divided into concentric rings and mounted coaxially with the beam, so that the azimuthal symmetry can be exploited, improving the count rate of the events of interest by a factor of around 10. A weakness of this technique is that, since the incident beam has to pass through a pressure foil at the entrance of the magnet, the beam intensity has to be kept below 10^7 particles/s in order to avoid breakage. This is not a severe restriction, however, since most of the radioactive ion beams presently available do not reach this limit.

IV.2. Test experiments with medium mass nuclei

The experiments described below were performed at the ATLAS facility at Argonne National Laboratory. An Enge split-pole magnetic spectrograph filled with N_2 gas at pressures between 10–20 Torr was used to identify the heavy residual nuclei at forward angles (see Fig. 24).While hydrogen or helium would

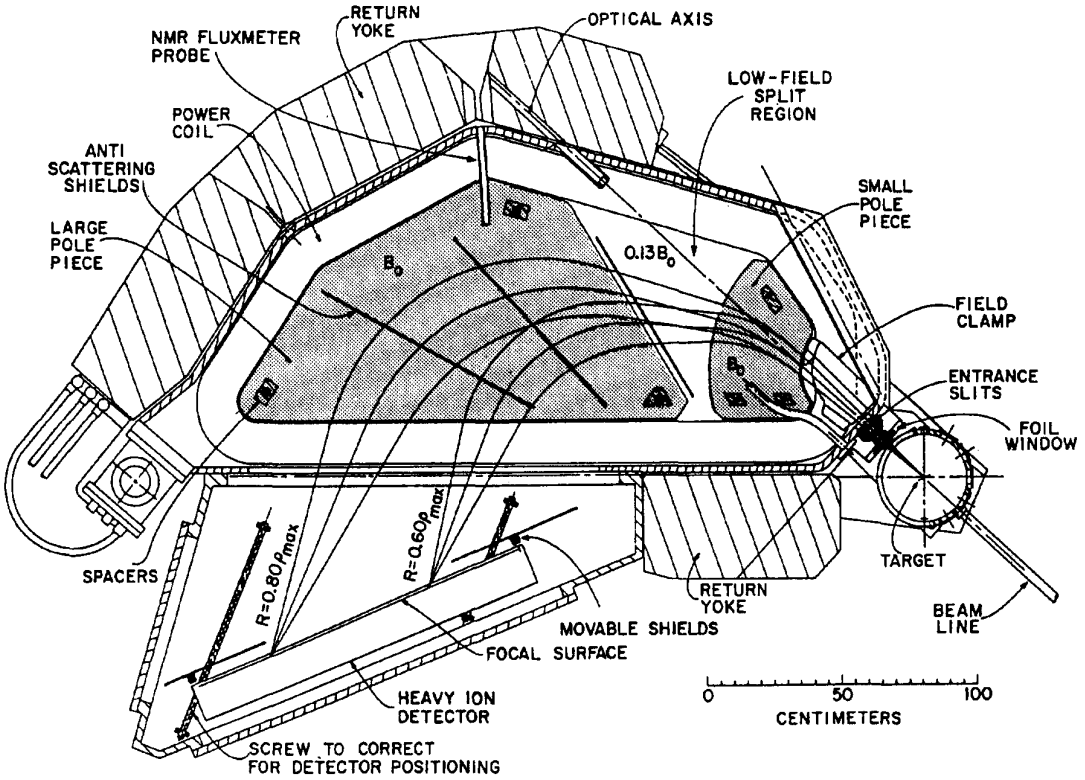

FIG. 15: Top view of the Enge split-pole spectrograph and scattering chamber located at the ATLAS facility. Trajectories corresponding to low and high magnetic rigidities accepted in the detectors are shown. The whole chamber of the magnet was filled with nitrogen gas at a pressure of 15 Torr. The foil window (1.3-g/cm^2 thick titanium) employed to contain the gas is indicated. The rectangular entrance slit to the spectrograph was located at 267 mm from the center of the scattering chamber. Its dimensions were 11.0-mm high and 1.70-mm wide in the GFM calibration runs, and 1.0-mm high and 13.5-mm wide in the ^{33}S$(p,\alpha)^{30}$P-reaction runs. Figure from Ref. [78].

have been a better choice for the GFM due to their lower charge, safety concerns and the existing cryo and sorption pumping system at the spectrograph prevented the use of these gases.

The heavy nuclei detected by the focal plane detector of the spectrograph were registered in coincidence with the light partners detected by an annular DSSD placed at forward angles in the scattering chamber (see Fig. 16). A schematic upper view of the focal plane detector is shown in Fig. 17. It consisted of an

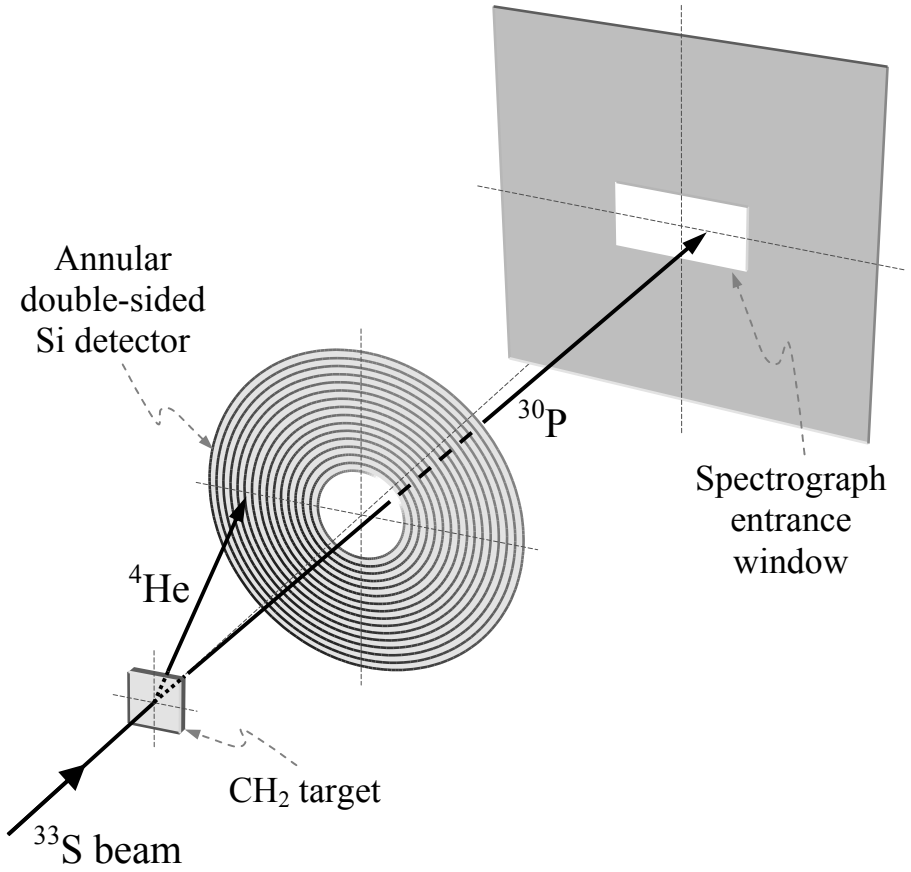

FIG. 16: A schematic of the experimental setup.

xy position-sensitive parallel grid avalanche counter (hereafter, PGAC) followed by an ionization chamber (hereafter, IC). The position at the focal plane X (proportional to the $B\rho$), the energy loss ΔE in the IC, and the time-of-flight TOF from the target to the focal plane were measured by the PGAC/IC detector and were used to identify the heavy reaction products.

IV.2.1. The split-pole spectrograph and its detector

Although not originally built as a gas-filled recoil separator the SPS is, due to its moderate dispersion, very well suited for the separation and detection

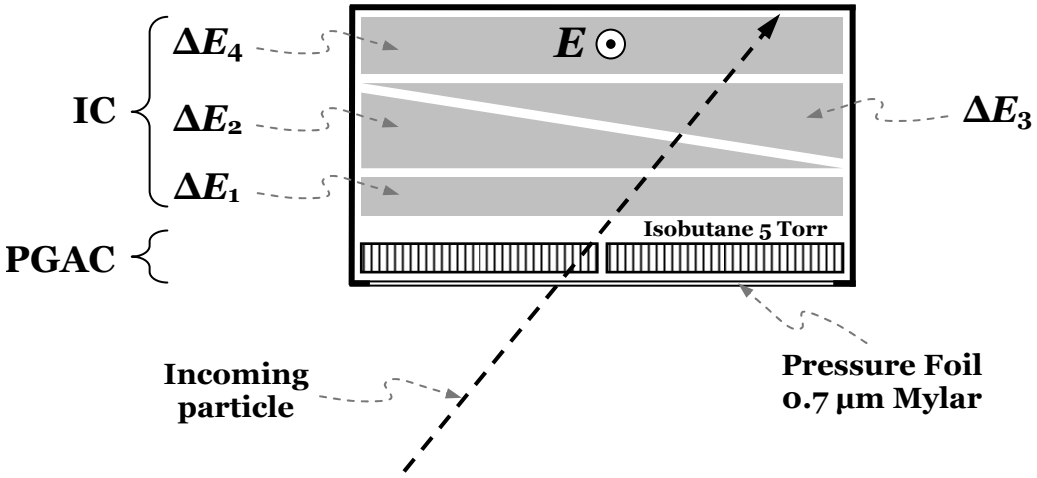

FIG. 17: Schematic upper view of the focal plane detector. It consists of a 5-cm thick x-y-position sensitive parallel grid avalanche counter (PGAC) filled with isobutane at a pressure of 3–5 Torr followed by a 30-cm deep multi-anode ionization chamber (IC). The PGAC also provides a fast timing signal which, together with the signal from the pulsed beam allows a determination of the time-of-flight from the target to the focal plane. The electric field (E) in the IC is perpendicular to the path of the incoming particles. The anode is subdivided in four strips allowing the measurement of multiple energy loss signals (ΔE_i).

of heavy ions. The spectrograph has a maximum solid angle of about 5 msr and accepts particles in the angular range $\delta\Theta = \pm 3.85°$. In the focal plane the particles are detected by a hybrid x-y-position sensitive detector system. It consists of a 5-cm thick x-y-position sensitive PGAC filled with isobutane at a pressure of 3–5 Torr [83] followed by a 30-cm deep multi-anode IC which is separated from the PGAC by a 6.25 μm mylar foil and filled with CF_4. The active area of the focal plane counter is 10×48 cm^2. Because of the large area of the window separating the IC from the PGAC the pressure in the IC has to be kept below 20 Torr. In addition to the x-y position information the PGAC provides also a fast timing signal which, together with the signal from the pulsed beam allows a determination of the time-of-flight from the target to the focal

plane. The electric field in the IC is perpendicular to the path of the incoming particle, which minimizes the drift time of the electrons and ions. The anode is subdivided in several strips allowing us to measure multiple ΔE signals for additional particle identification. This detector system has been used in the past for measurements of evaporation residues from heavy-ion induced fusion reactions [83] and more details of the detector can be found in this reference.

IV.2.2. GFM calibration runs

In order to obtain a better understanding of the energy and Z-dependence of the average charge state $\bar{q}$, a series of calibration runs were performed by bombarding a ^{197}Au target with ion beams of ^{27}Al, ^{28}Si and ^{29}Si at $E_{\text{lab.}} = 10$ MeV/nucleon and detecting elastically scattered particles at $\Theta_{\text{lab.}} = 2°$. The results of these test runs also served as a check as to whether the experimental results in the mass and energy range of interest in this work could be simulated by calculations carried out with the code RAYTRACE-GFM [87, 90, 91].

The RAYTRACE-GFM code calculates trajectories of heavy ions travelling through different types of ion-optical devices (dipoles, multipoles, electrostatic deflectors, velocity filters, lens and solenoids) filled with low-pressure gas. In our case, using a detailed configuration of the magnetic field regions of the SPS, the trajectories are calculated by integrating the equation of motion of the ions

$$\frac{d\,(m\boldsymbol{v})}{dt} = q\,(\boldsymbol{B} \times \boldsymbol{v}) - \frac{dE}{dx}\frac{\boldsymbol{v}}{v}. \tag{37}$$

The simulation of the ion-gas interaction process is performed with a standard Monte Carlo method, using Gaussian-shaped equilibrium charge-state distribu-

tion

$$F_q = \frac{1}{d\sqrt{2\pi}} \exp\left(-\frac{(q-\bar{q})^2}{2d^2}\right) \tag{38}$$

where $\bar{q}$ is the average charge state and d is the standard deviation of the distribution.

Different semiempirical parameterizations for $\bar{q}$ and d can be chosen to perform the calculations. Among them are:

i) the Betz parameterization [88, 92, 93]

$$\bar{q} = Z\left[1 - C\exp\left(A\frac{(v/v_0)^\delta}{Z^\gamma}\right)\right] \tag{39}$$

$$d = d_1 Z^w, \tag{40}$$

where $C = 1$, $A = 0.555$, $\delta = 1.175$, $\gamma = 0.607$, $d_1 = 0.27$ and $w = 0.5$ are parameters evaluated from experimental data in nitrogen gas and $v_0 = 2.19\times10^6$ m/s is the Bohr velocity;

ii) the Dmitriev-Nikolaev parameterization [94]

$$\bar{q} = Z\left[\frac{\log\left((v/v_0)\,Z^{\alpha_1}/m_1\right)}{\lg\left(n_1 Z^{\alpha_2}\right)}\right] \tag{41}$$

$$d = d_1 Z^w, \tag{42}$$

with $\alpha_1 = 0.4$, $\alpha_2 = 0.3$, $m_1 = 0.41$, $n_1 = 7$, $d_1 = 0.32$ and $w = 0.45$ in nitrogen gas;

and *iii*) the Schiwietz parameterization [95]

$$\bar{q} = Z\frac{376x + x^6}{1428 - 1206x^{0.5} + 690x + x^6} \tag{43}$$

with

$$x = \left(v/v_0 Z^{-0.52} Z_{gas}^{0.03-0.017Z^{-0.52}v/v_0}\right)^{1+0.4/Z}, \tag{44}$$

and

$$d = \frac{0.7}{Z^{-0.27} Z_{gas}^{0.035-0.0009Z} f(\bar{q}) f(Z - \bar{q})} \tag{45}$$

where

$$f(x) = \sqrt{\left(x + 0.37Z^{0.6}\right)/x}. \tag{46}$$

This last parameterization has been recently incorporated into the code in this work, for experiments with medium-mass nuclei.

Elastically scattered particles at $\Theta_{\text{lab.}} = 2^\circ$ were detected in the focal-plane detector of the SPS filled with N_2 at a pressure $P = 15$ Torr and at several different strengths of B field in the range 0.95 – 1.16 T. Examples of typical experimental two-dimensional spectra of TOF vs. X are given in Fig. 18. This figure shows a superposition of three different spectra obtained using ^{27}Al, ^{28}Si and ^{29}Si beams at $B = 1.1602$, 1.0782 and 1.0566 T, respectively. Under such conditions, the detected events associated with each beam are statistically distributed on the TOF vs. X plane in three groups with different locations. Experimental mean values of focal-plane position distribution $\bar{\text{X}}$ and time-of-flight distribution $\bar{\text{TOF}}$ as a function of the field strength B obtained for these three nuclei are shown in open symbols in Figs. 19(a) and 20(a), respectively. The solid, dashed

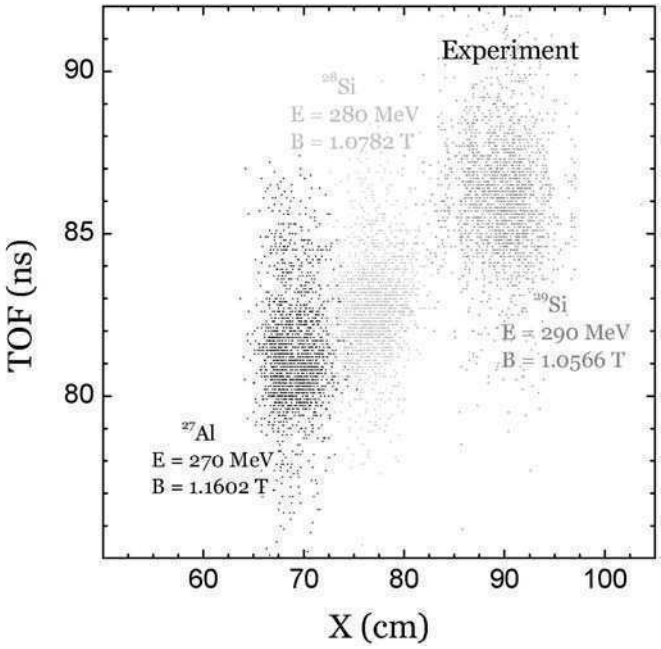

FIG. 18: Locations of particle groups in the TOF vs. X plane. Superposition of three different experimental spectra, taken from ^{27}Al, ^{28}Si and ^{29}Si elastically scattered on a ^{197}Au target at $\Theta_{\text{lab.}} = 2°$, $E_{\text{lab.}} = 10$ MeV/nucleon, $P = 15$ Torr and $B = 1.1602$, 1.0782 and 1.0566 T respectively.

and dotted lines exhibit the results of the RAYTRACE-GFM calculations which are discussed below.

RAYTRACE-GFM calculations of $\bar{\text{X}}$ and $\text{T}\bar{\text{O}}\text{F}$ as a function of the field strength B are shown and compared with experimental results in Figs. 19 and 20, respectively. Panels (a), (b) and (c) correspond, in that order, to the Betz, Schiwietz and Dmitriev models for the charge state distribution; solid, dotted and dashed lines were used, respectively, for ^{27}Al, ^{28}Si and ^{29}Si beams. As can be seen from the figures, the calculations using the Betz and Schiwietz models are in very good agreement with the experimental data, while the calculations of both $\bar{\text{X}}$ and $\text{T}\bar{\text{O}}\text{F}$ for the Dmitriev model are systematically shifted to smaller values. It must be noted, however, that the validity of the Dmitriev model covers only the range $0.3 \lesssim \bar{q}/Z \lesssim 0.9$ [94], which translates to a region in projectile velocity

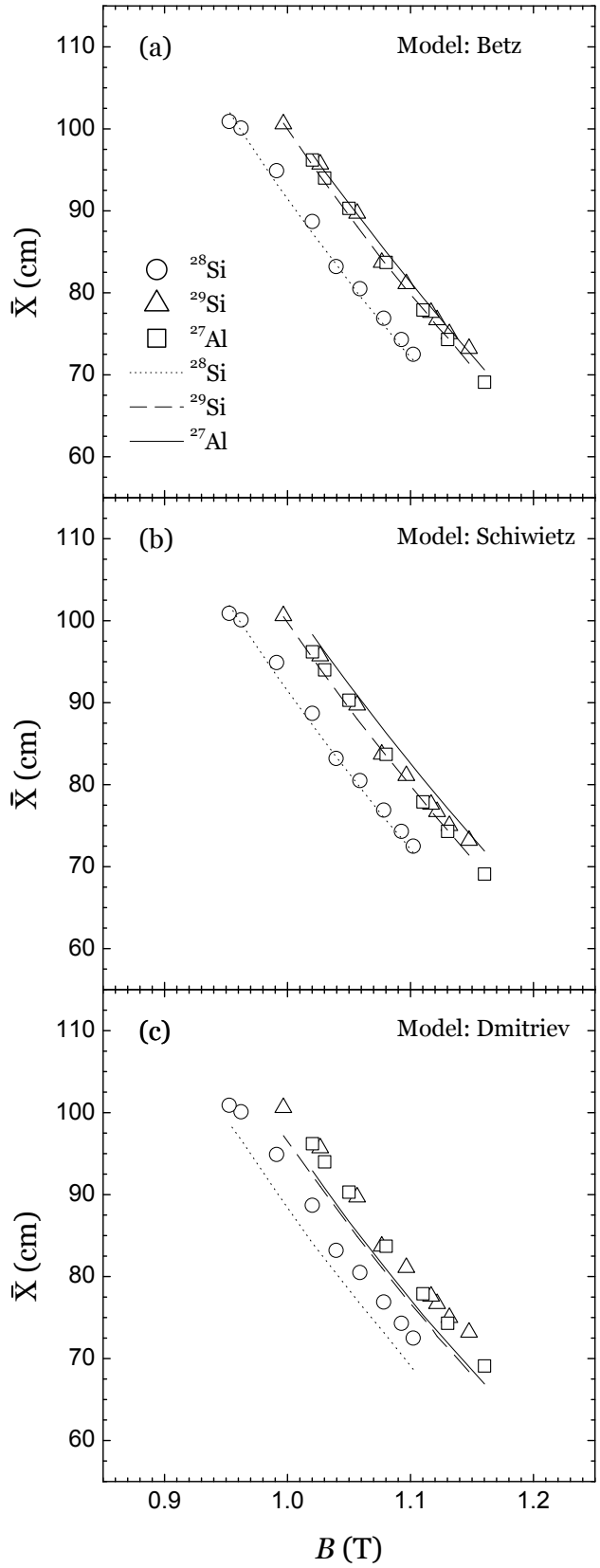

FIG. 19: Mean values of focal-plane position distributions plotted as a function of the magnetic field. Experimental results (symbols) and calculations (lines) are presented for three different beams: ^{27}Al (open squares and solid line), ^{28}Si (open triangles and dotted line) and ^{29}Si (open circles and dashed line). Panels (a), (b) and (c) correspond, in that order, to calculations using the Betz, Schiwietz and Dmitriev charge state distributions.

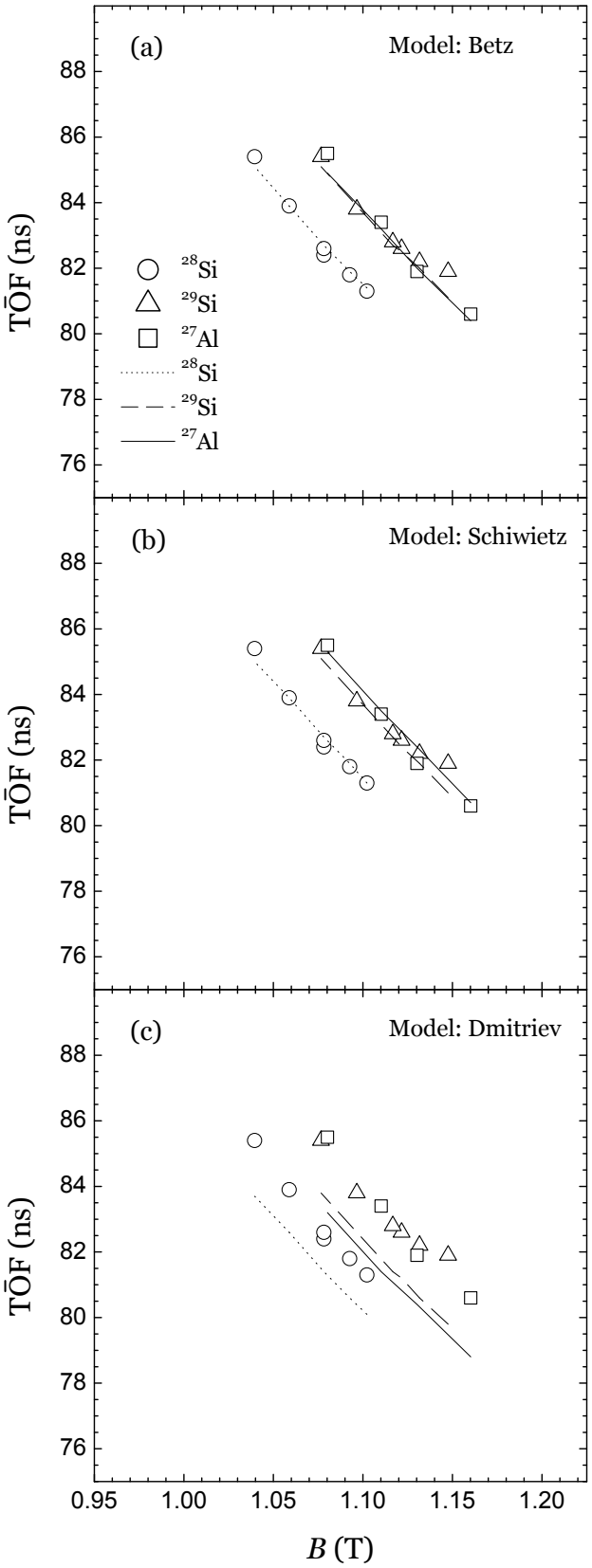

FIG. 20: Mean values of time-of-flight distributions plotted as a function of the magnetic field. Experimental results (symbols) and calculations (lines) are presented for three different beams: ^{27}Al (open squares and solid line), ^{28}Si (open triangles and dotted line) and ^{29}Si (open circles and dashed line). Panels (a), (b) and (c) correspond, in that order, to calculations done using the Betz, Schiwietz and Dmitriev charge state distributions.

equivalent to $2.6 \lesssim v/v_0 \lesssim 13$. At the bombarding energy used in this GFM calibration (10 MeV/nucleon) the projectile velocity is $v/v_0 = 20$ and therefore $\bar{q}$ is overestimated when calculated by Eq. 41. For instance, for ^{27}Al it gives $\bar{q}/Z = 1.05$ which corresponds to an unphysical value. In Eq. 36, an excessively high $\bar{q}$ leads to a smaller radius and, hence, the mean value of the focal-plane position $\bar{\mathrm{X}}$ is shifted towards smaller values. Also, smaller radii lead to shorter path lengths and therefore to smaller values of $\bar{\mathrm{TOF}}$. On the other hand, the Betz and Schiwietz parameterizations are valid in the range $v/v_0 \gtrsim 1$ [88, 95], which includes the velocities used in this experiment, and at $v/v_0 = 20$ the experimental data are still successfully described. A closer inspection of Figs. 19 and 20 shows that the centroids in X and TOF distributions, in particular the overlap between the ^{27}Al and ^{29}Si data, are better described by the Betz parameterization. For that reason this parameterization (given by Eq. 39) has been chosen for $\bar{q}$ in the RAYTRACE-GFM calculations explained below.

Other important input parameters for the RAYTRACE-GFM calculations are the variances of the X and TOF parameters. For the width of the time distribution a variance σ of 1 ns was assumed, which is based on previous experience with the ATLAS accelerator. The width of the X distribution is determined by the width of the q distribution which can be calculated from the parameters d in Eqs. 40, 42 and 45. A comparison of the experimental data with the predictions of Betz, Dimitriev and Schiwietz is shown in Fig. 21. In this comparison it has to be kept in mind that the widths depend on many parameters, e.g. the stopping gas, the type of the ion, etc. In the following, the Schiwietz parameterization has been used for the widths, which gives the best agreement with the data for the ions studied in this work.

Figure 22 shows a comparison of the experimental results for the two-dim-

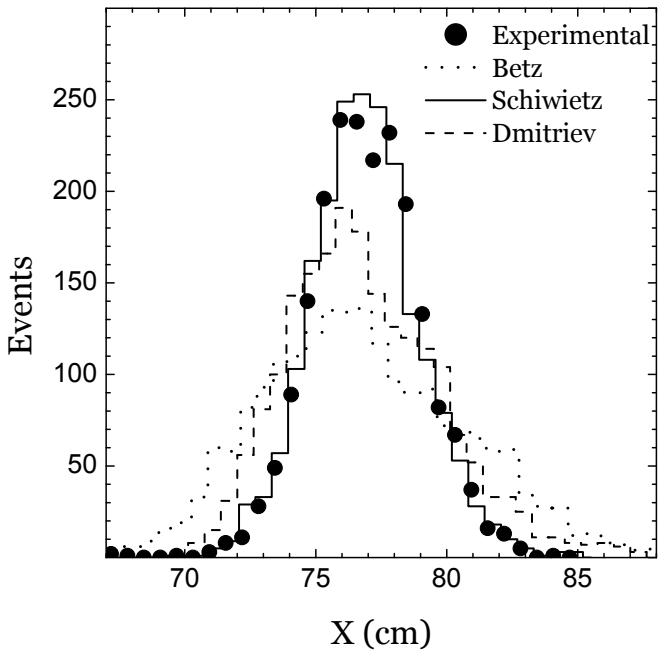

FIG. 21: X distributions, in GFM mode, of ^{28}Si particles elastically scattered on a ^{197}Au target at $\Theta_{\text{lab.}} = 2°$, $E_{\text{lab.}} = 10$ MeV/nucleon, $P = 15$ Torr and $B = 1.0782$ T. The full symbols are the experimental spectrum, while the dotted, solid and dashed lines correspond to calculations using the Betz, Schiwietz and Dmitriev charge state distributions, respectively. The distributions were normalized to have the same number of counts as the experimental spectrum. Only the width obtained with the Schiwietz charge state distribution agrees with the data.

ensional spectra of TOF vs. X and the predictions from RAYTRACE-GFM using the Betz parameterization for the mean charge state $\bar{q}$ and the Schiwietz parameterization for the width parameter d (Betz-Schiwietz model), for the superposition of ^{27}Al, ^{28}Si and ^{29}Si beams at $B = 1.1602$, 1.0782 and 1.0566 T, respectively. It is apparent from these pictures that with the exception of the tails towards longer flight times in the experimental spectrum, which are caused by the finite TOF acceptance of the accelerator, good agreement with the theoretical predictions is obtained for this energy and mass range.

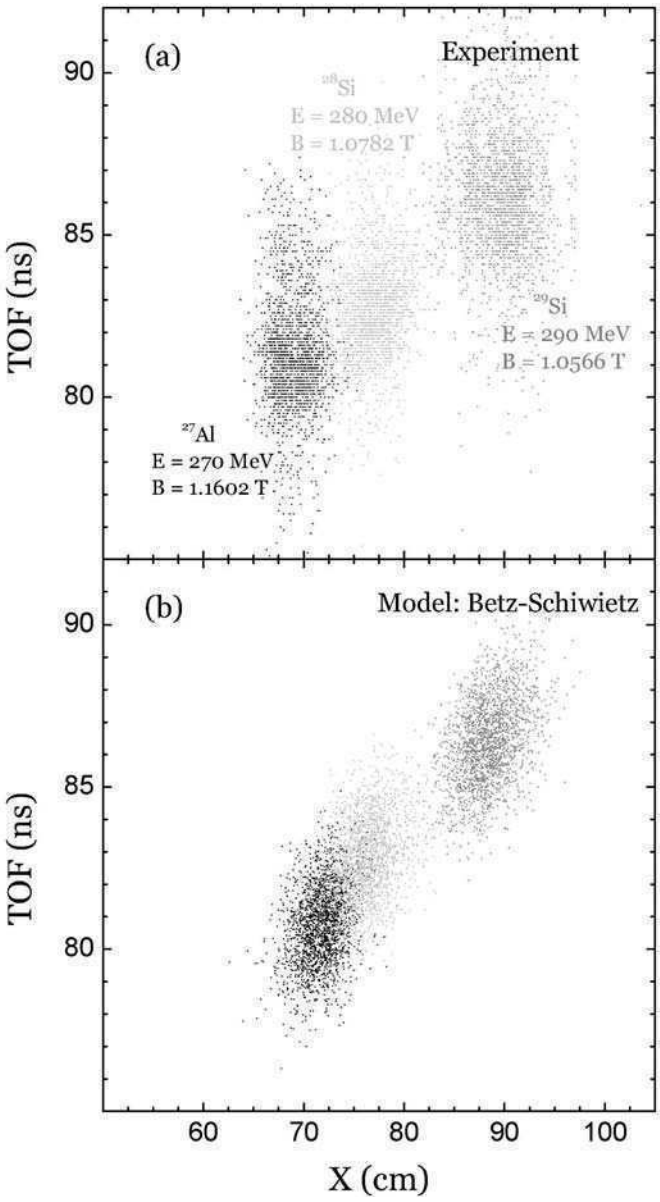

FIG. 22: Scatter plots of events in the TOF vs. X plane for ^{27}Al, ^{28}Si and ^{29}Si ions detected in the gas-filled split-pole spectrograph. Panel (a): superposition of three different experimental spectra, taken from ^{27}Al, ^{28}Si and ^{29}Si elastically scattered on a ^{197}Au target at $\Theta_{\text{lab.}} = 2°$, $E_{\text{lab.}} = 10$ MeV/nucleon, $P = 15$ Torr and $B = 1.1602$, 1.0782 and 1.0566 T respectively. Panel (b): RAYTRACE-GFM calculations using the Betz parameterization for the mean charge state $\bar{q}$ and the Schiwietz parameterization for the width parameter d (model Betz-Schiwietz), for the same particle groups and in the same conditions of panel (a). Good agreement with the theoretical predictions is obtained for this energy and mass range.

IV.2.3. Particle identification with a stable ^{33}S beam: the $^{33}S(p,\alpha)^{30}P$ reaction

After these calibration runs with ^{27}Al, ^{28}Si and ^{29}Si beams this technique was tested by using the reaction $p(^{33}\mathrm{S},^{30}\mathrm{P})\alpha$, with a ^{33}S ion beam incident on a 360-μg/cm^2 CH_2 target with a 50-μg/cm^2 Au backing foil. Fig. 23 shows the kinematic correlation between detection angle and energy for the α particles and ^{30}P reaction products calculated for a ^{33}S bombarding energy of 179 MeV. Because of the choice of inverse kinematics, these kinematic curves have both a low and a high energy solution at each angle. Small center-of-mass angles correspond to the high-energy part of the heavy recoils (i.e., to the low-energy solution for the α's). As can be seen from Fig. 23(a), the α particles are restricted to a cone with an opening angle of about 24° while, from Fig. 23(b), the heavy reaction products ^{30}P are more forward peaked with a maximum angle of about 3.1°. The acceptance limits of the annular Si-detector and the spectrograph are indicated by the dotted (α's) and dashed (^{30}P) lines, respectively. Since with a stable ^{33}S beam intensities in excess of 10^7 particles/s were available, the spectrograph was moved away from 0° in order to avoid entrance foil breakage. The angular range covered with the GFM was $0.5° \leq \Theta_{\mathrm{lab.}} \leq 3.5°$. As schematically shown in Fig. 24, the reaction products were spatially separated from the ^{33}S particles elastically scattered on the target. The majority of the ^{33}S particles were blocked before the entrance foil of the PGAC in order to avoid prohibitively high counting rates in the focal plane detector. Only a small fraction of the ^{33}S particles, those that were scattered on the edge of shield, entered the focal plane detector.

Figure 23(c) shows that within the acceptance range of the Si detector, $7.9° \leq \theta_{\mathrm{lab.}} \leq 23.4°$, the energies of the corresponding ^{30}P particles range from

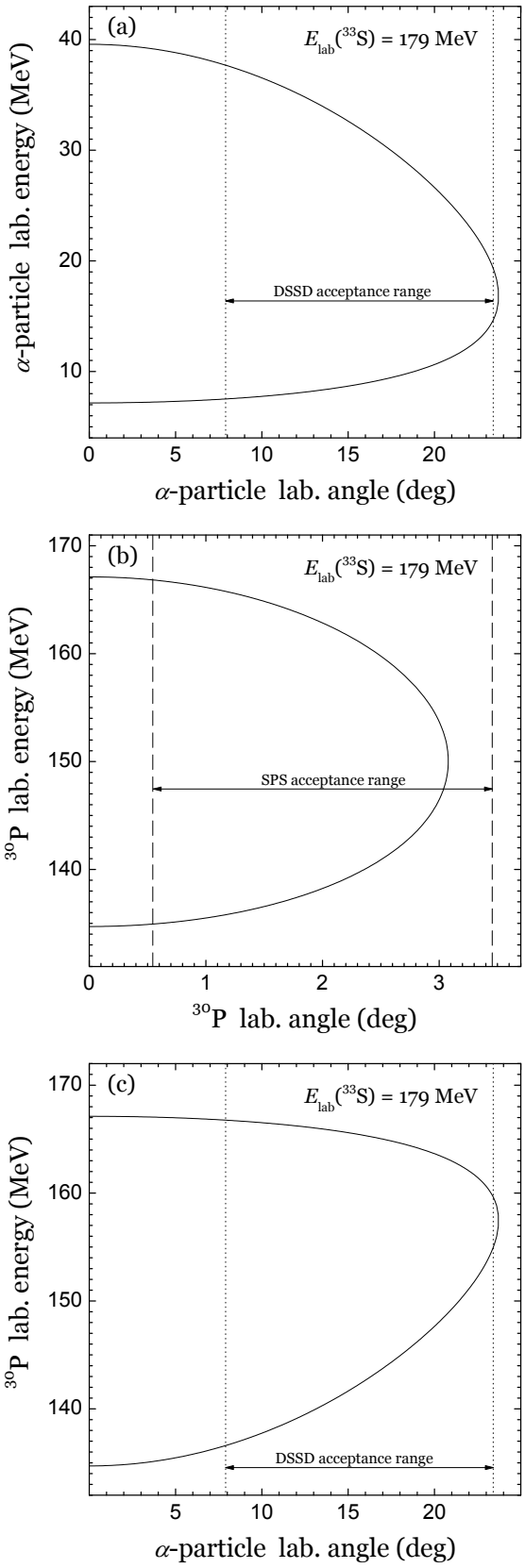

FIG. 23: Kinematic relations between detection angle and energy for the products of the $p(^{33}S,^{30}P)\alpha$ reaction at 179 MeV. Panel (a): Energy vs. emission angle for the α particle. Panel (b): Energy vs. emission angle for the ^{30}P recoil. Panel (c): Energy of the ^{30}P vs. emission angle of the α particle. The energies and angles are expressed in the laboratory system. Acceptance limits of the DSSD and SPS are indicated.

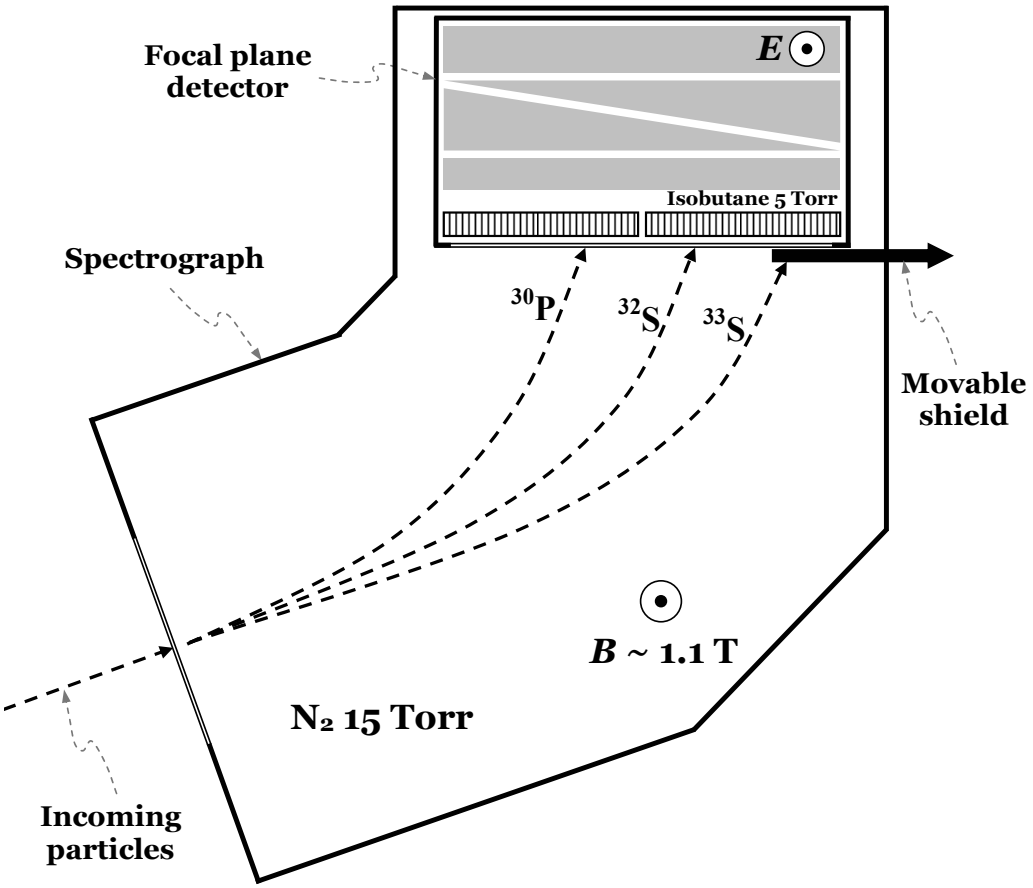

FIG. 24: Schematic of the isotope separation in the spectrograph filled with nitrogen gas at a pressure of 15 Torr and a magnetic field of around 1.1 T. Most of the ^{33}S particles were blocked before the entrance foil of the PGAC by means of a movable shield, while the ^{30}P particles entered the focal plane detector.

136.6 to 166.8 MeV. With this information RAYTRACE-GFM calculations were performed in order to predict where the ^{30}P reaction products and the elastic scattered ^{33}S would appear in a two-dimensional spectrum of TOF vs. X. The results are shown in Fig. 25(a). Due to a problem with the time-to-amplitude converter no TOF signal was available during this run. Since the focal plane detector in the spectrograph can also provide an energy-loss signal from the ionization chamber a calculation of a spectrum of ΔE vs. X was performed (Fig. 25(b)). An experimental spectrum of the same parameters is shown in

Fig. 25(c) at a ^{33}S bombarding energy of 202.0 MeV. The experimental spectrum includes only the heavy particles detected in the focal plane detector which had a light particle detected in coincidence in the DSSD. This filtering process was done by gating a time spectrum between the detection of a light particle at the DSSD and a heavy particle at the focal plane detector. The agreement between both the experimental and simulated spectra confirms that the heavy particle of interest was successfully separated from the beam-like particles by the focal plane detector with the spectrograph in gas-filled mode.

In order to identify the α-particles from the reaction of interest, an additional gate in the ^{30}P branch of the ΔE_1 vs. X spectra was applied. In this most of the background events in the emission angle vs. energy spectra acquired by the DSSD were eliminated. Figure 26 presents three different DSSD two-dimensional spectra for ^{33}S bombarding energies of 160.9, 171.1 and 179.0 MeV. The solid lines are the kinematic relations between the emission angle and the energy expected for population of the ground state, while the three subsequent dotted lines represent transitions to the first three excited states in ^{30}P. As can be seen there are groups of light particles detected in the DSSD which are consistent, in a wide energy range, with the kinematic curves corresponding to the ground state transitions in the ^{33}S$(p,\alpha)^{30}$P reaction.

This result confirms that the technique developed in this work can be applied successfully to the identification of (α, p) reaction by means of the time-inverse reaction and in inverse kinematics in a middle mass range. The events grouped as almost vertical lines at low energies in Fig. 26 correspond to inelastic excitations of ^{33}S from the $p(^{33}$S,$p)^{33}$S$'$ reaction which are present as a background in Fig. 25(c). From these spectra angular distributions can be obtained, which, after integration, result in an excitation function for the ^{33}S$(p,\alpha)^{30}$P reaction,

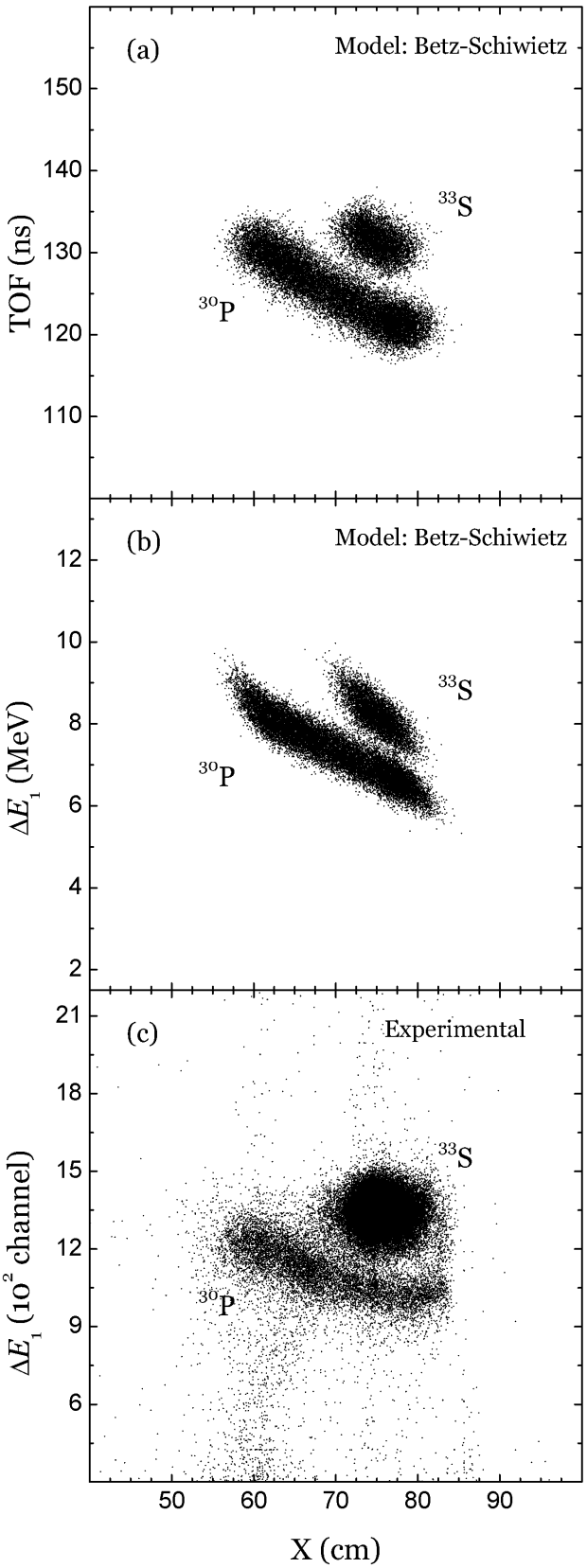

FIG. 25: Panels (a) and (b): Spectra of TOF and energy loss in the first anode (ΔE_1) vs. X calculated with the code RAYTRACE-GFM for the $p(^{33}\mathrm{S}, \alpha)^{30}\mathrm{P}$ reaction at a bombarding energy of 202.0 MeV. Islands of ^{30}P from the reaction of interest and ^{33}S from elastic scattering are shown. Panel (c): Experimental spectrum of ΔE_1 vs. X for the $p(^{33}\mathrm{S}, \alpha)^{30}\mathrm{P}$ reaction, gated with the time spectrum requiring coincidence, taken at a ^{33}S bombarding energy of 202.0 MeV. The spectra show the separation of the particles of interest that can be achieved with the GFM technique. A gate in the ^{30}P island was applied to identify α-particles of interest detected in the DSSD spectra.

as will be shown in Sec. V.4.

IV.2.4. Particle identification with a radioactive ^{37}K beam: the $^{37}K(p,\alpha)^{34}Ar$ reaction

Following this 'proof of principle' test of the GFM technique with a stable ^{33}S beam, a similar measurement of the ^{37}K$(p,\alpha)^{34}$Ar reaction using a radioactive beam of ^{37}K ($t_{1/2} = 1.22$ s) was performed. The secondary beam was produced via the $d(^{36}\mathrm{Ar},^{37}\mathrm{K})n$ reaction by bombarding a cryogenically cooled gas cell filled with 1.4 atm of deuterium with a 360-MeV beam of ^{36}Ar obtained from the ATLAS accelerator [96]. The ^{37}K particles were separated from the primary ^{36}Ar beam using a 22° bending magnet which was set to transport the $^{37}\mathrm{K}^{19+}$ ions to the target. The majority of the fully-stripped primary beam $^{36}\mathrm{Ar}^{18+}$ has a higher magnetic rigidity and is therefore not transmitted. However, energy-degraded $^{36}\mathrm{Ar}^{18+}$ ions will fall into the acceptance window of the bending magnet and will also be transported to the target, although with a different energy and time of flight. In order to eliminate some of these background events from the secondary beam of interest, an RF-sweeper has been installed in the beam line [97]. The RF phase was set to let the particles of interest $^{37}\mathrm{K}^{19+}$ pass through the RF-sweeper while the slower $^{36}\mathrm{Ar}^{18+}$ ions experience a vertical deflection and are stopped on a pair of slits located downstream of the sweeper. The intensity of the radioactive beam on target was typically 5×10^4 ^{37}K/s. Details of this in-flight technique can be found in Ref. [96].

The experimental setup used in this measurement was the same as the one used in the $p(^{33}\mathrm{S},\alpha)^{30}$P experiment shown in Fig. 16. Since the beam intensity

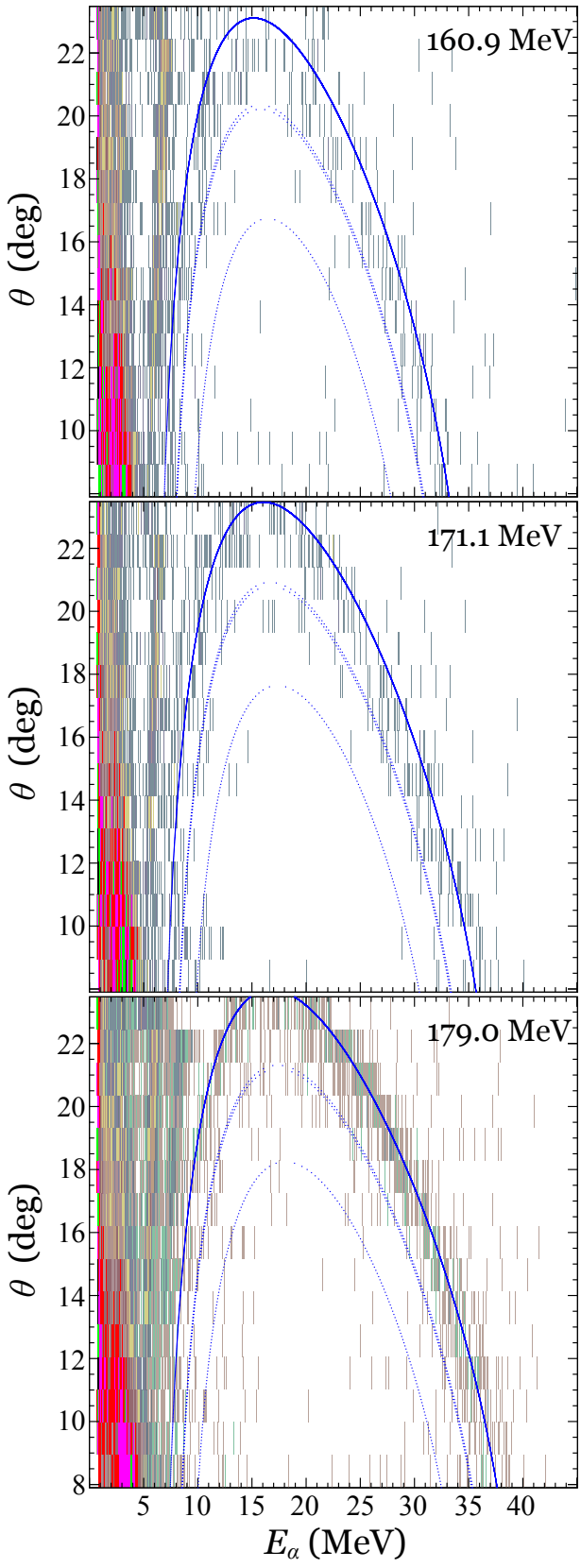

FIG. 26: Two-dimensional spectra of angle and energy of the particles detected at the DSSD, corresponding to events in coincidence (time gated) and within the ^{30}P island (ΔE_1-X gated). The ^{33}S bombarding energy of each spectrum is indicated. Experimental events are displayed as vertical segments. The θ binning represents the angular range covered by each DSSD rings. The blue lines are calculations of the $^{33}\mathrm{S}(p,\alpha)^{30}\mathrm{P}$ kinematics with excitation energy corresponding to the ground state (solid line) and the first three excited states (dotted lines) of ^{30}P. These results demonstrate that light particles detected in the DSSD follow the kinematic curves of the $^{33}\mathrm{S}(p,\alpha)^{30}\mathrm{P}$ reaction in a wide energy range, and confirm that this technique can be applied successfully to measure (α,p) transfer reactions in inverse kinematics and by means of the time-inverse reaction.

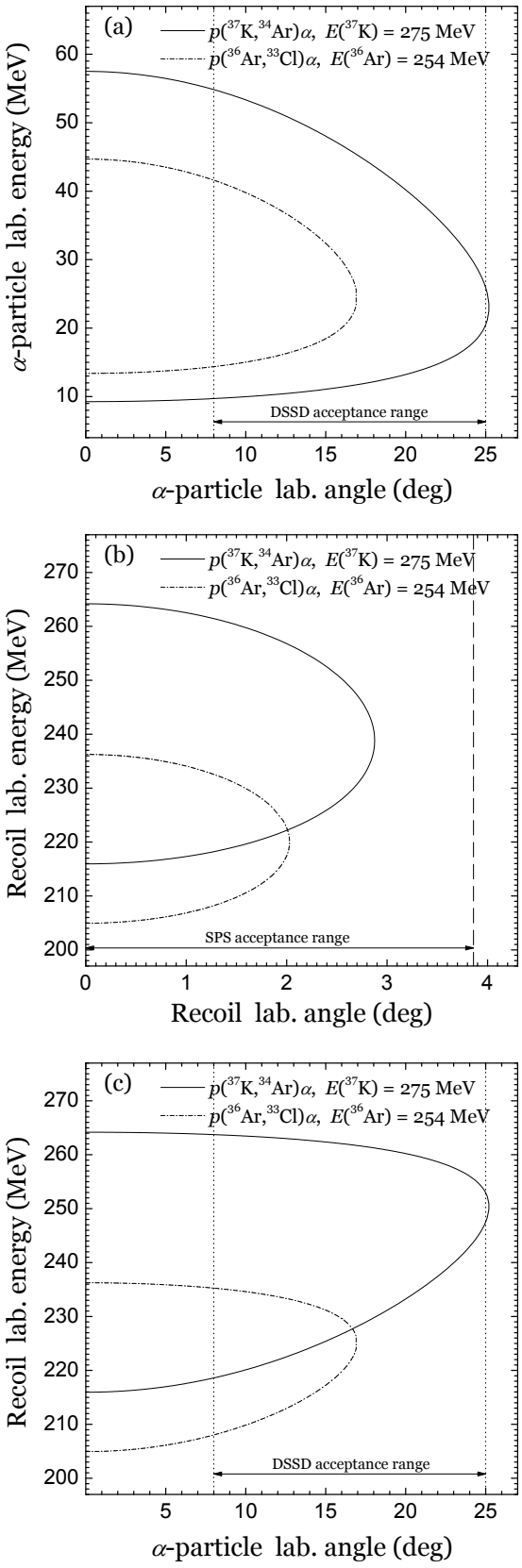

FIG. 27: Kinematic relations between detection angle and energy for the products of the $p(^{37}\mathrm{K},^{34}\mathrm{Ar})\alpha$ and $p(^{36}\mathrm{Ar},^{33}\mathrm{Cl})\alpha$ reactions at 275 and 254 MeV, respectively. Panel (a): Energy vs. emission angle for the α particle. Panel (b): Energy vs. emission angle for the ^{34}Ar and ^{37}K recoils. Panel (c): Energy of the ^{34}Ar and ^{37}K recoils vs. emission angle of the α particle. The energies and angles are expressed in the laboratory system. Acceptance limits of the DSSD and SPS are indicated.

of the secondary ^{37}K beam was only about 10^5 particles/s the spectrograph could be located at 0° with the ^{37}K/^{36}Ar cocktail beam entering the GFM. The kinematic correlations between emission angle and energy for the (p, α) reaction with a ^{37}K beam are given in Fig. 27. The angular distribution of the ^{37}K particles in the laboratory frame is restricted to scattering angles less than 2.9°, i.e., to a region where Si detectors are hard to use. In order to identify the region in a ΔE vs. X plot where ^{34}Ar reaction products can be expected RAYTRACE-GFM calculations were performed including elastic scattering events from both, the ^{37}K and ^{36}Ar beams as well as the corresponding ^{34}Ar and ^{33}Cl products from the corresponding (p, α) reactions. The energies of the incoming ^{37}K and ^{36}Ar beams were 275 MeV and 254 MeV, respectively. The results for ΔE vs. X are shown in the top part of Fig. 28 in comparison with the experimental results (bottom). In order to eliminate tails from the primary beam only events corresponding to the high-energy part of the kinematic curve (see e.g. Fig. 27) are shown in the lower part of Fig. 28. Since (*a*) the beam intensity of the contaminant ^{36}Ar beam was only 20% of that of the radioactive ^{37}K beam and (*b*) the corresponding ^{36}Ar energy was about 10% lower, the reaction products from the ^{36}Ar$(p, \alpha)^{33}$Cl reaction had a negligible count rate. In this comparison it should be kept in mind that the experiment was done with ^{37}K beam intensities that were smaller by 3 to 5 orders of magnitude than comparable stable beam experiments. Despite the poor statistics the structure of the experimental spectrum is found to be in good agreement with the calculations.

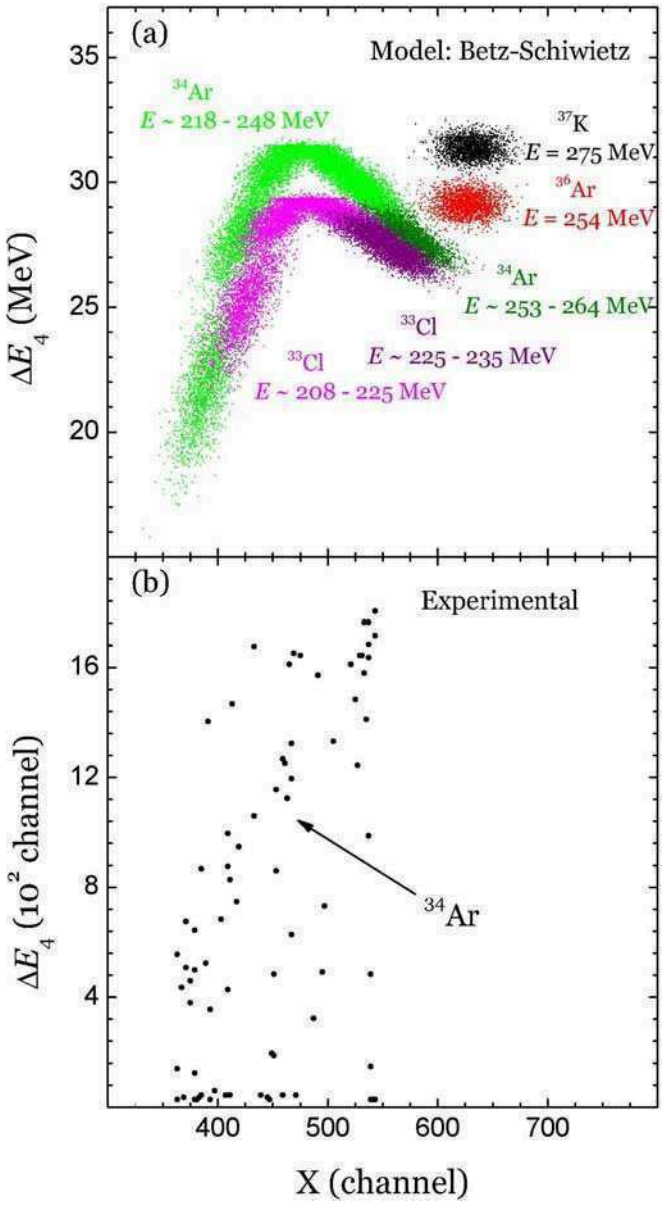

FIG. 28: Calculated two-dimensional spectra of TOF vs. X (a) and ΔE_4 vs. X (b), obtained using the code RAYTRACE-GFM, for the recoils of the $p(^{37}\mathrm{K},^{34}\mathrm{Ar})\alpha$ and $p(^{36}\mathrm{Ar},^{33}\mathrm{Cl})\alpha$ reactions at 275 and 254 MeV, respectively. Groups of ^{34}Ar and ^{33}Cl together with islands of ^{37}K and ^{36}Ar from elastic scattering are indicated.

V. CROSS SECTION MEASUREMENT

Using the technique described in the previous chapter, the reaction $^{33}\mathrm{S}(p,\alpha)^{30}\mathrm{P}$ was studied in inverse kinematics at five ^{33}S-bombarding energies in the range 150–202 MeV. The results will be presented in this chapter. Firstly, in Sec. V.1, the method used for the normalization of the cross sections will be described. After that, the detection efficiency and its calculation and the results will be explained and presented in Secs. V.2 and V.3, respectively. Then, the procedure for determination of the ground-state-to-ground-state (hereafter, g.s. to g.s.) differential and total cross sections for the $^{33}\mathrm{S}(p,\alpha)^{30}\mathrm{P}$ reaction from a direct measurement will be described in Sec. V.4 and the results will be presented. The total cross sections for the g.s. to g.s. time-reverse reaction $^{30}\mathrm{P}(\alpha,p)^{30}\mathrm{S}$, calculated using the reciprocity theorem, will be given in Sec. V.5. The experimental excitation functions of both reactions will also be compared with theoretical predictions.

V.1. Normalization

During the measurements performed to determine the differential cross section of the $^{33}\mathrm{S}(p,\alpha)^{30}\mathrm{P}$ reaction, $\left(\frac{d\sigma}{d\Omega}\right)_{p^{33}\mathrm{S}}$, the ^{33}S-beam flux J was determined by monitoring the elastically scattered ^{33}S particles on the ^{197}Au backing of the

CH_2Au target by means of a monitor detector with a solid angle $\Omega_{\rm mon}$ placed at a polar angle $\theta_{\rm mon}$. This angle $\theta_{\rm mon}$ was equal to 41° in the laboratory frame, small enough as to ensure that the elastic scattering of the ^{33}S + ^{197}Au system was pure Rutherford scattering for all the ^{33}S bombarding energies. For the differential cross section of the Rutherford scattering of the ^{33}S + ^{197}Au system, $\left(\frac{d\sigma}{d\Omega}\right)^{\rm Ruth}_{^{33}S^{197}Au}$, a similar expression to Eq. 2 can be written, i.e.,

$$\left(\frac{d\sigma}{d\Omega}\right)^{\rm Ruth}_{^{33}S^{197}Au}(\theta_{\rm mon}) \cong \frac{R_{\rm mon}}{J}\frac{1}{\Omega_{\rm mon}}\,, \tag{47}$$

where $R_{\rm mon}$ is the number of nuclei of ^{33}S detected in the monitor detector per unit time per nucleus of ^{197}Au in the target. The differential cross section $\left(\frac{d\sigma}{d\Omega}\right)^{\rm Ruth}_{^{33}S^{197}Au}$ can be easily calculated in the center-of-mass frame by means of the well-known Rutherford formula

$$\left(\frac{d\sigma}{d\Omega}\right)^{\rm Ruth}_{^{33}S^{197}Au}(\theta_{\rm mon}) = \left(\frac{Z_{^1H}\, Z_{^{197}Au}\, e^2}{4E}\right)^2 \frac{1}{\sin^4(\theta_{\rm mon}/2)}\,, \tag{48}$$

with $Z_{^1H}$ and $Z_{^{197}Au}$ the atomic numbers of hydrogen and gold respectively, e the elementary charge, and E and $\theta_{\rm mon}$, in that order, the energy and the monitor detector angle expressed in the center-of-mass system.

In this way, J can be eliminated from Eqs. 2 by using Eq. 47, and the differential cross sections can be expressed as

$$\left(\frac{d\sigma}{d\Omega}\right)_{p^{33}S}(\theta) \cong \frac{R_{\rm det}}{R_{\rm mon}}\frac{\Omega_{\rm mon}}{\Omega_{\rm det}}\left(\frac{d\sigma}{d\Omega}\right)^{\rm Ruth}_{^{33}S^{197}Au}(\theta_{\rm mon})\,. \tag{49}$$

Using $R_{\rm det} = \dfrac{N_{\rm det}}{t\,\omega_{^1H}\,A}$ and $R_{\rm mon} = \dfrac{N_{\rm mon}}{t\,\omega_{^{197}Au}\,A}$, where $N_{\rm det}$ and $N_{\rm mon}$ are associated with the number of particles of interest (α-particles from the reaction $^{33}S(p,\alpha)^{30}P$ and ^{33}S from the reaction $^{197}Au(^{33}S,^{33}S)^{197}Au$, respectively) emit-

ted in the direction of the detectors (DSSD and monitor detector, respectively) in the time period t, A is the effective area of the target and $\omega_{^1\mathrm{H}}$ and $\omega_{^{197}\mathrm{Au}}$ are the surface density of atoms of ^{1}H and ^{197}Au in the target, respectively, and writing ω in terms of the target thickness δ (given in units of [mass]/[area]), the Avogadro's number N_{Av} and the molar mass M as $\omega = \delta\, N_{\mathrm{Av}}/M$, the differential cross section of the $^{33}\mathrm{S}(p,\alpha)^{30}\mathrm{P}$ reaction can be finally obtained as

$$\left(\frac{d\sigma}{d\Omega}\right)_{p^{33}\mathrm{S}}(\theta) \cong \frac{N_{\mathrm{det}}}{N_{\mathrm{mon}}}\frac{\Omega_{\mathrm{mon}}}{\Omega_{\mathrm{det}}}\frac{\delta_{^{197}\mathrm{Au}}}{\delta_{^1\mathrm{H}}}\frac{M_{^1\mathrm{H}}}{M_{^{197}\mathrm{Au}}}\left(\frac{d\sigma}{d\Omega}\right)^{\mathrm{Ruth}}_{^{33}\mathrm{S}^{197}\mathrm{Au}}(\theta_{\mathrm{mon}})\ . \qquad (50)$$

V.2. Detection efficiency

When a detection system involves the detection of two particles in coincidence by two different detectors, the effective solid angle covered by the system is smaller than the solid angles covered by each detector. For instance, in the specific case of the reaction $^{33}\mathrm{S}(p,\alpha)^{30}\mathrm{P}$, it is possible that when an α-particle is detected by the DSSD the partner ^{30}P is not detected by the PPAC because it does not travel in the direction of the spectrograph entrance window. Equivalently, it is possible that when a ^{30}P nucleus is detected by the PPAC the partner α-particle is not detected by the DSSD because it does not travel in the direction of this detector. If N_{det} is the number of events with α-particles from the reaction $^{33}\mathrm{S}(p,\alpha)^{30}\mathrm{P}$ emitted in the direction of a DSSD's strip (i.e., detected in singles) covering a solid angle Ω_{det}, and N_{coinc} is the number of events where an α-particles and a ^{30}P nucleus from the same reaction were detected simultaneously in the DSSD's strip and the PPAC, respectively, the detection efficiency ε can be defined by the relation

$$\varepsilon = \frac{N_{\mathrm{coinc}}}{N_{\mathrm{det}}}. \tag{51}$$

Because in this experiment the identification of the events of interest can be achieved only when the particles are measured in coincidence by the DSSD and the PPAC, N_{coinc} is the quantity which is accessible from the experiment and N_{det} can be calculated by means of Eq. 51 if ε is known. In this way, the differential cross section can be calculated as

$$\left(\frac{d\sigma}{d\Omega}\right)_{p^{33}\mathrm{S}}(\theta) \cong \frac{1}{\varepsilon}\frac{N_{\mathrm{coinc}}}{N_{\mathrm{mon}}}\frac{\Omega_{\mathrm{mon}}}{\Omega_{\mathrm{det}}}\frac{\delta_{^{197}\mathrm{Au}}}{\delta_{^{1}\mathrm{H}}}\frac{M_{^{1}\mathrm{H}}}{M_{^{197}\mathrm{Au}}}\left(\frac{d\sigma}{d\Omega}\right)^{\mathrm{Ruth}}_{^{33}\mathrm{S}^{197}\mathrm{Au}}(\theta_{\mathrm{mon}})\ . \tag{52}$$

In this expression, the product $\varepsilon\,\Omega_{\mathrm{det}}$ can be thought of as the effective solid angle of the detection system Ω_{sys} because it is associated with the angular range where a number N_{coinc} of pairs of particles from the same kind of reaction are detected in coincidence. Therefore, in terms of the effective solid angle Ω_{sys}, Eq. 52 can be rewritten as

$$\left(\frac{d\sigma}{d\Omega}\right)_{p^{33}\mathrm{S}}(\theta) \cong \frac{N_{\mathrm{coinc}}}{N_{\mathrm{mon}}}\frac{\Omega_{\mathrm{mon}}}{\Omega_{\mathrm{sys}}}\frac{\delta_{^{197}\mathrm{Au}}}{\delta_{^{1}\mathrm{H}}}\frac{M_{^{1}\mathrm{H}}}{M_{^{197}\mathrm{Au}}}\left(\frac{d\sigma}{d\Omega}\right)^{\mathrm{Ruth}}_{^{33}\mathrm{S}^{197}\mathrm{Au}}(\theta_{\mathrm{mon}})\ . \tag{53}$$

As will be seen in Sec. V.3, Ω_{sys} can be calculated from kinematical considerations, or equivalently the efficiency by means of

$$\varepsilon = \frac{\Omega_{\mathrm{sys}}}{\Omega_{\mathrm{det}}} \tag{54}$$

because Ω_{det} can be easily determined from geometrical considerations.

V.3. Efficiency calculations

The detection efficiency ε was calculated using the SUPERKIN code [98].

This code simulates the reaction $^{33}\mathrm{S}(p,\alpha)^{30}\mathrm{P}$ in the center of mass, with the exit-channel particles emitted in a random direction assuming a uniform probability distribution in solid angle, which is equivalent to a uniform probability distribution in azimuthal angle $\phi_{\mathrm{c.m.}}$ and a sine distribution in polar angle $\theta_{\mathrm{c.m.}}$. The emission angles of the α particle, $\phi_{\mathrm{c.m.}}$ and $\theta_{\mathrm{c.m.}}$, and those of the $^{30}\mathrm{P}$ nucleus, $\Phi_{\mathrm{c.m.}}$ and $\Theta_{\mathrm{c.m.}}$, satisfy (due to conservation laws) $\phi_{\mathrm{c.m.}} = \Phi_{\mathrm{c.m.}}$ and $\theta_{\mathrm{c.m.}} = \Theta_{\mathrm{c.m.}}$ (as in the center of mass particles are emitted back to back). Then, these angles in the center of mass system are converted to the laboratory system (using $\phi_{\mathrm{c.m.}} = \phi_{\mathrm{lab.}}$, and that $\theta_{\mathrm{c.m.}}$ and $\theta_{\mathrm{lab.}}$ are related by Eq. 8) and using their directions of emission it is checked whether the α particle and the $^{30}\mathrm{P}$ nucleus are detected in the DSSD and the SPS, respectively. A 'coincidence event' will be registered by the detection system only when both particles coming from the same reaction are detected by a different detector. Thus, when the simulation is performed for a large number of trials N_{total}, the effective solid angle Ω_{sys} subtended by the detection system in the center of mass can be calculated as

$$\Omega_{\mathrm{sys}} = 4\pi \, \frac{N_{\mathrm{success}}}{N_{\mathrm{total}}} \, , \tag{55}$$

where N_{success} is the number of 'coincedence events'. As stated in Sec. V.2, Ω_{sys} and the solid angle subtended by a DSSD's ring Ω_{det} are related by the expression

$$\Omega_{\mathrm{sys}} = \varepsilon \, \Omega_{\mathrm{det}} \, , \tag{56}$$

from which ε can be calculated if the values of $\Omega_{\rm det}$ expressed in the center of mass system are used.

TABLE III: Angular position θ, angular range $\theta_{\rm min}-\theta_{\rm max}$ and spanned solid angle $\Omega_{\rm det}$ of each DSSD ring, expressed in the laboratory system. The uncertainties in solid angles are about 5%.

Ring #	θ (deg)	$\theta_{\rm min}$ (deg)	$\theta_{\rm max}$ (deg)	$\Omega_{\rm det} = -2\pi[cos(\theta_{\rm min}) - cos(\theta_{\rm max})]$ (sr)
1	8.5	8.0	9.0	0.0022
2	9.6	9.1	10.1	0.0025
3	10.7	10.2	11.2	0.0028
4	11.8	11.3	12.3	0.0030
5	12.8	12.4	13.4	0.0033
6	13.9	13.5	14.4	0.0035
7	14.9	14.5	15.5	0.0037
8	16.0	15.6	16.5	0.0039
9	17.0	16.6	17.5	0.0041
10	18.0	17.6	18.5	0.0043
11	19.1	18.6	19.6	0.0045
12	20.1	19.7	20.5	0.0047
13	21.0	20.6	21.5	0.0048
14	22.0	21.6	22.5	0.0050
15	23.0	22.6	23.4	0.0051

The angular position θ, the angular range $\theta_{\rm min}$–$\theta_{\rm max}$ and the subtended solid angle $\Omega_{\rm det}$ of each ring of the DSSD used during the experiment (and therefore in the efficiency calculation) are indicated in Table III in the laboratory system. The solid angles $\Omega_{\rm det}$ expressed in the center-of-mass system, which are needed to calculate the efficiency by means of Eq. 56, were obtained by using Eq. 3 and are shown in Table IV for each of the five ^{33}S incident energies used in the experiment.

The other information needed for the calculation was the position, shape and size of the SPS's entrance window. It consisted of a 10.8 mm high and 13.6 mm wide rectangular window placed in the reaction plane, 267 mm from the center

TABLE IV: Solid angle $\Omega_{\rm det}$ spanned by each DSSD ring, expressed in the center-of-mass system for each of the five ^{33}S bombarding energies used in the experiment. The uncertainties in solid angles are about 5%.

	$\Omega_{\rm det}$ (sr)									
Rings	Low energy solution					High energy solution				
#	150.0 MeV	160.9 MeV	171.1 MeV	179.0 MeV	202.0 MeV	150.0 MeV	160.9 MeV	171.1 MeV	179.0 MeV	202.0 MeV
1	0.0065	0.0061	0.0058	0.0056	0.0051	0.029	0.028	0.028	0.027	0.026
2	0.0076	0.0071	0.0067	0.0065	0.0060	0.033	0.032	0.031	0.031	0.030
3	0.0088	0.0082	0.0078	0.0075	0.0069	0.037	0.036	0.035	0.034	0.033
4	0.010	0.0094	0.0089	0.0086	0.0078	0.041	0.039	0.038	0.038	0.036
5	0.012	0.011	0.010	0.0098	0.0090	0.044	0.043	0.042	0.041	0.040
6	0.013	0.012	0.012	0.011	0.010	0.048	0.047	0.046	0.045	0.043
7	0.015	0.014	0.013	0.013	0.012	0.053	0.051	0.049	0.048	0.046
8	0.018	0.017	0.015	0.015	0.013	0.057	0.055	0.053	0.052	0.050
9	0.021	0.019	0.018	0.017	0.015	0.062	0.059	0.058	0.056	0.054
10	0.025	0.023	0.021	0.020	0.018	0.068	0.065	0.062	0.061	0.058
11	0.031	0.028	0.025	0.024	0.021	0.075	0.071	0.068	0.066	0.062
12	0.040	0.035	0.031	0.029	0.025	0.085	0.079	0.075	0.073	0.067
13	0.056	0.046	0.040	0.037	0.031	0.10	0.092	0.086	0.082	0.075
14	0.11	0.072	0.058	0.052	0.040	0.16	0.12	0.10	0.097	0.085
15	0.088	0.15	0.13	0.092	0.059	0.098	0.18	0.18	0.14	0.10

of the scattering chamber, centered at $\theta_{\text{lab.}} = 2^\circ$ and subtending a solid angle of 0.0021 sr in the laboratory system.

As an example, efficiencies as a function of the center-of-mass angle obtained for three different ^{33}S bombarding energies are shown in Fig. 29. Because of the inverse kinematics each ring has two different solutions, which are indicated in the figure as low and high energy solutions. The vertical bars indicate the statistical uncertainty in the calculation of the efficiency, obtained as $\Delta\varepsilon = \varepsilon\sqrt{N_{success}}/N_{success}$, while the horizontal bars indicate the angular ranges in the center-of-mass system that each ring spanned during the experiment. As can be seen in the Fig. 29, the efficiency patterns are essentially the same for all the energies: $\varepsilon \sim 0$ at $\theta_{\text{c.m.}} \lesssim 30^\circ$ and $\varepsilon \sim 1$ at $30^\circ \lesssim \theta_{\text{c.m.}} \lesssim 150^\circ$, with a rapid transition from 0 to 1.

In the following section these efficiencies will be used for the determination of the differential cross sections as a function of the angle.

V.4. Cross section determination of the ^{33}S$(p,\alpha)^{30}$P reaction

V.4.1. Determination of measured energies

The cross section measurements were performed using ^{33}S ion beams incident on a CH_2Au target at five different bombarding energies: 150.0, 160.9, 171.1, 179.0 and 202.0 MeV.

The CH_2Au target was perpendicular to the beam direction and the thicknesses of the ^{197}Au and the CH_2 foils were 50 μg/cm^2 and 360 μg/cm^2, respectively. The energy losses ΔE of the ^{33}S beam particles in the target were

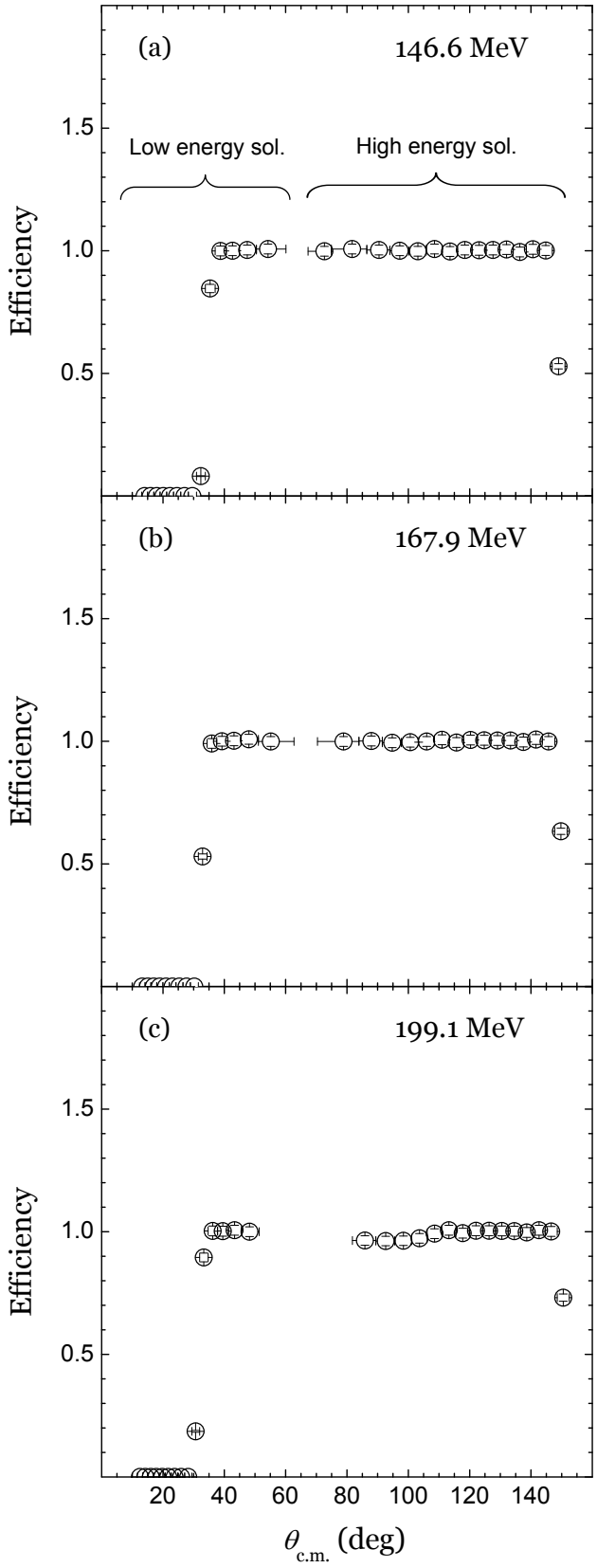

FIG. 29: Detection efficiency for the systems consisting of each DSSD ring together to the SPS entrance window at $E_{\mathrm{lab.}}(^{33}\mathrm{S}) = 146.6$, 167.6 and 199.1 MeV. Low and high energy solution are indicated. The vertical bars indicate the statistical uncertainty in the calculation of the efficiency, while the horizontal bars indicate the angular ranges in the center-of-mass system that each ring spanned during the experiment.

calculated performing Monte Carlo simulations. These simulations were carried out using the SRIM-2011 code [99]. The energy losses in the target were approximately $\Delta E \sim 6$ MeV, and the energy intervals over which differential cross sections were experimentally averaged are therefore (E_b, $E_b - \Delta E$), where E_b is the bombarding energy. The reported energy for each differential cross section corresponds to the center of the corresponding energy interval. Energy losses and integration intervals are presented in Table V at each of the five bombarding energies studied in this work.

TABLE V: ^{33}S bombarding energies, energy losses in the CH_2Au target and energy intervals over which experimental differential cross sections were integrated.

Bombarding energy (MeV)	Energy loss in the target (MeV)	Energy integration interval (MeV)
150.0	6.8	146.6 ± 3.4
160.9	6.5	157.6 ± 3.3
171.1	6.3	167.9 ± 3.2
179.0	6.2	175.9 ± 3.1
202.0	5.8	199.1 ± 2.9

V.4.2. Angular distributions of differential cross sections

The differential cross sections for the $^{33}S(p,\alpha)^{30}P$ reaction in the laboratory system were calculated using Eq. 52.

As mentioned above, the target was perpendicular to the beam and the thicknesses of the ^{197}Au and the CH_2 foils were $\delta_{^{197}Au} = (50 \pm 5)$ μg/cm^2 and $\delta_{CH_2} = (360 \pm 36)$ μg/cm^2, respectively. Hence, the CH_2 foil had an effective ^{1}H thickness of $\delta_{^1H} = (51 \pm 5)$ μg/cm^2. The molar masses $M_{^1H}$ = 1.00782503192(12) g/mol and $M_{^{197}Au}$ = 196.9665687(6) g/mol were calculated

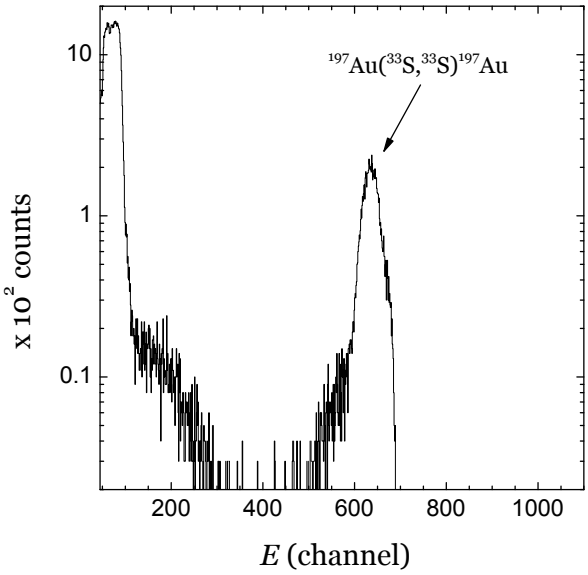

FIG. 30: Energy spectrum taken by the monitor detector at a ^{33}S bombarding energy of 171.1 MeV. The peak of elastic scattering of ^{33}S on ^{197}Au is indicated.

using atomic masses taken from Ref. [58]. A silicon surface barrier monitor detector was placed at $\theta_{\rm mon} = 41^\circ$ from the beam direction, with a solid angle $\Omega_{\rm mon} = (0.0055 \pm 0.0002)$ sr in the laboratory frame. The annular DSSD was 1000-μm thick and its active inner and outer radii were 10.7 mm and 33.2 mm, respectively. It was divided in 15 rings of 1.5 mm of length and 16 azimuthal sectors of 22.5° angular size. The angle θ, the angular range $\theta_{\rm min}$–$\theta_{\rm max}$ and the covered solid angle $\Omega_{\rm det}$ of each ring, expressed in the laboratory system, are indicated in Table III.

The number $N_{\rm mon}$ of elastically scattered ^{33}S particles on ^{197}Au was obtained from the monitor detector's energy spectra. In Fig. 30 the energy spectrum acquired by the monitor detector at a ^{33}S bombarding energy of 171.1 MeV is shown as an example. $N_{\rm mon}$ was taken from the integral of the elastic scattering peak, which is indicated in the figure. The angular distributions of the number of α-particles coming from the ^{33}S$(p,\alpha)^{30}$P reaction, $N_{\rm det}$, were taken from the

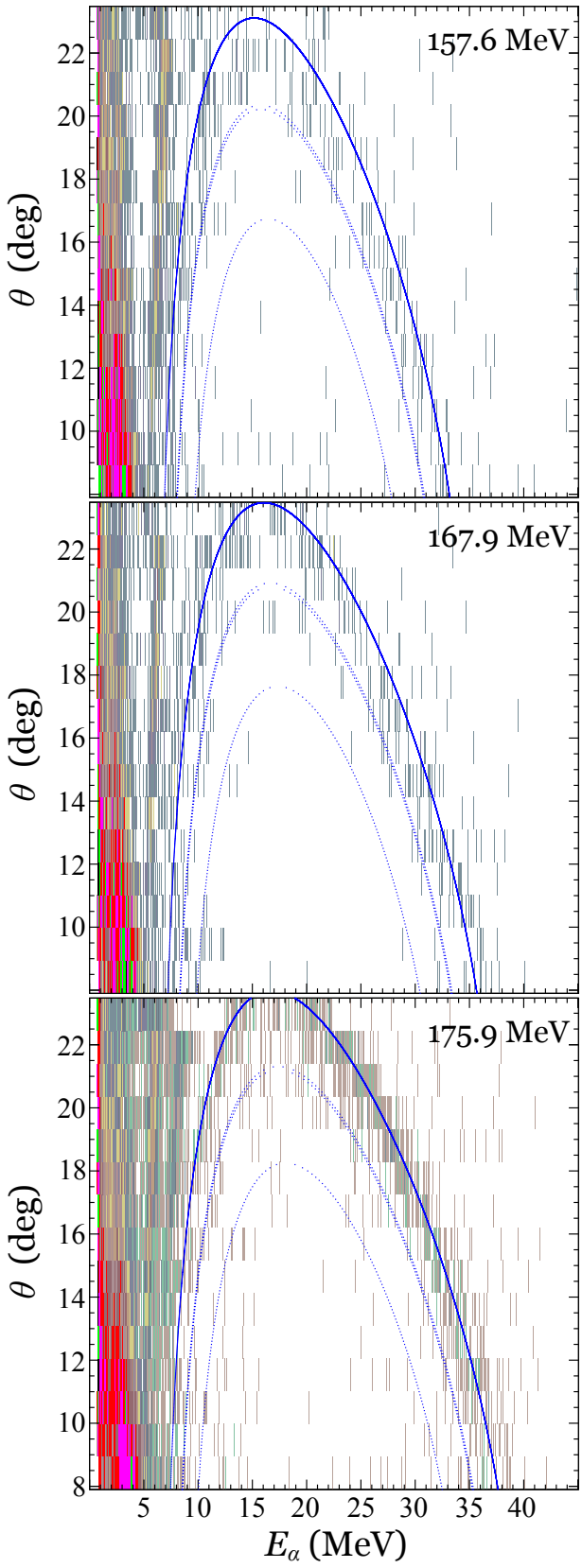

FIG. 31: Two-dimensional spectra of angle and energy of the particles detected at the DSSD, corresponding to events in coincidence (time gated) and within the ^{30}P island (ΔE_1-X gated). The laboratory energy of each spectrum is indicated. Experimental events are displayed as vertical segments. The θ binning represents the angular range covered by each DSSD's rings. The lines are calculations of the $^{33}\mathrm{S}(p,\alpha)^{30}\mathrm{P}$ kinematics with excitation energy corresponding to the ground state (solid line) and the first three excited states (dotted lines) of ^{30}P.

DSSD's E vs. θ spectra. In Fig. 31 the E vs. θ spectra acquired by the DSSD at three different ^{33}S bombarding energies are shown. $N_{\rm det}(\theta)$ was obtained by integrating the peak associated with the ground state of the $^{33}\mathrm{S}(p,\alpha)^{30}\mathrm{P}$ reaction. The solid lines are calculations of the $^{33}\mathrm{S}(p,\alpha)^{30}\mathrm{P}$ kinematics with excitation energy corresponding to the ground state, and indicate the location of the events of interest in the E vs. θ plane, while the dotted lines correspond to the location of events associated with the three first excited states of ^{30}P. The differential cross sections expressed in the laboratory system were transformed to the center-of-mass system by means of Eq. 6.

Measured angular distributions of the differential cross sections for the $^{33}\mathrm{S}(p,\alpha)^{30}\mathrm{P}$ reaction converted to the center-of-mass frame of reference are shown in Fig. 32 at each of the five laboratory energies studied in this work, i.e., 146.6, 157.6, 167.9, 175.9 and 199.1 MeV. From Eq. 7, these laboratory energies correspond to 4.35, 4.67, 4.98, 5.22 and 5.91 MeV in the center-of-mass system, respectively. The data shown in Fig. 32 are tabulated in Appendix A.

V.4.3. Uncertainties

The number $N_{\rm det}$ of events detected in each ring was very low, ranging from about 1 event per ring at 146.6 MeV up to about 50 events per ring at 199.1 MeV. For this reason, the statistical uncertainties due to fluctuations on $N_{\rm det}$ were estimated following the approach for small signals given by Feldman and Cousins in Ref. [100]. When the number of events $N_{\rm det}$ was lower than 20, the cross section confidence intervals with a confidence level (C.L.) of 68.3% (so-called 1σ intervals by analogy with Gaussian intervals) were taken from Tables VI

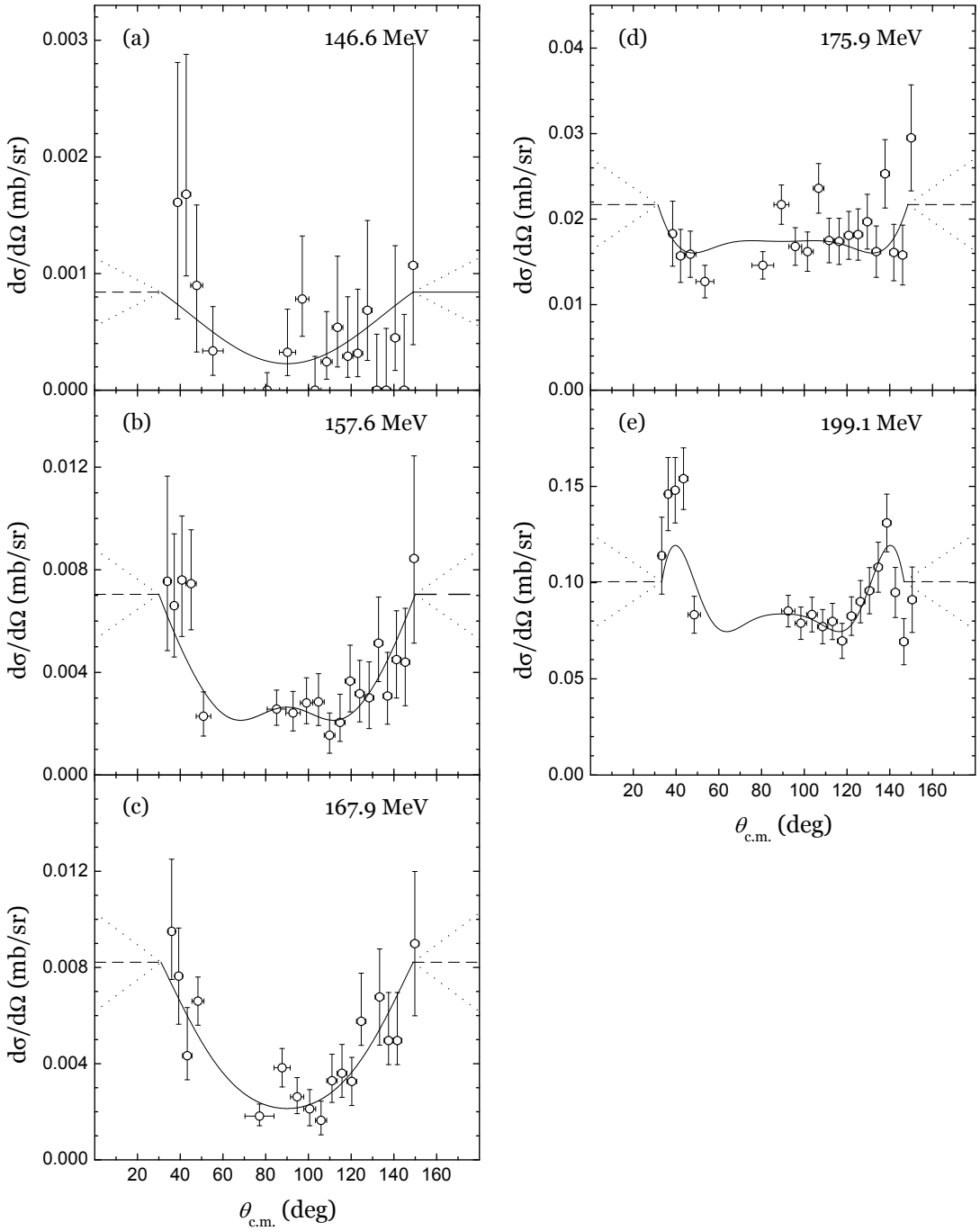

FIG. 32: Experimental angular distributions of differential cross section for the ^{33}S$(p,\alpha)^{30}$P reaction (open circles) and Legendre polynomial fits (solid lines). The dashed lines are linear extrapolations to the region without experimental data. The dotted lines were used to estimate contributions to the systematic uncertainties in the total cross sections due to the errors in the extrapolations. The vertical bars represent statistical 68.3% C.L. confidence intervals in the differential cross section, while the horizontal bars indicate the angular ranges where differential cross sections were experimentally averaged.

TABLE VI: 68.3% C.L. intervals for the Poisson signal mean μ, for total events observed n_0 , for known mean background b ranging from 0 to 5. Taken from Ref. [100]

$n_0 \backslash b$	0.0		0.5		1.0		1.5		2.0		2.5		3.0		3.5		4.0		5.0	
0	0.00	1.29	0.00	0.80	0.00	0.54	0.00	0.41	0.00	0.41	0.00	0.25	0.00	0.25	0.00	0.21	0.00	0.21	0.00	0.19
1	0.37	2.75	0.00	2.25	0.00	1.75	0.00	1.32	0.00	0.97	0.00	0.68	0.00	0.50	0.00	0.50	0.00	0.36	0.00	0.30
2	0.74	4.25	0.44	3.75	0.14	3.25	0.00	2.75	0.00	2.25	0.00	1.80	0.00	1.41	0.00	1.09	0.00	0.81	0.00	0.47
3	1.10	5.30	0.80	4.80	0.54	4.30	0.32	3.80	0.00	3.30	0.00	2.80	0.00	2.30	0.00	1.84	0.00	1.45	0.00	0.91
4	2.34	6.78	1.84	6.28	1.34	5.78	0.91	5.28	0.44	4.78	0.25	4.28	0.00	3.78	0.00	3.28	0.00	2.78	0.00	1.90
5	2.75	7.81	2.25	7.31	1.75	6.81	1.32	6.31	0.97	5.81	0.68	5.31	0.45	4.81	0.20	4.31	0.00	3.81	0.00	2.81
6	3.82	9.28	3.32	8.78	2.82	8.28	2.32	7.78	1.82	7.28	1.37	6.78	1.01	6.28	0.62	5.78	0.36	5.28	0.00	4.28
7	4.25	10.30	3.75	9.80	3.25	9.30	2.75	8.80	2.25	8.30	1.80	7.80	1.41	7.30	1.09	6.80	0.81	6.30	0.32	5.30
8	5.30	11.32	4.80	10.82	4.30	10.32	3.80	9.82	3.30	9.32	2.80	8.82	2.30	8.32	1.84	7.82	1.45	7.32	0.82	6.32
9	6.33	12.79	5.83	12.29	5.33	11.79	4.83	11.29	4.33	10.79	3.83	10.29	3.33	9.79	2.83	9.29	2.33	8.79	1.44	7.79
10	6.78	13.81	6.28	13.31	5.78	12.81	5.28	12.31	4.78	11.81	4.28	11.31	3.78	10.81	3.28	10.31	2.78	9.81	1.90	8.81
11	7.81	14.82	7.31	14.32	6.81	13.82	6.31	13.32	5.81	12.82	5.31	12.32	4.81	11.82	4.31	11.32	3.81	10.82	2.81	9.82
12	8.83	16.29	8.33	15.79	7.83	15.29	7.33	14.79	6.83	14.29	6.33	13.79	5.83	13.29	5.33	12.79	4.83	12.29	3.83	11.29
13	9.28	17.30	8.78	16.80	8.28	16.30	7.78	15.80	7.28	15.30	6.78	14.80	6.28	14.30	5.78	13.80	5.28	13.30	4.28	12.30
14	10.30	18.32	9.80	17.82	9.30	17.32	8.80	16.82	8.30	16.32	7.80	15.82	7.30	15.32	6.80	14.82	6.30	14.32	5.30	13.32
15	11.32	19.32	10.82	18.82	10.32	18.32	9.82	17.82	9.32	17.32	8.82	16.82	8.32	16.32	7.82	15.82	7.32	15.32	6.32	14.32
16	12.33	20.80	11.83	20.30	11.33	19.80	10.83	19.30	10.33	18.80	9.83	18.30	9.33	17.80	8.83	17.30	8.33	16.80	7.33	15.80
17	12.79	21.81	12.29	21.31	11.79	20.81	11.29	20.31	10.79	19.81	10.29	19.31	9.79	18.81	9.29	18.31	8.79	17.81	7.79	16.81
18	13.81	22.82	13.31	22.32	12.81	21.82	12.31	21.32	11.81	20.82	11.31	20.32	10.81	19.82	10.31	19.32	9.81	18.82	8.81	17.82
19	14.82	23.82	14.32	23.32	13.82	22.82	13.32	22.32	12.82	21.82	12.32	21.32	11.82	20.82	11.32	20.32	10.82	19.82	9.82	18.82
20	15.83	25.30	15.33	24.80	14.83	24.30	14.33	23.80	13.83	23.30	13.33	22.80	12.83	22.30	12.33	21.80	11.83	21.30	10.83	20.30

TABLE VII: 68.3% C.L. intervals for the Poisson signal mean μ, for total events observed n_0 , for known mean background b ranging from 6 to 15. Taken from Ref. [100]

$n_0\backslash b$	6.0		7.0		8.0		9.0		10.0		11.0		12.0		13.0		14.0		15.0	
0	0.00	0.18	0.00	0.17	0.00	0.17	0.00	0.17	0.00	0.16	0.00	0.16	0.00	0.16	0.00	0.16	0.00	0.16	0.00	0.15
1	0.00	0.24	0.00	0.21	0.00	0.20	0.00	0.19	0.00	0.18	0.00	0.17	0.00	0.17	0.00	0.17	0.00	0.17	0.00	0.16
2	0.00	0.31	0.00	0.27	0.00	0.23	0.00	0.21	0.00	0.20	0.00	0.19	0.00	0.19	0.00	0.18	0.00	0.18	0.00	0.18
3	0.00	0.69	0.00	0.42	0.00	0.31	0.00	0.26	0.00	0.23	0.00	0.22	0.00	0.21	0.00	0.20	0.00	0.20	0.00	0.19
4	0.00	1.22	0.00	0.69	0.00	0.60	0.00	0.38	0.00	0.30	0.00	0.26	0.00	0.24	0.00	0.23	0.00	0.22	0.00	0.21
5	0.00	1.92	0.00	1.23	0.00	0.99	0.00	0.60	0.00	0.48	0.00	0.35	0.00	0.29	0.00	0.26	0.00	0.24	0.00	0.23
6	0.00	3.28	0.00	2.38	0.00	1.65	0.00	1.06	0.00	0.63	0.00	0.53	0.00	0.42	0.00	0.33	0.00	0.29	0.00	0.26
7	0.00	4.30	0.00	3.30	0.00	2.40	0.00	1.66	0.00	1.07	0.00	0.88	0.00	0.53	0.00	0.47	0.00	0.38	0.00	0.32
8	0.31	5.32	0.00	4.32	0.00	3.32	0.00	2.41	0.00	1.67	0.00	1.46	0.00	0.94	0.00	0.62	0.00	0.48	0.00	0.43
9	0.69	6.79	0.27	5.79	0.00	4.79	0.00	3.79	0.00	2.87	0.00	2.10	0.00	1.46	0.00	0.94	0.00	0.78	0.00	0.50
10	1.22	7.81	0.69	6.81	0.23	5.81	0.00	4.81	0.00	3.81	0.00	2.89	0.00	2.11	0.00	1.47	0.00	1.03	0.00	0.84
11	1.92	8.82	1.23	7.82	0.60	6.82	0.19	5.82	0.00	4.82	0.00	3.82	0.00	2.90	0.00	2.12	0.00	1.54	0.00	1.31
12	2.83	10.29	1.94	9.29	1.12	8.29	0.60	7.29	0.12	6.29	0.00	5.29	0.00	4.29	0.00	3.36	0.00	2.57	0.00	1.89
13	3.28	11.30	2.38	10.30	1.65	9.30	1.06	8.30	0.60	7.30	0.05	6.30	0.00	5.30	0.00	4.30	0.00	3.37	0.00	2.57
14	4.30	12.32	3.30	11.32	2.40	10.32	1.66	9.32	1.07	8.32	0.53	7.32	0.00	6.32	0.00	5.32	0.00	4.32	0.00	3.38
15	5.32	13.32	4.32	12.32	3.32	11.32	2.41	10.32	1.67	9.32	1.00	8.32	0.53	7.32	0.00	6.32	0.00	5.32	0.00	4.32
16	6.33	14.80	5.33	13.80	4.33	12.80	3.33	11.80	2.43	10.80	1.46	9.80	0.94	8.80	0.47	7.80	0.00	6.80	0.00	5.80
17	6.79	15.81	5.79	14.81	4.79	13.81	3.79	12.81	2.87	11.81	2.10	10.81	1.46	9.81	0.94	8.81	0.48	7.81	0.00	6.81
18	7.81	16.82	6.81	15.82	5.81	14.82	4.81	13.82	3.81	12.82	2.89	11.82	2.11	10.82	1.47	9.82	0.93	8.82	0.43	7.82
19	8.82	17.82	7.82	16.82	6.82	15.82	5.82	14.82	4.82	13.82	3.82	12.82	2.90	11.82	2.12	10.82	1.48	9.82	0.84	8.82
20	9.83	19.30	8.83	18.30	7.83	17.30	6.83	16.30	5.83	15.30	4.83	14.30	3.83	13.30	2.91	12.30	2.12	11.30	1.31	10.30

and VII. These tables, obtained by Feldman and Cousins [100] using Bayesian statistics of Poisson processes with background, provide non-symmetrical lower and upper limits for different background contributions. Otherwise, for $N_{\mathrm{det}} > 20$, confidence intervals were calculated by means of the classical approach using the well-known $N_{\mathrm{det}} \pm \sqrt{N_{\mathrm{det}}}$ for Poisson processes, which is also associated with a C.L. of 68.3%. For a small N_{det} the classical approach underestimates both the lower and upper limits of the confidence intervals (i.e., the length of the lower confidence interval is overestimated while the length of the upper confidence interval is underestimated). But the classical approach tends towards the Bayesian as N_{det} gets larger, the difference being almost negligible for $N_{\mathrm{det}} > 20$.

The statistical uncertainties of N_{mon} are also calculated by means of $\pm\sqrt{N_{\mathrm{mon}}}$ ($N_{\mathrm{mon}} \sim 1000$) and its contribution to the final statistical uncertainty of the differential cross section is almost negligible in comparison with the contribution of N_{mon}.

The vertical bars in Fig. 32 represent statistical confidence intervals for the differential cross sections with a C.L. of 68.3%. They typically range from 10% at 199.1 MeV up to 175% at 146.6 MeV. The horizontal bars indicate the angular ranges in the center-of-mass system covered by each ring during the experiment, i.e., the intervals over which the differential cross sections were experimentally averaged. Tabulated values of the 68.3% C.L. confidence limits for the differential cross section and the angular integration limits are given in Appendix A.

The dominant contributions to the systematic uncertainty of the differential cross section come from the effective thickness of the ^{1}H target ($\Delta\delta_{^{1}\mathrm{H}}/\delta_{^{1}\mathrm{H}} = 0.10$), the thickness of the ^{197}Au backing foil ($\Delta\delta_{^{197}\mathrm{Au}}/\delta_{^{197}\mathrm{Au}} = 0.10$), the solid angle of the monitor detector ($\Delta\Omega_{\mathrm{mon}}/\Omega_{\mathrm{mon}} = 0.035$) and the solid angles of the

rings of the DSSD ($\Delta\Omega_{\rm det}/\Omega_{\rm det} = 0.05$). An overall systematic uncertainty of 15% is obtained by adding these contributions in quadrature.

V.4.4. Fitting the differential cross sections

In order to calculate total cross sections at each energy by integrating the differential cross sections, multipole expansions of the angular distributions have been performed.

In scattering theory the differential cross sections are typically expanded in terms of orthogonal Legendre polynomials [60, 101–105],

$$\frac{d\sigma}{d\Omega}(\theta) = \sum_{i=0} a_i P_i(\cos\theta) \ , \tag{57}$$

because the expansion coefficients a_i are linear combinations of bilinear products of the appropriate partial wave amplitudes [101], i.e.,

$$a_i = \sum_{jk} C_i(j,k)\eta_j\eta_k^* \ . \tag{58}$$

Because at these low energies the reaction is dominated by compound-nucleus formation [60, 106, 107] the angular distributions measured in this work are symmetric about $\theta = 90°$, and therefore only the even-order Legendre polynomials were used in the expansion. The expansion coefficients a_j and their covariance matrix were determined by the least squares method. For each set of differential cross-sections a number of fits were carried out, each with the expansion series truncated at a different order of Legendre polynomial (second, fourth, sixth, and eighth order truncations were examined). The results of the fits are

shown in Fig. 32 and tabulated in Table VIII. The polynomial expansions were restricted to the angular range $\theta_1 \lesssim \theta_{\text{c.m.}} \lesssim \theta_2$ where experimental data were obtained ($\theta_1 \sim 30^\circ$ and $\theta_2 \sim 150^\circ$). The condition $\theta_2 = 180^\circ - \theta_1$ was imposed for the purpose of satisfying the symmetry about $\theta = 90^\circ$. The dashed linear segments shown in Fig. 32 are extrapolations of the differential cross section towards forward and backward angles and were used, together with the Legendre polynomial fits, to obtain the total cross sections from integration.

TABLE VIII: Least-squares Legendre polynomial expansion coefficients of the differential cross section for the $^{33}\text{S}(p,\alpha)^{30}\text{P}$ reaction at different laboratory energies.

	Energy				
Coeff.	146.6 MeV	157.6 MeV	167.9 MeV	175.9 MeV	199.1 MeV
a_0	0.000506	0.00392	0.00468	0.0195	0.0625
a_2	0.000557	0.00500	0.00591	0.0100	-0.0964
a_4	–	0.00285	0.00110	0.0127	-0.161
a_6	–	-0.000164	–	0.00722	-0.152
a_8	–	0.000391	–	0.00123	-0.0511

V.4.5. Total cross sections and the excitation function

The total cross section σ is related to the differential cross section by

$$\sigma = \int_{4\pi} \frac{d\sigma}{d\Omega}(\theta)\, d\Omega\,. \tag{59}$$

Since the differential solid angle is $d\Omega = \sin(\theta) d\phi d\theta$ and $\dfrac{d\sigma}{d\Omega}$ is independent of ϕ,

$$\sigma = \int_0^{\pi} \frac{d\sigma}{d\Omega}(\theta)\sin(\theta)d\theta \int_0^{2\pi} d\phi = 2\pi \int_0^{\pi} \frac{d\sigma}{d\Omega}(\theta)\sin(\theta)d\theta\,. \tag{60}$$

Total cross sections were calculated by the integration of the Legendre polynomial expansions obtained from the fits and their extrapolations, i.e.,

$$\sigma = 2\pi \left(\int_0^{\theta_1} f(\theta)\sin(\theta)\,d\theta + \int_{\theta_1}^{\theta_2} \left(\sum_i a_i P_i(\cos\theta) \right) \sin(\theta)\,d\theta + \int_{\theta_2}^{\pi} g(\theta)\sin(\theta)\,d\theta \right), \tag{61}$$

where P_i is the Legendre polynomial of order i, and $f(\theta)$ and $g(\theta)$ are the linear extrapolations which have been set as constant. If $f(\theta) = A$ and $g(\theta) = B$, using the substitution $x = \cos(\theta)$, the integrals in Eq. 61 become

$$\sigma = 2\pi \left(\int_{x_1}^{1} A\,dx + \sum_i a_i \int_{x_2}^{x_1} P_i(x)\,dx + \int_{-1}^{x_2} B\,dx \right), \tag{62}$$

which can be easily integrated analytically.

The uncertainty in the integration has two contributions. One of them comes from the statistical uncertainty in the Legendre polynomial fit over the angular range $\theta_1 \leq \theta \leq \theta_2$. This contribution, $\Delta\sigma_{\text{stat.}}$, was obtained by means of the law of propagation of errors [108]

$$(\Delta\sigma_{\text{stat.}})^2 = \sum_{i,j} \frac{\partial\sigma}{\partial a_i}\frac{\partial\sigma}{\partial a_j}\,\text{cov}(a_i, a_j)\,, \tag{63}$$

where cov(a_i,a_j) is an element of the covariance matrix, i.e., the covariance of a_i and a_j when $i \neq j$ and the variance of a_i when $i = j$. Using Eq. 62, this statistical uncertainty can be calculated as

$$(\Delta\sigma_{\text{stat.}})^2 = (2\pi)^2 \sum_{i,j} \int_{x_2}^{x_1} P_i(x)\,dx \int_{x_2}^{x_1} P_j(x)\,dx \;\; \text{cov}(a_i, a_j)\,. \tag{64}$$

The relative statistical uncertainty, $\frac{\Delta\sigma_{\text{stat.}}}{\sigma}$, varies from about 2% at the highest measured energy to about 20% at the lowest measured energy.

The other contribution comes from the systematic uncertainty in the linear extrapolations used at backward and forward angles. This contribution, $\Delta\sigma_{\text{sys.}}^{\text{extrap.}}$, was estimated by integrating the non-constant linear extrapolations shown in Fig. 32 as dotted lines, which keep the symmetry about $\theta = 90°$.

The contribution to the total cross sections of $\frac{d\sigma}{d\Omega}$ integrated over the angular intervals where the constant linear extrapolations were done, $0° \leq \theta \leq \theta_1$ and $\theta_2 \leq \theta \leq 180°$, are always lower than 25%. This is due to the fact that in the integrals of Eq. 61 the differential cross section is weighted by the Jacobian $\sin(\theta)$ and, therefore, the integrands become smaller as the angle approaches 0° and 180°. For the same reason, the relative systematic uncertainty due to the linear extrapolations $\frac{\Delta\sigma_{\text{sys.}}^{\text{extrap.}}}{\sigma}$, which ranges from 1% up to 3% for the highest and lowest measured energies respectively, is always smaller than the relative statistical uncertainty $\frac{\Delta\sigma_{\text{stat.}}}{\sigma}$ from the Legendre polynomial fits, and much smaller than the 15% of relative systematic uncertainty $\frac{\Delta\sigma_{\text{sys.}}^{\text{norm.}}}{\sigma}$ from normalization.

The total cross sections obtained for the g.s. to g.s. transition of the $^{33}\text{S}(p,\alpha)^{30}\text{P}$ reaction are given in Table IX. Statistical and systematic uncertainties are tabulated separately, the latter one obtained by adding in quadrature the contributions $\Delta\sigma_{\text{sys.}}^{\text{extrap.}}$ and $\Delta\sigma_{\text{sys.}}^{\text{norm.}}$. The experimental excitation function for this reaction is plotted in Fig. 33. The vertical bars represent the overall uncertainty calculated by adding the statistical and systematic contributions in

TABLE IX: Cross sections of the ^{33}S(p,α)^{30}P and its reverse ^{30}P(α,p)^{33}S reactions in the center-of-mass system, at the five energies studied in this work. The first three columns contain energies and cross sections for the ^{33}S(p,α)^{30}P reaction, the fourth column contains the conversion factors from the ^{33}S(p,α)^{30}P to the ^{30}P(α,p)^{33}S cross sections, and the last two columns contain energies and cross sections for the ^{30}P(α,p)^{33}S reaction. The energy intervals represent where the cross sections have been experimentally averaged due to energy loss in the target.

^{33}S(p,α)^{30}P			C. Factor	^{30}P(α,p)^{33}S	
$E_{\mathrm{lab.}}$ (MeV)	$E_{\mathrm{c.m.}}$ (MeV)	$\sigma_{p^{33}\mathrm{S}}$ (mb)	$\sigma_{\alpha^{30}\mathrm{P}}/\sigma_{p^{33}\mathrm{S}}$	$E_{\mathrm{c.m.}}$ (MeV)	$\sigma_{\alpha^{30}\mathrm{P}}$ (mb)
146.6 ± 3.4	4.35 ± 0.10	0.0061 ± 0.0012(stat.) ± 0.0009(sys.)	1.136	2.83 ± 0.10	0.0069 ± 0.0013(stat.) ± 0.0011(sys.)
157.6 ± 3.3	4.67 ± 0.10	0.0447 ± 0.0031(stat.) ± 0.0068(sys.)	1.095	3.15 ± 0.10	0.0489 ± 0.0033(stat.) ± 0.0074(sys.)
167.9 ± 3.2	4.98 ± 0.09	0.0650 ± 0.0028(stat.) ± 0.0098(sys.)	1.064	3.46 ± 0.09	0.069 ± 0.003(stat.) ± 0.010(sys.)
175.9 ± 3.1	5.22 ± 0.09	0.2213 ± 0.0069(stat.) ± 0.033(sys.)	1.043	3.70 ± 0.09	0.231 ± 0.007(stat.) ± 0.035(sys.)
199.1 ± 2.9	5.91 ± 0.09	1.11 ± 0.03(stat.) ± 0.17(sys.)	0.995	4.38 ± 0.09	1.10 ± 0.03(stat.) ± 0.17(sys.)

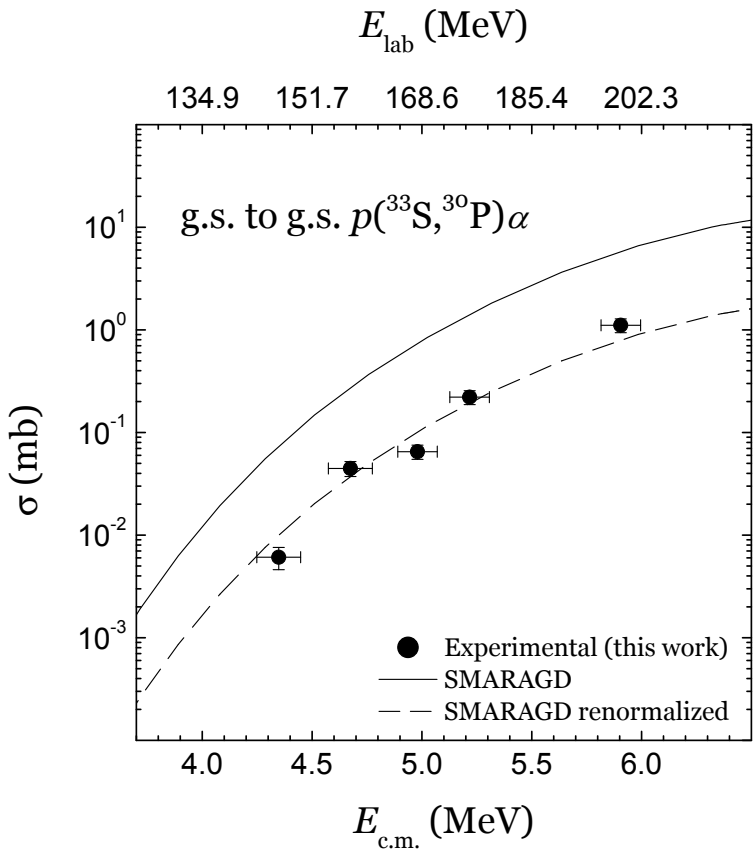

FIG. 33: Experimental $p(^{33}\mathrm{S},^{30}\mathrm{P})\alpha$ cross sections obtained in this work (full circles) and predicted SMARAGD cross sections (solid line) as a function of the energy. The vertical bars indicate overall uncertainties. The horizontal bars indicate the energy intervals where the cross sections were experimentally averaged due to energy loss in the target. The measured cross sections fluctuate around the SMARAGD cross section which was renormalized by a factor of 0.137 (dashed line).

quadrature. The horizontal bars indicate the energy intervals where the cross sections were experimentally averaged due to the energy loss in the target. The cross sections measured in this experiment are compared with the theoretical prediction of the SMARAGD code calculations [109–111]. As can be seen from Fig. 33, the theoretical prediction (solid line) overestimates the experimentally determined result (circles) by approximately a factor of 7–8. The dashed line represents the SMARAGD cross sections renormalized by a factor $\beta = 0.137$. This

factor was calculated by the method of weighted least squares, minimizing the statistic

$$\chi^2 = \sum_i \frac{\left(\sigma_i - \beta\,\sigma^{\mathrm{th}}\left(E_i\right)\right)^2}{\left(\Delta\sigma_i\right)^2} \tag{65}$$

where $\sigma^{\mathrm{th}}(E)$ is the theoretical excitation function, and σ_i and $\Delta\sigma_i$ are, respectively, the experimental cross section and its statistical uncertainty at the energy E_i. Although the experimental cross sections and the theoretical excitation function differ by a factor of 0.137, they both exhibit the same energy dependence as can be noted from the comparison between the experimental and the renormalized theoretical excitation functions.

As seen in Fig. 31, the contributions to the $^{33}\mathrm{S}(p,\alpha)^{30}\mathrm{P}^*$ cross section from transfer to excited states in ^{30}P were experimentally found to be small. Indeed, SMARAGD calculations of the $^{33}\mathrm{S}(p,\alpha)^{30}\mathrm{P}$ cross section show that the reaction is dominated by transitions to the ground state in ^{30}P at the energy range studied in this work [112].

V.5. Cross section determination of the $^{30}\mathrm{P}(\alpha,p)^{33}\mathrm{S}$ reaction

The conversion factors $\sigma_{\alpha^{30}\mathrm{P}}/\sigma_{p^{33}\mathrm{S}}$ were obtained using the reciprocity theorem (see Eq. 10) spin values $J_p = 1/2$, $J_{^{33}\mathrm{S}} = 3/2$, $J_\alpha = 0$ and $J_{^{30}\mathrm{P}} = 1$ (extracted from Ref. [113]), masses $m_p = 1.00782503192(12)$ amu, $m_{^{33}\mathrm{S}} = 32.97145876(15)$ amu, $m_\alpha = 4.00260325410(6)$ amu and $m_{^{30}\mathrm{P}} = 29.9783138(3)$ amu (extracted from Ref. [58]), and the Q-value $Q_{[^{33}\mathrm{S}(p,\alpha)^{30}\mathrm{P}]} = -1.52136(34)$ MeV (extracted from Ref. [114]). These conversion factors are shown in Fig. 34 as a function of $E_{p^{33}\mathrm{S}}$, from where it can be seen that they are typically around 1.0–1.2 in the

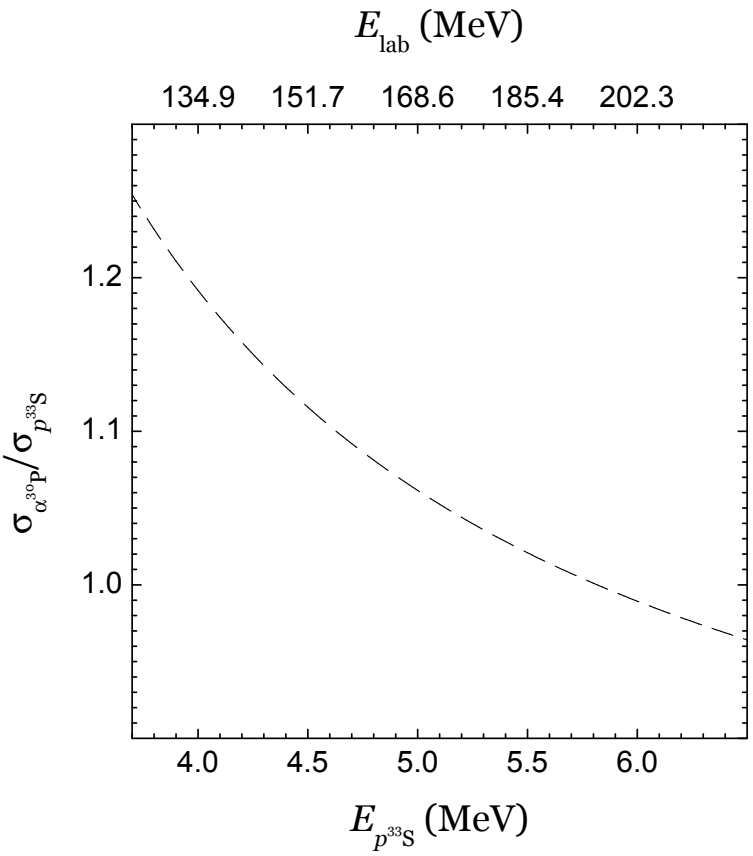

FIG. 34: Conversion factors from ^{33}S$(p,\alpha)^{30}$P to ^{30}P$(\alpha,p)^{33}$S cross sections as a function of the center-of-mass $E_{p^{33}\mathrm{S}}$ and the ^{33}S bombarding energy (top scale).

energy region studied in this work.

The ^{30}P$(\alpha,p)^{33}$S cross sections for the g.s. to g.s. transition obtained from the experimental ^{33}S$(p,\alpha)^{30}$P cross sections are tabulated in Table IX. The excitation function is plotted in Fig. 35 and compared with the theoretical prediction of the SMARAGD code calculations. This theoretical excitation function is tabulated in Appendix B. In Fig. 35, as well as for the case of the ^{33}S$(p,\alpha)^{30}$P cross sections, the vertical bars represent the overall uncertainty calculated by adding the statistical and systematic contributions in quadrature, while the horizontal bars indicate the energy intervals where the cross sections were experimentally averaged due to energy loss in the target. As can be seen from Fig. 35, the the-

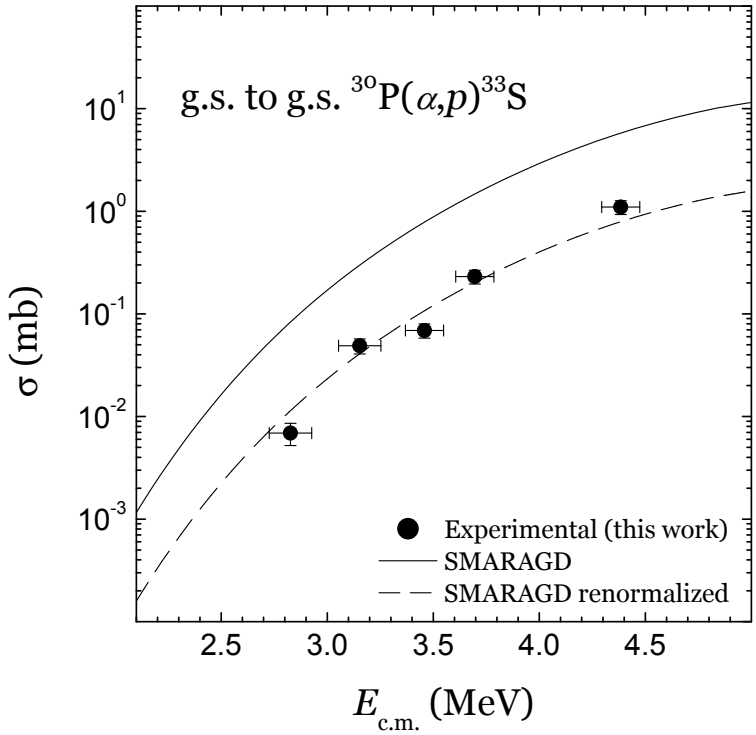

FIG. 35: ^{30}P(α,p)^{33}S cross sections (circles) obtained in this work from experimental ^{33}S(p,α)^{30}P cross sections, and predicted SMARAGD cross sections (solid line) as a function of the energy. The vertical bars indicate overall uncertainties. The horizontal bars indicate the energy intervals where the cross sections were experimentally averaged due to energy loss in the target. The measured cross section fluctuates around a SMARAGD cross section renormalized by a factor of 0.137 (dashed line).

oretical cross sections for the ^{30}P(α,p)^{33}S reaction predicted by SMARAGD (solid line) overestimate the experimentally determined result (circles) by approximately a factor of 7–8. The dashed line represents the SMARAGD cross sections renormalized by a factor of 0.137. As for the case of the ^{33}S(p,α)^{30}P reaction, the experimental cross sections fluctuate around the renormalized theoretical ones showing a similar pattern as a function of the energy. This renormalized theoretical excitation function will be used in Sec. VI as the extrapolation to lower energies that is needed to obtain the ^{30}P(α,p)^{33}S reaction rate.

VI. REACTION RATE DETERMINATION

VI.1. ^{30}P(α,p)^{33}S reaction rate

VI.1.1. Ground-state-to-ground-state reaction rate

As mentioned previously, at energies of astrophysical interest (i.e., in the energy range of the Gamow window at a given temperature) the cross sections are very small. Therefore, their measurements require very time consuming experiments that in most of the cases are impractical to carry out. Instead, cross sections are usually measured at higher energies and extrapolated to lower energies in order to calculate the stellar reaction rate. In X-ray bursts, the astrophysical scenario of interest to this work, the relevant temperature range is $0.5 \lesssim T_9 \lesssim 2$. For the ^{30}P($\alpha$,$p$)^{33}S reaction, these temperatures correspond to the energy range 0.9 MeV $\lesssim E \lesssim$ 3.7 MeV, which is only in a partial overlap with the energy range of 2.9 MeV $\lesssim E \lesssim$ 4.2 MeV covered in this work. For this reason, the theoretical SMARAGD excitation function renormalized by a factor of 0.137 which fits the experimental cross sections, as shown in Sec. V.5, was used for the extrapolation to lower energies.

The astrophysical S-factor for the g.s. to g.s. ^{30}P(α,p)^{33}S reaction obtained by means of Eq. 31 from the experimental and the renormalized theoretical cross sections is shown in Fig. 36 by the dashed line. The dotted lines represent

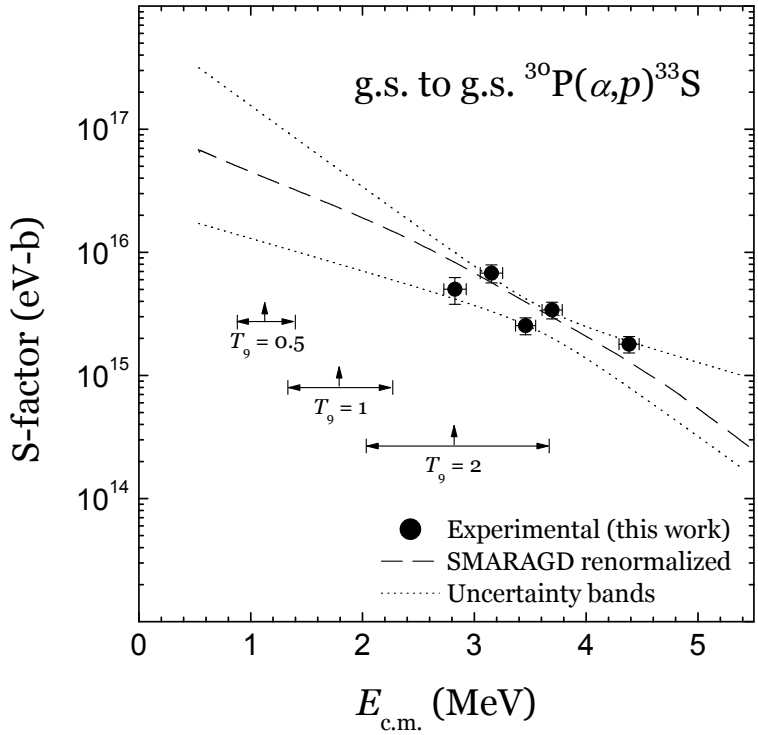

FIG. 36: Energy dependence of the astrophysical S-factor for the g.s. to g.s. ^{30}P(α,p)^{33}S reaction obtained from the experimental (circles) and the renormalized theoretical (dashed line) cross sections. The dotted lines represent 68.3% C.L. confidence limits for the extrapolations to the experimental result. Vertical and horizontal arrows correspond, respectively, to the most effective energies for thermonuclear reactions of the ^{30}P(α,p)^{33}S type and the Gamow windows over which most of the reactions occur at the indicated T_9 X-ray burst temperatures.

68.3% C.L. confidence limits for the extrapolations to the experimental result. It can be seen, as explained in Sec. III.5, that the S-factor varies much less rapidly with energy than the cross section shown in Fig. 35. Astrophysically interesting energy regions for different X-ray bursts temperatures T_9 are also shown in Fig. 36. The vertical arrows correspond to the most effective energies for thermonuclear reactions at those temperatures, while the horizontal arrows represent the Gamow windows over which most of the reactions occur.

The g.s. to g.s. ^{30}P(α,p)^{33}S reaction rate per particle pair $\langle\sigma^0 v\rangle$ as a function

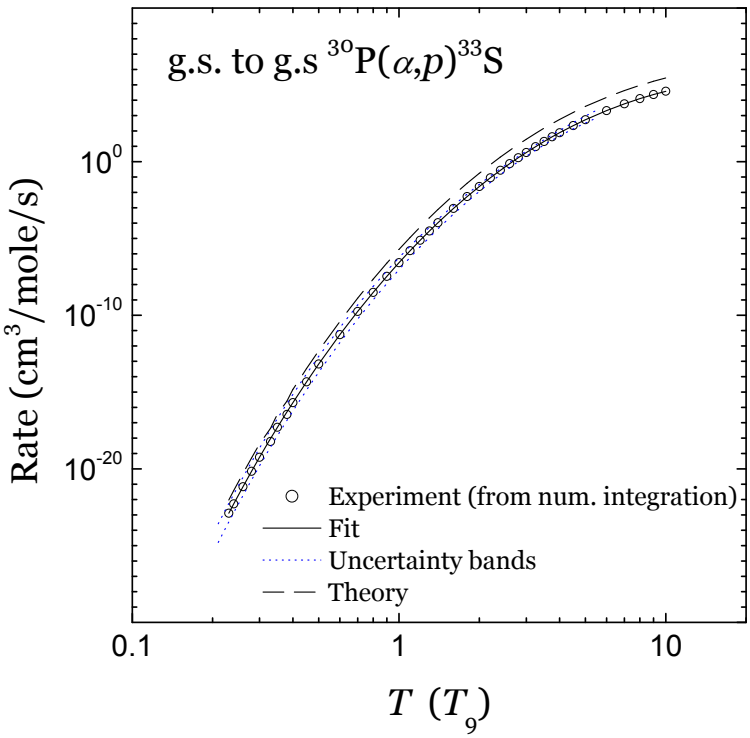

FIG. 37: Temperature dependence of the g.s. to g.s. ^{30}P(α,p)^{33}S reaction rate $\langle\sigma^0 v\rangle$ obtained by numerically integrating the theoretical renormalized S-factor used as extrapolation to lower energies. The numerically integrated results (circles), 68.3% C.L. confidence limits (dotted lines), the theoretical SMARAGD prediction (dashed line) and a fit using the parameterization of Eq. X (solid line) are shown. The temperature range where the calculations were performed includes the X-ray burst temperatures of interest.

of temperature was obtained from Eq. 32 by numerical integration of the renormalized SMARAGD S-factor shown by the dashed line in Fig. 36. The calculation of $\langle\sigma^0 v\rangle$ was carried out by means of the INFRASTRUCTURE code [115, 116], which performs numerical integration using the Riemann sum and trapezoidal rule. The energy range 0.5 MeV $\lesssim E \lesssim$ 12 MeV over which the S-factor was given as input made it possible to perform the integration in the temperature range $0.2 \lesssim T_9 \lesssim 10$ (the Gamow window at $T_9 = 0.2$ covers the energy range 0.5 MeV $\lesssim E \lesssim$ 0.7 MeV), which includes the temperatures of interest for X-ray

bursts. The obtained reaction rate per particle pair, given as usual by $N_{\rm Av}\,\langle\sigma^0 v\rangle$ in units of $\mathrm{cm}^3\,\mathrm{mole}^{-1}\,\mathrm{s}^{-1}$, is plotted against T in Fig. 37 by the open circles. The dotted lines are 68.3% C.L. confidence limits and the dashed line is the theoretical SMARAGD prediction.

The reaction rate per particle pair $N_{\rm Av}\,\langle\sigma^0 v\rangle$ obtained in this work varies from $6\times10^{-14}\,\mathrm{cm}^3\,\mathrm{mole}^{-1}\,\mathrm{s}^{-1}$ to $2\times10^{-6}\,\mathrm{cm}^3\,\mathrm{mole}^{-1}\,\mathrm{s}^{-1}$ in the most important temperature range for X-ray bursts, $0.5 \leq T_9 \leq 2$. As well as for the g.s. to g.s. $^{30}\mathrm{P}(\alpha,\,p)^{33}\mathrm{S}$ cross section, the theoretical SMARAGD prediction overestimates the obtained reaction rate by approximately a factor of 7–8, due to the fact that the cross section and the reaction rate are related by the linear relation of Eq. 27.

TABLE X: Parameters of the fit to the g.s. to g.s. $^{30}\mathrm{P}(\alpha,p)^{33}\mathrm{S}$ reaction rate $\langle\sigma^0 v\rangle$ shown in Fig. 37, which was performed using as fitting function the parameterization given in Eq. 66.

a_0	0.553120 $\times10^{2}$
a_1	-0.132569 $\times10^{1}$
a_2	-0.189871 $\times10^{2}$
a_3	-0.516285 $\times10^{2}$
a_4	0.149475 $\times10^{1}$
a_5	-0.487502 $\times10^{-1}$
a_6	0.272247 $\times10^{2}$

A fit to the numerically calculated reaction rate as a function of temperature was performed using the phenomenological parameterization from Refs. [59, 117],

$$N_{\rm Av}\left\langle\sigma^0 v\right\rangle = \exp\left(a_0 + a_1 T_9^{-1} + a_2 T_9^{-1/3} + a_3 T_9^{1/3} + a_4 T_9 + a_5 T_9^{5/3} + a_6 \ln\left(T_9\right)\right), \tag{66}$$

where a_0–a_6 are the parameters and T_9 the stellar temperature given in 10^9 K. This parameterization was shown to be good enough to fit the different

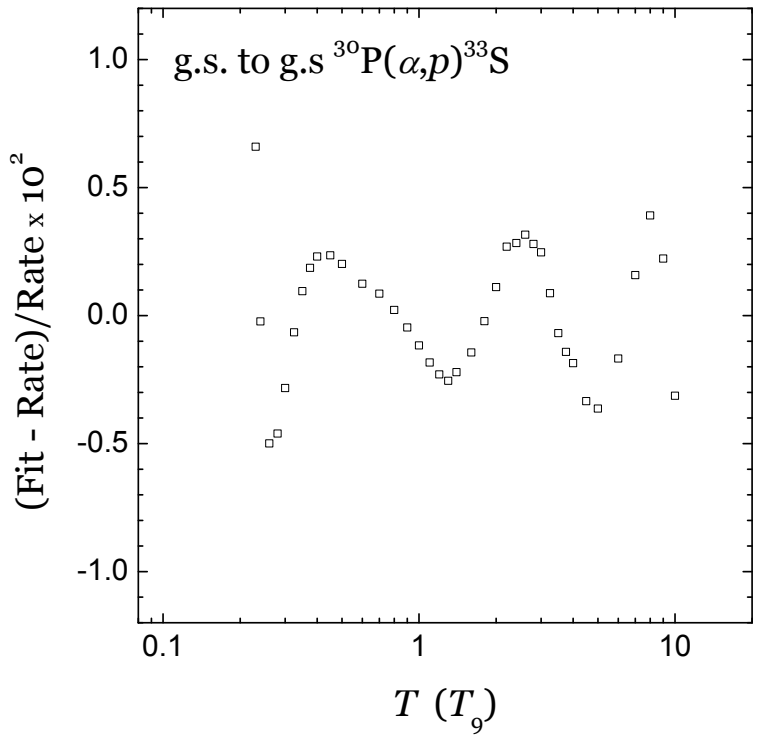

FIG. 38: Plot of the percent difference between the fit and g.s. to g.s. ^{30}P(α,p)^{33}S reaction rate $\langle\sigma^0 v\rangle$ shown in Fig. 37. The percent difference is lower than 0.64% for all the energy range where the reaction rate was calculated.

temperature dependence for various reaction types in the temperature region $0.01 \lesssim T_9 \lesssim 10$ [59]. The fit is shown in Fig. 37 by the solid line, and the obtained parameters are summarized in Table X. The percent difference between the parameterization and the reaction rate at each energy is plotted in Fig. 38 and, as can be seen, a maximum percent difference of only 0.64% was obtained.

VI.1.2. Stellar reaction rate

The g.s. to g.s. reaction rate $\langle\sigma^0 v\rangle$ is only a lower limit to the stellar reaction rate $\langle\sigma^* v\rangle$, because contributions from i) transitions from the g.s. of the initial

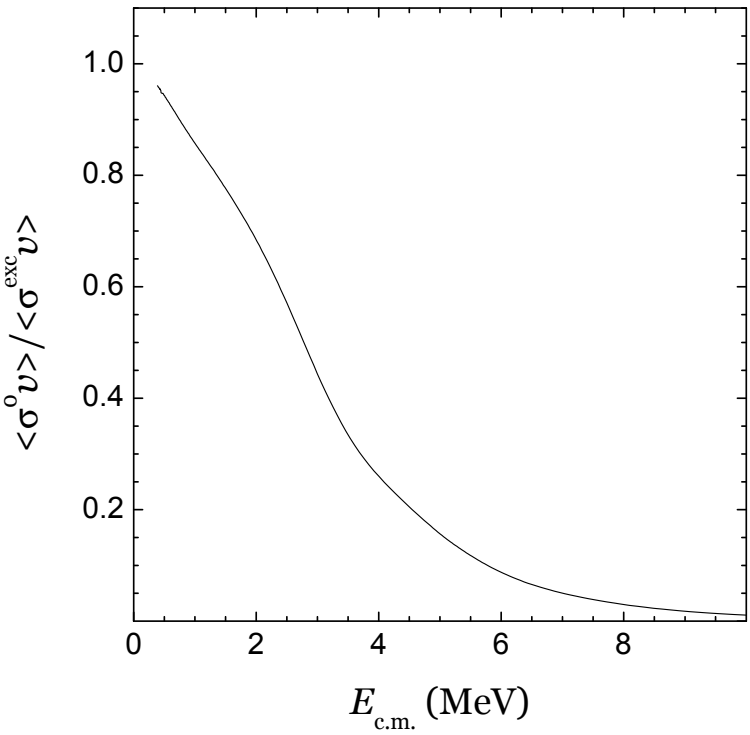

FIG. 39: SMARAGD calculation of the ratio between the reaction rate σ^0, which only includes g.s. to g.s. transitions, and the reaction rate σ^{exc}, which includes transitions from the g.s. in the initial nucleus ^{30}P to any state in the final nucleus ^{33}S.

nucleus ^{30}P to excited states in the final nucleus ^{33}S (i.e., transitions $0 \rightarrow m$, where $m = 1, 2, 3, ...$) and *ii*) transitions from excited states in ^{30}P produced in the star due to thermal excitation to any state in ^{33}S (i.e., transitions $m \rightarrow n$, where $m = 1, 2, 3, ...$, and $n = 0, 1, 2, ...$) have not been included.

The first contribution can be estimated using SMARAGD calculations of the ratio between the g.s. to g.s. cross section σ^0 and the cross section including transitions from the g.s. to any state in ^{33}S, $\sigma^{\rm exc}$. This ratio $\sigma^0/\sigma^{\rm exc}$ is shown in Fig. 39 and was used to determined $\sigma^{\rm exc}$ from σ^0. Hence, the reaction rate $\langle \sigma^{\rm exc} v \rangle$ was calculated.

The second contribution can be obtained by means of the stellar enhancement factor f, which is defined as [59, 118]

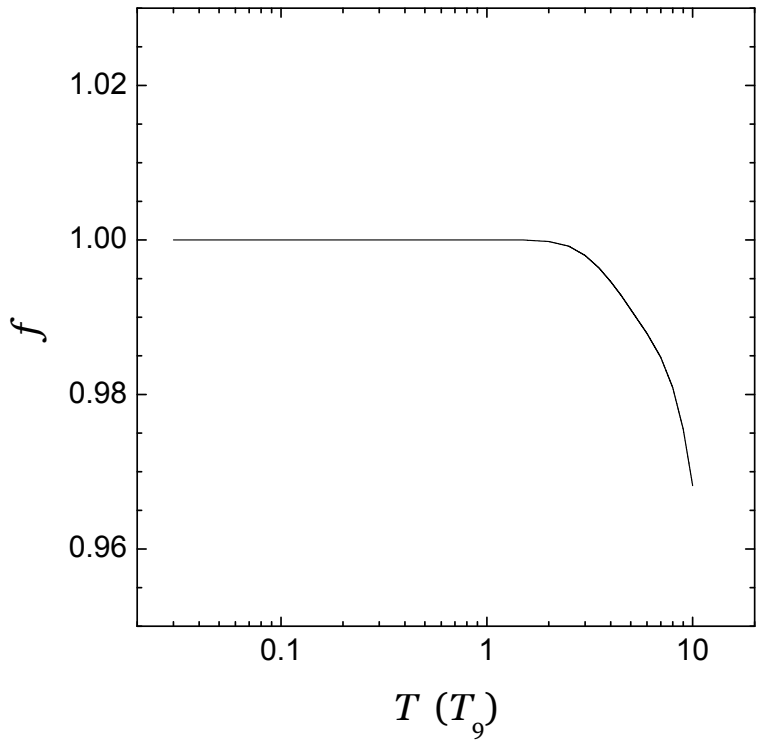

FIG. 40: Stellar enhancement factor as a function of the temperature used to obtain the ^{30}P(α,p)^{33}S stellar reaction rate.

$$f = \frac{\langle \sigma^* v \rangle}{\langle \sigma^{\rm exc} v \rangle} \,. \tag{67}$$

The stellar enhancement factor is a function of temperature and can be theoretically calculated from the partition function of the initial nucleus. Hundreds of stellar enhancement factors for neutron-, proton- and α-particle- induced reaction rates are tabulated in Ref. [59]. The f corresponding to the ^{30}P(α,p)^{33}S reaction rate, shown in Fig. 40, was obtained by request from one of the authors [112].

The ^{30}P(α,p)^{33}S stellar reaction rate $\langle \sigma^* v \rangle$ is plotted against the temperature in Fig. 41. A fit using the parameterization of Eq. 66 was carried out. This fit, 68.3% C.L. confidence bands and the theoretical SMARAGD prediction are also

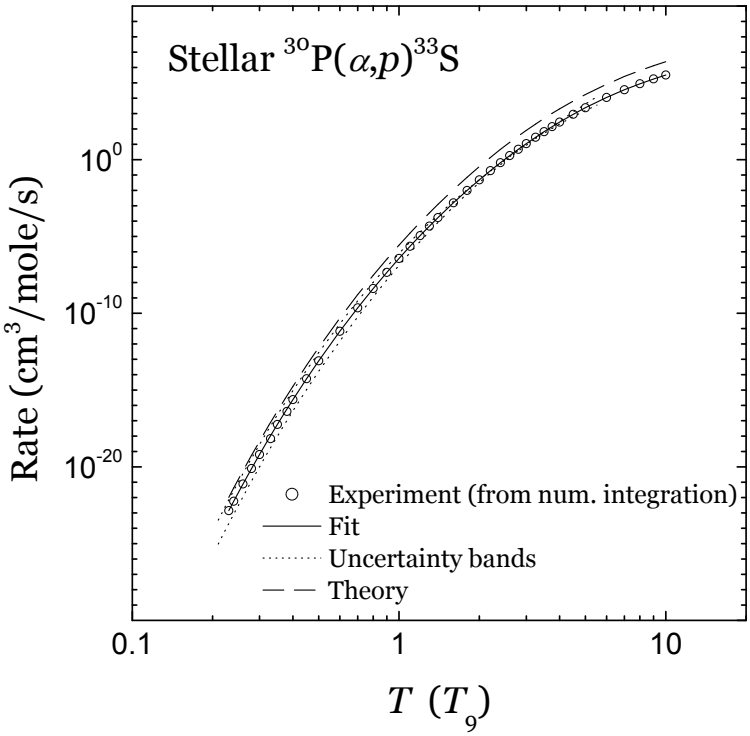

FIG. 41: Temperature dependence of the ^{30}P(α,p)^{33}S stellar reaction rate $\langle\sigma^* v\rangle$ (circles) obtained from the stellar enhancement factor f and cross section including transitions from the g.s. to any state in ^{33}S, $\sigma^{\rm exc}$. A fit using the parameterization of Eq. X (solid line), 68.3% C.L. confidence limits (dotted lines) and the theoretical SMARAGD prediction (dashed line) are shown. The temperature range where the calculations were performed includes the X-ray burst temperatures of interest.

shown in Fig. 41 and the fit parameters are given in Table XI.

Assuming a relative systematic uncertainty of 10% for the theoretical factors $\sigma^0/\sigma^{\rm exc}$ and f, the contribution of each of them, independently, to the relative systematic uncertainty of the stellar reaction rate is also 10%. Another contribution to the relative systematic uncertainty of 15% has to be taken into account due to the systematic uncertainty of the g.s. to g.s. cross section. Adding these three contributions to the systematic uncertainty of the stellar ^{30}P(α,p)^{33}S reaction rate in quadrature, an overall systematic uncertainty of 20% is obtained.

TABLE XI: Parameters of the fit to the stellar ^{30}P(α,p)^{33}S reaction rate $\langle\sigma^* v\rangle$ shown in Fig. 41, which was performed using as fitting function the parameterization given in Eq. 66.

a_0	0.369778 $\times 10^2$
a_1	-0.153516 $\times 10^0$
a_2	-0.669789 $\times 10^2$
a_3	0.171694 $\times 10^2$
a_4	-0.199580 $\times 10^1$
a_5	0.126294 $\times 10^0$
a_6	-0.699856 $\times 10^1$

This experimentally constrained stellar reaction rate should be used instead of the purely theoretical one as an input for future X-ray burst nucleosynthesis calculations.

VII. CONCLUSION

In this work, the $^{30}\mathrm{P}(\alpha,p)^{33}\mathrm{S}$ reaction has been studied for the first time. This reaction is part of the αp-process, which along with the triple-α reaction and the rapid proton capture process are the mechanisms by which the nuclear flow is driven toward the proton drip line in X-ray burst nucleosynthesis. For the measurement of the (α,p) reaction a novel method based on the gas-filled magnet technique was developed. In this method the collisions are studied in inverse kinematics, and therefore can also be used in experiments involving radioactive beams for measuring reactions with short-lived nuclei in both the entrance and exit channels.

Through a series of measurements using stable and radioactive ion beams, a parameterization of the average charge state $\bar{q}$ has been determined for ions moving through a magnetic field region filled with nitrogen gas which is valid in the mass $A \sim 20$–40 region. Using this parameterization in a RAYTRACE-GFM calculation, the motion of intermediate-mass ions in a gas-filled split pole spectrograph can be quantitatively described. The ability of the gas-filled magnet technique to separate the (p,α) reaction products from the beam particles has been established through measurements with $^{33}\mathrm{S}$ and $^{37}\mathrm{K}$ beams incident on a CH_2 target. The medium-mass reaction products and the correlated light particles were detected in coincidence by the focal plane detector of the gas-filled spectrograph and by an annular double-sided Si detector, respectively. This

method can be applied successfully to the identification of (p, α) reactions in the mass 20–40 range and, by means of the reciprocity theorem, to the measurement of cross sections for the time-reverse (α, p) reactions. Since the GFM method, however, is not independent of the velocity of the ion (i.e., it is not fully velocity focusing) there can still be considerable overlap between different particle species, which limits the general application of this technique to other fields.

This method was also used for measuring cross sections of the $^{33}\mathrm{S}(p, \alpha)^{30}\mathrm{P}$ reaction in the energy range $E_{\mathrm{c.m.}} = 4.35$–5.91 MeV. By means of the reciprocity theorem, cross sections of the time-reverse $^{30}\mathrm{P}(\alpha, p)^{33}\mathrm{S}$ reaction, relevant to X-ray burst nucleosynthesis models, were obtained in the energy range $E_{\mathrm{c.m.}} = 2.83$–4.38 MeV and compared with Hauser-Feshbach calculations. It was found that the theoretical results overestimate the experimentally determined cross sections by a factor of around 7–8. From the measured cross sections, and using an extrapolation to lower energies based on a renormalization of the theoretical result by a factor 0.137, the stellar reaction rate was calculated as a function of temperature at the relevant range in X-ray bursts of around 0.1–10 GK. The experimentally determined stellar rate was found to be a factor of approximately 7–8 smaller than the theoretical result that was previously used as input in X-ray burst nucleosynthesis nucleosynthesis models. This result may also increase the yield of $^{30}\mathrm{Si}$ by a factor of around 20, $^{31}\mathrm{P}$ by a factor of around 2, and decrease the yield of $^{33}\mathrm{S}$ by a factor of around 4, and $^{36}\mathrm{Cl}$ by a factor of around 3.

Of particular importance for studying (α, p) reactions that require radioactive ions beams, the method developed in this work has since been employed at Argonne National Laboratory to measure cross sections for the (α, p) reaction on the waiting point nucleus $^{30}\mathrm{S}$ (i. e., the $^{30}\mathrm{S}(\alpha, p)^{33}\mathrm{Cl}$ reaction) [119]. Other (α, p) reactions involving possible waiting point nuclei, such as the $^{22}\mathrm{Mg}(\alpha, p)^{25}\mathrm{Al}$,

^{26}Si$(\alpha, p)^{29}$P and ^{34}Ar$(\alpha, p)^{37}$K reactions, are currently being investigated [120].

APPENDICES

APPENDIX A: Angular distributions of differential cross sections for the ^{33}S$(p,\alpha)^{30}$P reaction

Measured angular distributions of differential cross sections for the ^{33}S$(p,\alpha)^{30}$P reaction in the center-of-mass frame of reference, $d\sigma/d\Omega_{\rm c.m.}(\theta_{\rm c.m.})$, (shown in Fig. 32 of Sec. V.4.2) are given in Tables XII–XVI in this appendix at each of the five ^{33}S laboratory energies studied in this work: (146.6 ± 3.4), (157.6 ± 3.3), (167.9 ± 3.2), (175.9 ± 3.1) and (199.1 ± 2.9) MeV. The energy intervals represent where differential cross sections were experimentally averaged due to energy loss in the target. Values of the limits of the statistical 68.3% C.L. confidence intervals for the differential cross section ($d\sigma/d\Omega_{\rm c.m.}$ 68.3% C.L. limits) and angular limits that each ring spanned during the experiment, i.e., the limits of intervals where differential cross sections were experimentally averaged ($\theta_{\rm c.m.}$ integration limits) are also given.

APPENDIX B: Theoretical ^{30}P$(\alpha,p)^{33}$S cross sections

Theoretical ^{30}P$(\alpha,p)^{33}$S cross sections for g.s. to g.s. transition calculated using SMARAGD code (shown in Fig. 35 of Sec. V.5) are given in Table XVII of this appendix.

TABLE XII: Angular distribution of cross sections for the $^{33}\mathrm{S}(p,\alpha)^{30}\mathrm{P}$ reaction in the center-of-mass frame of reference, measured in this work at a laboratory energy of (146.6 ± 3.4) MeV, equivalent to $E_{\mathrm{c.m.}} = (4.35 \pm 0.10)$ MeV.

$\theta_{\mathrm{c.m.}}$ (deg)	$d\sigma/d\Omega_{\mathrm{c.m.}}$ (mb/sr)	$\theta_{\mathrm{c.m.}}$ integration limits (deg)		$d\sigma/d\Omega_{\mathrm{c.m.}}$ 68.3% C.L. limits (mb/sr)	
		lower	upper	lower	upper
38.8	0.0016	37.0	40.6	0.0006	0.0028
42.8	0.0017	40.6	44.9	0.0010	0.0028
47.7	0.00090	44.9	50.5	0.00033	0.0016
55.3	0.00034	50.5	60.1	0.00012	0.00072
80.7	0.00000	74.9	86.5	0.00000	0.00015
90.2	0.00033	86.5	94.0	0.00012	0.00069
97.1	0.00078	94.0	100.3	0.00046	0.0013
103.1	0.00000	100.3	105.9	0.00000	0.00029
108.5	0.00024	105.9	111.1	0.00009	0.00067
113.6	0.00054	111.1	116.0	0.00020	0.0011
118.4	0.00029	116.0	120.8	0.00011	0.00080
123.1	0.00032	120.8	125.4	0.00012	0.00087
127.6	0.00068	125.4	129.8	0.00025	0.0015
132.0	0.00000	129.8	134.2	0.00000	0.00048
136.4	0.00000	134.2	138.5	0.00000	0.00053
140.6	0.00045	138.5	142.7	0.00017	0.0012
144.8	0.00000	142.7	146.9	0.00000	0.00065
149.0	0.0011	146.9	151.1	0.0004	0.0030

TABLE XIII: Angular distribution of cross sections for the $^{33}\mathrm{S}(p,\alpha)^{30}\mathrm{P}$ reaction in the center-of-mass frame of reference, measured in this work at a laboratory energy of (157.6 ± 3.3) MeV, equivalent to $E_{\mathrm{c.m.}} = (4.67 \pm 0.10)$ MeV.

$\theta_{\mathrm{c.m.}}$ (deg)	$d\sigma/d\Omega_{\mathrm{c.m.}}$ (mb/sr)	$\theta_{\mathrm{c.m.}}$ integration limits (deg)		$d\sigma/d\Omega_{\mathrm{c.m.}}$ 68.3% C.L. limits (mb/sr)	
		lower	upper	lower	upper
34.0	0.0076	32.5	35.5	0.0048	0.012
37.2	0.0066	35.5	38.9	0.0046	0.0094
40.8	0.0076	38.9	42.7	0.0054	0.010
45.1	0.0075	42.7	47.5	0.0056	0.0096
50.9	0.0023	47.5	54.3	0.0015	0.0032
85.1	0.0026	80.7	89.4	0.0019	0.0033
92.8	0.0024	89.4	96.2	0.0017	0.0033
99.1	0.0028	96.2	102.0	0.0020	0.0038
104.7	0.0029	102.0	107.4	0.0019	0.0039
109.9	0.0016	107.4	112.4	0.0009	0.0024
114.8	0.0020	112.4	117.2	0.0013	0.0032
119.5	0.0037	117.2	121.8	0.0025	0.0051
124.0	0.0032	121.8	126.2	0.0021	0.0045
128.4	0.0030	126.2	130.6	0.0018	0.0044
132.8	0.0051	130.6	134.9	0.0036	0.0069
137.0	0.0031	134.9	139.1	0.0020	0.0048
141.2	0.0045	139.1	143.3	0.0030	0.0064
145.3	0.0044	143.3	147.4	0.0027	0.0065
149.4	0.0084	147.4	151.5	0.0051	0.012

TABLE XIV: Angular distribution of cross sections for the $^{33}\mathrm{S}(p,\alpha)^{30}\mathrm{P}$ reaction in the center-of-mass frame of reference, measured in this work at a laboratory energy of (167.9 ± 3.2) MeV, equivalent to $E_{\mathrm{c.m.}} = (4.98 \pm 0.09)$ MeV.

$\theta_{\mathrm{c.m.}}$ (deg)	$d\sigma/d\Omega_{\mathrm{c.m.}}$ (mb/sr)	$\theta_{\mathrm{c.m.}}$ integration limits (deg)		$d\sigma/d\Omega_{\mathrm{c.m.}}$ 68.3% C.L. limits (mb/sr)	
		lower	upper	lower	upper
36.0	0.0095	34.4	37.5	0.0072	0.012
39.3	0.0076	37.5	41.1	0.0058	0.0098
43.3	0.0043	41.1	45.4	0.0031	0.0058
48.3	0.0066	45.4	51.1	0.0052	0.0079
77.1	0.0018	70.4	83.9	0.0014	0.0023
87.7	0.0038	83.9	91.5	0.0031	0.0046
94.7	0.0026	91.5	97.8	0.0019	0.0034
100.6	0.0021	97.8	103.4	0.0014	0.0029
105.9	0.0016	103.4	108.5	0.0010	0.0024
111.0	0.0033	108.5	113.4	0.0023	0.0044
115.7	0.0036	113.4	118.0	0.0026	0.0048
120.3	0.0033	118.0	122.5	0.0023	0.0044
124.7	0.0058	122.5	126.9	0.0044	0.0073
133.3	0.0068	131.2	135.4	0.0052	0.0086
137.5	0.0050	135.4	139.6	0.0037	0.0067
141.6	0.0050	139.6	143.7	0.0035	0.0067
149.8	0.0090	147.8	151.8	0.0061	0.012

TABLE XV: Angular distribution of cross sections for the $^{33}\mathrm{S}(p,\alpha)^{30}\mathrm{P}$ reaction in the center-of-mass frame of reference, measured in this work at a laboratory energy of (175.9 ± 3.1) MeV, equivalent to $E_{\mathrm{c.m.}} = (5.22 \pm 0.09)$ MeV.

$\theta_{\mathrm{c.m.}}$ (deg)	$d\sigma/d\Omega_{\mathrm{c.m.}}$ (mb/sr)	$\theta_{\mathrm{c.m.}}$ integration limits (deg)		$d\sigma/d\Omega_{\mathrm{c.m.}}$ 68.3% C.L. limits (mb/sr)	
		lower	upper	lower	upper
38.4	0.018	36.7	40.1	0.015	0.022
42.1	0.016	40.1	44.1	0.013	0.019
46.7	0.016	44.1	49.3	0.013	0.019
53.5	0.013	49.3	57.7	0.011	0.015
80.6	0.015	75.5	85.7	0.013	0.016
89.3	0.022	85.7	92.8	0.019	0.024
95.8	0.017	92.8	98.8	0.015	0.019
101.5	0.016	98.8	104.2	0.014	0.018
106.7	0.024	104.2	109.3	0.021	0.027
111.6	0.017	109.3	114.0	0.015	0.020
116.3	0.017	114.0	118.6	0.015	0.020
120.8	0.018	118.6	123.1	0.015	0.021
125.2	0.018	123.1	127.4	0.015	0.021
129.5	0.020	127.4	131.6	0.016	0.023
133.7	0.016	131.6	135.8	0.013	0.019
137.8	0.025	135.8	139.9	0.021	0.029
141.9	0.016	139.9	144.0	0.013	0.019
146.0	0.016	144.0	148.0	0.012	0.019
150.0	0.029	148.0	152.0	0.023	0.036

TABLE XVI: Angular distribution of cross sections for the $^{33}\mathrm{S}(p,\alpha)^{30}\mathrm{P}$ reaction in the center-of-mass frame of reference, measured in this work at a laboratory energy of (199.1 ± 2.9) MeV, equivalent to $E_{\mathrm{c.m.}} = (5.91 \pm 0.09)$ MeV.

$\theta_{\mathrm{c.m.}}$ (deg)	$d\sigma/d\Omega_{\mathrm{c.m.}}$ (mb/sr)	$\theta_{\mathrm{c.m.}}$ integration limits (deg)		$d\sigma/d\Omega_{\mathrm{c.m.}}$ 68.3% C.L. limits (mb/sr)	
		lower	upper	lower	upper
33.3	0.11	32.0	34.7	0.09	0.13
36.3	0.15	34.7	37.8	0.13	0.17
39.6	0.15	37.8	41.4	0.13	0.17
43.5	0.15	41.4	45.6	0.14	0.17
48.5	0.083	45.6	51.4	0.074	0.093
92.5	0.085	89.4	95.6	0.077	0.093
98.4	0.079	95.6	101.1	0.071	0.087
103.6	0.083	101.1	106.2	0.074	0.092
108.6	0.077	106.2	110.9	0.068	0.086
113.2	0.080	110.9	115.5	0.070	0.089
117.7	0.070	115.5	119.9	0.061	0.079
122.1	0.083	119.9	124.2	0.072	0.093
126.3	0.090	124.2	128.4	0.079	0.10
130.5	0.096	128.4	132.5	0.084	0.11
134.6	0.11	132.5	136.6	0.10	0.12
138.6	0.13	136.6	140.6	0.12	0.15
142.6	0.095	140.6	144.6	0.082	0.11
146.6	0.069	144.6	148.6	0.057	0.081
150.5	0.091	148.6	152.5	0.074	0.11

TABLE XVII: Theoretical ^{30}P(α,p)^{33}S cross sections for g.s. to g.s. transition calculated using SMARAGD code.

E_{cm} (MeV)	σ (b)	E_{cm} (MeV)	σ (b)	E_{cm} (MeV)	σ (b)	E_{cm} (MeV)	σ (b)	E_{cm} (MeV)	σ (b)	E_{cm} (MeV)	σ (b)	E_{cm} (MeV)	σ (b)	E_{cm} (MeV)	σ (b)	E_{cm} (MeV)	σ (b)	E_{cm} (MeV)	σ (b)	E_{cm} (MeV)	σ (b)
0.3865	1.60E-27	0.4815	1.15E-24	0.6518	6.77E-19	0.927	2.64E-14	1.412	6.76E-10	2.264	3.82E-06	3.763	0.00173	4.927	0.0109	5.304	0.0140	6.251	0.0175	8.631	0.0105
0.3887	2.06E-27	0.4859	1.32E-23	0.6601	1.03E-18	0.942	4.03E-14	1.438	9.89E-10	2.309	5.16E-06	3.842	0.00208	4.936	0.0110	5.328	0.0142	6.311	0.0175	8.780	0.0100
0.3910	2.66E-27	0.4950	2.20E-23	0.6686	1.56E-18	0.957	6.14E-14	1.464	1.44E-09	2.356	6.94E-06	3.923	0.00249	4.946	0.0111	5.352	0.0143	6.372	0.0175	8.934	0.00940
0.3933	3.44E-27	0.4998	2.66E-23	0.6773	2.36E-18	0.972	9.35E-14	1.491	2.10E-09	2.403	9.28E-06	4.006	0.00296	4.956	0.0111	5.377	0.0145	6.435	0.0175	9.093	0.00884
0.3957	4.47E-27	0.5095	8.96E-23	0.6862	3.59E-18	0.988	1.42E-13	1.518	3.06E-09	2.451	1.24E-05	4.091	0.00350	4.966	0.0112	5.404	0.0147	6.501	0.0174	9.259	0.00829
0.3982	5.83E-27	0.5146	1.65E-22	0.6952	5.47E-18	1.004	2.16E-13	1.546	4.43E-09	2.500	1.64E-05	4.178	0.00411	4.977	0.0113	5.431	0.0149	6.570	0.0174	9.431	0.00775
0.4007	7.62E-27	0.5250	3.10E-22	0.7045	8.33E-18	1.020	3.28E-13	1.575	6.40E-09	2.551	2.17E-05	4.267	0.00480	4.989	0.0114	5.459	0.0151	6.641	0.0173	9.609	0.00720
0.4033	1.00E-26	0.5304	5.13E-22	0.7140	1.27E-17	1.037	4.98E-13	1.604	9.22E-09	2.603	2.85E-05	4.358	0.00556	5.000	0.0115	5.488	0.0152	6.715	0.0172	9.795	0.00668
0.4059	1.32E-26	0.5360	7.52E-22	0.7237	1.94E-17	1.054	7.54E-13	1.635	1.32E-08	2.655	3.73E-05	4.450	0.00638	5.012	0.0116	5.519	0.0154	6.791	0.0171	9.987	0.00616
0.4086	1.74E-26	0.5416	1.06E-21	0.7337	2.96E-17	1.071	1.14E-12	1.665	1.90E-08	2.709	4.86E-05	4.545	0.00727	5.025	0.0117	5.550	0.0156	6.870	0.0169	10.19	0.00565
0.4113	2.31E-26	0.5474	1.63E-21	0.7439	4.52E-17	1.089	1.72E-12	1.697	2.71E-08	2.765	6.30E-05	4.643	0.00822	5.038	0.0119	5.583	0.0158	6.953	0.0167	10.39	0.00516
0.4141	3.08E-26	0.5533	2.38E-21	0.7543	6.91E-17	1.108	2.60E-12	1.729	3.86E-08	2.821	8.13E-05	4.742	0.00920	5.052	0.0120	5.617	0.0160	7.038	0.0165	10.61	0.00468
0.4170	4.11E-26	0.5594	3.54E-21	0.7649	1.06E-16	1.126	3.91E-12	1.762	5.48E-08	2.879	1.04E-04	4.832	0.0101	5.066	0.0121	5.652	0.0161	7.127	0.0162	10.83	0.00422
0.4199	5.51E-26	0.5655	5.24E-21	0.7758	1.62E-16	1.145	5.88E-12	1.795	7.75E-08	2.938	1.33E-04	4.839	0.0102	5.080	0.0122	5.689	0.0163	7.219	0.0159	11.06	0.00378
0.4229	7.41E-26	0.5719	7.77E-21	0.7869	2.47E-16	1.165	8.83E-12	1.830	1.09E-07	2.999	1.69E-04	4.844	0.0102	5.095	0.0123	5.727	0.0164	7.314	0.0156	11.30	0.00337
0.4260	9.99E-26	0.5783	1.16E-20	0.7983	3.78E-16	1.185	1.32E-11	1.865	1.54E-07	3.061	2.14E-04	4.850	0.0102	5.111	0.0125	5.766	0.0165	7.413	0.0153	11.55	0.00298
0.4292	1.35E-25	0.5850	1.72E-20	0.8099	5.79E-16	1.205	1.98E-11	1.901	2.16E-07	3.124	2.70E-04	4.856	0.0103	5.127	0.0126	5.807	0.0167	7.515	0.0149	11.81	0.00261
0.4324	1.84E-25	0.5917	2.57E-20	0.8218	8.86E-16	1.226	2.95E-11	1.938	3.01E-07	3.189	3.38E-04	4.863	0.0103	5.144	0.0127	5.850	0.0168	7.622	0.0145	12.07	0.00228
0.4357	2.51E-25	0.5987	3.85E-20	0.8340	1.36E-15	1.248	4.40E-11	1.975	4.19E-07	3.255	4.21E-04	4.870	0.0104	5.162	0.0129	5.894	0.0169	7.733	0.0141		
0.4390	3.43E-25	0.6058	5.77E-20	0.8465	2.07E-15	1.270	6.54E-11	2.014	5.81E-07	3.323	5.23E-04	4.877	0.0105	5.180	0.0130	5.939	0.0170	7.847	0.0136		
0.4425	4.71E-25	0.6130	8.66E-20	0.8592	3.17E-15	1.292	9.71E-11	2.053	8.03E-07	3.392	6.46E-04	4.885	0.0105	5.199	0.0132	5.987	0.0171	7.966	0.0131		
0.4460	7.09E-32	0.6204	1.30E-19	0.8723	4.85E-15	1.315	1.44E-10	2.094	1.11E-06	3.463	7.94E-04	4.893	0.0106	5.218	0.0133	6.036	0.0172	8.090	0.0126		
0.4496	2.26E-32	0.6280	1.96E-19	0.8856	7.42E-15	1.339	2.12E-10	2.135	1.52E-06	3.535	9.71E-04	4.901	0.0107	5.238	0.0135	6.087	0.0173	8.218	0.0121		
0.4648	3.56E-33	0.6358	2.96E-19	0.8992	1.13E-14	1.362	3.13E-10	2.177	2.07E-06	3.609	0.00118	4.909	0.0107	5.260	0.0137	6.140	0.0174	8.350	0.0116		
0.4772	3.11E-24	0.6437	4.47E-19	0.9132	1.73E-14	1.387	4.61E-10	2.220	2.82E-06	3.685	0.00144	4.918	0.0108	5.281	0.0138	6.195	0.0174	8.488	0.0111		

REFERENCES

[1] E. M. Burbidge, G. R. Burbidge, W. A. Fowler, and F. Hoyle, Rev. Mod. Phys. **29**, 547 (1957).

[2] Committee on The Physics of The Universe, Board on Physics and Astronomy, Division on Engineering and Physical Sciences, & National Research Council of The National Academies , ed., *Connecting Quarks with the Cosmos: Eleven Science Questions for the New Century* (National Academies Press, Washington, 2003).

[3] M. Aliotta, Eur. Phys. J. Special Topics **150**, 201 (2007).

[4] H. Schatz and K. Rehm, Nucl. Phys. A **777**, 601 (2006).

[5] A. Parikh, J. José, F. Moreno, and C. Iliadis, Astrophys. J. Suppl. Ser. **178**, 110 (2008).

[6] J. L. Fisker, H. Schatz, and F.-K. Thielemann, Astrophys. J. Suppl. Ser. **174**, 261 (2008).

[7] W. H. G. Lewin, J. van Paradijs, and R. E. Taam, Space Sci. Rev. **62**, 223 (1993).

[8] J. van Paradijs and W. Lewin, in *Flares and Flashes*, Lecture Notes in Physics, Vol. 454, edited by J. Greiner, H. Duerbeck, and R. Gershberg (Springer Berlin/Heidelberg, 1995) pp. 307–318.

[9] W. H. G. Lewin, J. van Paradijs, and R. E. Taam, *X-ray Binaries* (Cambridge University Press, Cambridge, 1997).

[10] T. E. Strohmayer and L. Bildsten, *Compact Stellar X-ray Sources*, edited by W. H. G. Lewin and M. van der Klies (Cambridge University Press, Cambridge,

2003) pp. 113–156, arXiv:astro-ph/0301544v2.

[11] J. Isern, M. Hernanz, and J. José, in *Astronomy with Radioactivities*, Lecture Notes in Physics, Vol. 812, edited by R. Diehl, D. H. Hartmann, & N. Prantzos (Berlin Springer Verlag, 2011) pp. 233–308.

[12] R. D. Belian, J. P. Conner, and W. D. Evans, Astrophys. J. Lett. **206**, L135 (1976).

[13] J. Grindlay, H. Gursky, H. Schnopper, D. R. Parsignault, J. Heise, A. C. Brinkman, and J. Schrijver, Astrophys. J. Lett. **205**, L127 (1976).

[14] W. H. G. Lewin, G. Clark, and J. Doty, IAU Circ. **2922**, 1 (1976).

[15] Q. Z. Liu, J. van Paradijs, and E. P. J. van den Heuvel, Astron. Astrophys. **469**, 807 (2007), arXiv:0707.0544.

[16] S. E. Woosley and R. E. Taam, Nature **263**, 101 (1976).

[17] L. Maraschi and A. Cavaliere, in *X-ray Binaries and Compact Objects*, Highlights of Astronomy, Vol. 4, edited by K. A. van der Hucht (Dordrecht, D. Reidel Publishing Co., Boston, 1977) pp. 127–128.

[18] J. A. Hoffman, H. L. Marshall, and W. H. G. Lewin, Nature **271**, 630 (1978).

[19] J. van Paradijs, VizieR Online Data Catalog **5090**, 0 (1997).

[20] J. van Paradijs and M. van der Klis, "Low mass X-ray binaries," in *The Century of Space Science, Volume I*, edited by J. A. Bleeker, J. Geiss, and M. C. E. Huber (Kluwer Academic Publishers, 2002) p. 811.

[21] W. Pietsch and F. Haberl, Astron. Astrophys. **430**, L45 (2005), arXiv:astro-ph/0412373.

[22] C. E. Rolfs and W. S. Rodney, *Cauldrons in the cosmos* (University of Chicago Press, Chicago, 1988).

[23] C. J. Hansen and H. M. van Horn, Astrophys. J. **195**, 735 (1975).

[24] R. E. Taam, S. E. Woosley, T. A. Weaver, and D. Q. Lamb, Astrophys. J. **413**, 324 (1993).

[25] L. Bildsten and E. F. Brown, Astrophys. J. **477**, 897 (1997).

[26] H. Schatz, L. Bildsten, A. Cumming, and M. Wiescher, Astrophys. J. **524**, 1014 (1999).

[27] E. Kuulkers, J. J. M. in't Zand, M. H. van Kerkwijk, R. Cornelisse, D. A. Smith, J. Heise, A. Bazzano, M. Cocchi, L. Natalucci, and P. Ubertini, Astron. Astrophys. **382**, 503 (2002), arXiv:astro-ph/0111261.

[28] E. Kuulkers, P. R. den Hartog, J. J. M. in't Zand, F. W. M. Verbunt, W. E. Harris, and M. Cocchi, Astron. Astrophys. **399**, 663 (2003), arXiv:astro-ph/0212028.

[29] D. K. Galloway, M. P. Muno, J. M. Hartman, D. Psaltis, and D. Chakrabarty, Astrophys. J. Suppl. Ser. **179**, 360 (2008), arXiv:astro-ph/0608259.

[30] J. H. Swank, R. H. Becker, E. A. Boldt, S. S. Holt, S. H. Pravdo, and P. J. Serlemitsos, Astrophys. J. Lett. **212**, L73 (1977).

[31] J. A. Hoffman, W. H. G. Lewin, and J. Doty, Astrophys. J. Lett. **217**, L23 (1977).

[32] R. A. London, W. M. Howard, and R. E. Taam, Astrophys. J. Lett. **287**, L27 (1984).

[33] R. A. London, R. E. Taam, and W. M. Howard, Astrophys. J. **306** (1986).

[34] T. Ebisuzaki and N. Nakamura, Astrophys. J. **328**, 251 (1988).

[35] J. Madej, Astrophys. J. **376**, 161 (1991).

[36] L. Titarchuk, Astrophys. J. **429**, 340 (1994).

[37] H. Schatz, A. Aprahamian, J. Görres, M. Wiescher, T. Rauscher, J. Rembges, F.-K. Thielemann, B. Pfeiffer, P. Möller, K.-L. Kratz, H. Herndl, B. Brown,

and H. Rebel, Phys. Rep. **294**, 167 (1998).

[38] H. Schatz, A. Aprahamian, V. Barnard, L. Bildsten, A. Cumming, M. Ouellette, T. Rauscher, F.-K. Thielemann, and M. Wiescher, Phys. Rev. Lett. **86**, 3471 (2001).

[39] S. E. Woosley, A. Heger, A. Cumming, R. D. Hoffman, J. Pruet, T. Rauscher, J. L. Fisker, H. Schatz, B. A. Brown, and M. Wiescher, Astrophys. J. Suppl. Ser. **151**, 75 (2004).

[40] J. José and F. Moreno, Proc. of Sci. **PoS(NIC-IX)123**, in *Proceedings of the 9th International Symposium on Nuclei in the Cosmos, CERN, Geneva, Switzerland, 2006.*

[41] C. Iliadis, *Nuclear Physics of Stars* (Wiley-VCH Verlag, Weinheim, 2007).

[42] J. José, F. Moreno, A. Parikh, and C. Iliadis, Proc. of Sci. **PoS(NIC-XI)050** (2010), in *Proceedings of the 11th International Symposium on Nuclei in the Cosmos, Heidelberg, Germany, 2010.*

[43] J. José, F. Moreno, A. Parikh, and C. Iliadis, Astrophys. J. Suppl. Ser. **189**, 204 (2010), arXiv:1005.4767 [astro-ph.SR].

[44] J. José, J. Casanova, F. Moreno, E. Garcia-Berro, A. Parikh, and C. Iliadis, AIP Conf. Proc. **1238**, 157 (2010).

[45] E. Chaisson and S. McMillan, *Astronomy Today* (Prentice Hall, 2005).

[46] N. Grevesse and A. Sauval, Space Sci. Rev. **85**, 161 (1998).

[47] M. S. Smith, *The Onset and Breakout of the Stellar Hot Carbon Nitrogen-Oxygen Cycle*, Ph.D. thesis, Yale University (1990).

[48] M. Wiescher, J. Görres, and H. Schatz, J. Phys. G **25**, R133 (1999).

[49] M. Wiescher, G. P. A. Berg, M. Couder, J. L. Fisker, Y. Fujita, J. Görres, M. N. Harakeh, K. Hatanaka, A. Matic, W. Tan, and A. M. van den Berg, Prog. Part.

Nucl. Phys. **59**, 51 (2007).

[50] S. A. Glasner and J. W. Truran, Astrophys. J. Lett. **692**, L58 (2009), arXiv:0812.3984.

[51] R. K. Wallace and S. E. Woosley, Astrophys. J. Suppl. Ser. **45**, 389 (1981).

[52] L. van Wormer, J. Görres, C. Iliadis, M. Wiescher, and F.-K. Thielemann, Astrophys. J. **432**, 326 (1994).

[53] S. Utku, J. G. Ross, N. P. T. Bateman, D. W. Bardayan, A. A. Chen, J. Görres, A. J. Howard, C. Iliadis, P. D. Parker, M. S. Smith, R. B. Vogelaar, M. Wiescher, and K. Yildiz, Phys. Rev. C **57**, 2731 (1998).

[54] N. de Séréville, E. Berthoumieux, and A. Coc, Nucl. Phys. A **758**, 745 (2005).

[55] O. Koike, M. aki Hashimoto, R. Kuromizu, and S. ichirou Fujimoto, Astrophys. J. **603**, 242 (2004).

[56] C. Angulo, M. Arnould, M. Rayet, P. Descouvemont, D. Baye, C. Leclercq-Willain, A. Coc, S. Barhoumi, P. Aguer, C. Rolfs, R. Kunz, J. Hammer, A. Mayer, T. Paradellis, S. Kossionides, C. Chronidou, K. Spyrou, S. Degl'Innocenti, G. Fiorentini, B. Ricci, S. Zavatarelli, C. Providencia, H. Wolters, J. Soares, C. Grama, J. Rahighi, A. Shotter, and M. L. Rachti, Nucl. Phys. A **656**, 3 (1999).

[57] C. Iliadis, J. M. D'Auria, S. Starrfield, W. J. Thompson, and M. Wiescher, Astrophys. J. Suppl. Ser. **134**, 151 (2001).

[58] G. Audi, A. H. Wapstra, and C. Thibault, Nucl. Phys. A **729**, 337 (2003).

[59] T. Rauscher and F.-K. Thielemann, At. Data Nucl. Data Tables **75**, 1 (2000), arXiv:astro-ph/0004059v1.

[60] G. R. Satchler, *Introduction to Nuclear Reactions*, 1st ed. (The MacMillan Press Ltd., London, 1980).

[61] P. Marmier and E. Sheldon, *Physics of Nuclei and Particles* (Academic Press, New York, 1969).

[62] J. O. Fernández Niello and J. E. Testoni, *Elementos de Reacciones Nucleares* (Instituto de Tecnología Prof. J. A. Sábato, Argentina, 1997).

[63] J. M. Blatt and V. F. Weisskopf, *Theoretical Nuclear Physics* (Wiley, New York, 1952).

[64] W. Von Witsch, A. Richter, and P. Von Brentano, Phys. Rev. **169**, 923 (1968).

[65] A. Messiah, *Quantum Mechanics* (Dover, New York, 1999).

[66] G. Gamow, Zeit. Phys. **51**, 204 (1928).

[67] B. Harss, J. P. Greene, D. Henderson, R. V. F. Janssens, C. L. Jiang, J. Nolen, R. C. Pardo, K. E. Rehm, J. P. Schiffer, R. H. Siemssen, A. A. Sonzogni, J. Uusitalo, I. Wiedenhöver, M. Paul, T. F. Wang, F. Borasi, R. E. Segel, J. C. Blackmon, M. S. Smith, A. Chen, and P. Parker, Phys. Rev. Lett. **82**, 3964 (1999).

[68] A. A. Sonzogni, K. E. Rehm, I. Ahmad, F. Borasi, D. L. Bowers, F. Brumwell, J. Caggiano, C. N. Davids, J. P. Greene, B. Harss, A. Heinz, D. Henderson, R. V. F. Janssens, C. L. Jiang, G. McMichael, J. Nolen, R. C. Pardo, M. Paul, J. P. Schiffer, R. E. Segel, D. Seweryniak, R. H. Siemssen, J. W. Truran, J. Uusitalo, I. Wiedenhöver, and B. Zabransky, Phys. Rev. Lett. **84**, 1651 (2000).

[69] C. B. Fulmer and B. L. Cohen, Phys. Rev. **109**, 94 (1958).

[70] B. L. Cohen and C. B. Fulmer, Nucl. Phys. **6**, 547 (1958).

[71] P. Armbruster, Nukleonik **3**, 188 (1961).

[72] K. Sistemich, J. W. Grüter, H. Lawin, J. Eidens, R. Fabbri, T. A. Khan, W. D. Lauppe, G. Sadler, H. A. Selic, M. Shaanan, and P. Armbruster, Nucl. Instr. and Meth. **130**, 491 (1975).

[73] H. Lawin, J. Eidens, J. W. Borgs, R. Fabbri, J. W. Grüter, G. Joswig, T. A.

Khan, W. D. Lauppe, G. Sadler, H. A. Selic, M. Shaanan, K. Sistemich, and P. Armbruster, Nucl. Instr. and Meth. **137**, 103 (1976).

[74] A. Ghiorso, S. Yashita, M. E. Leino, L. Frank, J. Kalnins, P. Armbruster, J.-P. Dufour, and P. K. Lemmertz, Nucl. Instr. and Meth. A **269**, 192 (1988).

[75] V. Ninov, P. Armbruster, F. P. Heßberger, S. Hofmann, G. Münzenberg, Y. Fujita, M. Leino, and A. Lüttgen, Nucl. Instr. and Meth. A **357**, 486 (1995).

[76] M. Leino, J. Äystö, T. Enqvist, P. Heikkinen, A. Jokinen, M. Nurmia, A. Ostrowski, W. H. Trzaska, J. Uusitalo, K. Eskola, P. Armbruster, and V. Ninov, Nucl. Instr. and Meth. B **99**, 653 (1995).

[77] K. Subotic, Y. T. Oganessian, V. K. Utyonkov, Y. V. Lobanov, F. S. Abdullin, A. N. Polyakov, Y. S. Tsyganov, and O. V. Ivanov, Nucl. Instr. and Meth. A **481**, 71 (2002).

[78] M. Paul, B. G. Glagola, W. Henning, J. G. Keller, W. Kutschera, Z. Liu, K. E. Rehm, B. Schneck, and R. H. Siemssen, Nucl. Instr. and Meth. A **277**, 418 (1989).

[79] W. Henning, W. A. Bell, P. J. Billquist, B. G. Glagola, W. Kutschera, Z. Liu, H. F. Lucas, M. Paul, K. E. Rehm, and J. L. Yntema, Science **236**, 725 (1987).

[80] A. Arazi, T. Faestermann, J. O. Fernández Niello, K. Knie, G. Korschinek, M. Poutivtsev, E. Richter, G. Rugel, and A. Wallner, Phys. Rev. C **74**, 025802 (2006).

[81] C. Li, Y. Guan, S. Jiang, M. He, X. Ruan, W. Wang, D. Zhang, J. Yuan, S. Wu, and K. Dong, Nucl. Instr. and Meth. B **268**, 876 (2010), in *Proceedings of the Eleventh International Conference on Accelerator Mass Spectrometry, Rome, Italy, 2008.*

[82] U. Morgenstern, L. K. Fifield, S. G. Tims, and R. G. Ditchburn, Nucl. Instr.

and Meth. B **268**, 739 (2010), in *Proceedings of the Eleventh International Conference on Accelerator Mass Spectrometry, Rome, Italy, 2008.*

[83] K. E. Rehm, M. Paul, J. Gehring, B. Glagola, D. Henderson, W. Kutschera, and A. H. Wuosmaa, Nucl. Instr. and Meth. A **344**, 614 (1994).

[84] J. F. Liang, D. Shapira, J. R. Beene, J. D. Bierman, A. Galindo-Uribarri, J. G. del Campo, C. J. Gross, M. L. Halbert, T. J. Harding, A. I. D. Macnab, S. P. McNeal, R. L. Varner, and K. Zhao, Nucl. Instr. and Meth. A **435**, 393 (1999).

[85] C. Schmitt, M. Rejmund, A. Navin, B. Lecornu, B. Jacquot, G. de France, A. Lemasson, A. Shrivastava, P. Greenlees, J. Uusitalo, K. Subotic, L. Gaudefroy, C. Theisen, B. Sulignano, O. Dorvaux, and L. Stuttgé, Nucl. Instr. and Meth. A **621**, 558 (2010).

[86] K. E. Rehm, C. L. Jiang, M. Paul, D. Blumenthal, J. Gehring, D. Henderson, J. Nickles, J. Nolen, R. C. Pardo, A. D. Roberts, J. P. Schiffer, and R. E. Segel, Nucl. Instr. and Meth. A **370**, 438 (1996).

[87] M. Paul, Nucl. Instr. and Meth. B **52**, 315 (1990).

[88] H. D. Betz, Rev. Mod. Phys. **44**, 465 (1972).

[89] H. D. Betz, *Applied Atomic Collision Physics*, edited by S. Datz, Vol. 4 (Academic Press, Ney York, 1983) p. 1.

[90] S. B. Kowalski and H. A. Enge, RAYTRACE, MIT Internal Report (1986).

[91] S. B. Kowalski and H. A. Enge, Nucl. Instr. and Meth. A **258**, 407 (1987).

[92] H. D. Betz, G. Hortig, E. Leischner, C. Schmelzer, B. Stadler, and J. Weihrauch, Phys. Lett. **22**, 643 (1966).

[93] H. D. Betz and C. Schmelzer, Unilac Report 1-67, (1967), Universitat Heidelberg (unpublished).

[94] I. S. Dmitriev and V. S. Nikolaev, Zh. Eksperim. i Teor. Fiz. 47, 615 (1964)

[English transl.: Sov. Phys. JETP 20, 409 (1965)].

[95] G. Schiwietz and P. L. Grande, Nucl. Instr. and Meth. B **175**, 125 (2001).

[96] B. Harss, R. C. Pardo, K. E. Rehm, F. Borasi, J. P. Greene, R. V. F. Janssens, C. L. Jiang, J. Nolen, M. Paul, J. P. Schiffer, R. E. Segel, J. Specht, T. F. Wang, P. Wilt, and B. Zabransky, Rev. Sci. Instrum. **71**, 380 (2000).

[97] R. C. Pardo et al., to be published.

[98] D. M. Heimann, A. J. Pacheco, and O. A. Capurro, Nucl. Instr. and Meth. A **622**, 642 (2010).

[99] J. F. Ziegler, M. D. Ziegler, and J. P. Biersack, Nucl. Instr. and Meth. B **268**, 1818 (2010), in *Proceedings of the 19th International Conference on Ion Beam Analysis, University of Cambridge, UK, 2009*.

[100] G. J. Feldman and R. D. Cousins, Phys. Rev. D **57**, 3873 (1998).

[101] J. E. Bowcock and H. Burkhardt, Rep. Prog. Phys. **38**, 1099 (1975).

[102] E. G. Illsley, H. D. Holmgren, R. L. Johnston, and E. A. Wolicki, Phys. Rev. **107**, 538 (1957).

[103] S. M. Bharathi, U. T. Raheja, and E. Kondaiah, Nucl. Phys. **83**, 407 (1966).

[104] J. A. Niskanen, AIP Conf. Proc. **69**, 62 (1981), in *Proceedings of the Fifth International Symposium on Polarization Phenomena in Nuclear Physics, Santa Fe, USA, 1980*.

[105] S. Zhaomin and S.-Q. Xie, J. Phys. G **16**, 1283 (1990).

[106] P. E. Hodgson, Rep. Prog. Phys. **50**, 1171 (1987).

[107] T. Ericson and V. Strutinsky, Nucl. Phys. **9**, 689 (1958).

[108] A. G. Frodesen and O. Skjeggestad, *Probability and Statistics in Particle Physics* (Universitetsforlaget, Oslo, 1979).

[109] T. Rauscher, Int. J. Mod. Phys. E **20**, 1071 (2011).

[110] T. Rauscher, arXiv:1010.4283v4 [nucl-th].

[111] SMARAGD code, URL: `http://nucastro.org/smaragd.html`.

[112] T. Rauscher, "private communication".

[113] National Nuclear Data Center, NuDat 2 database, URL: `http://www.nndc.bnl.gov/nudat2/`.

[114] National Nuclear Data Center, Q-value Calculator, URL: `http://www.nndc.bnl.gov/qcalc/`.

[115] INFRASTRUCTURE code, URL: `http://www.nucastrodata.org/infrastructure.html`.

[116] M. S. Smith, E. J. Lingerfelt, J. P. Scott, C. D. Nesaraja, K. Chae, H. Koura, L. F. Roberts, W. R. Hix, D. W. Bardayan, and J. C. Blackmon, Proc. of Sci. **PoS(NIC-IX)180** (2006), in *Proceedings of the 9th International Symposium on Nuclei in the Cosmos, CERN, Geneva, Switzerland, 2006.*

[117] T. Rauscher and F.-K. Thielemann, At. Data Nucl. Data Tables **79**, 47 (2001).

[118] T. Rauscher, P. Mohr, I. Dillmann and R. Plag, arXiv:1106.1728v2.

[119] C. M. Deibel, K. E. Rehm, J. M. Figueira, J. P. Greene, C. L. Jiang, B. P. Kay, H. Y. Lee, J. C. Lighthall, S. T. Marley, R. C. Pardo, N. Patel, M. Paul, C. Ugalde, A. Woodard, A. H. Wuosmaa, and G. Zinkann, Phys. Rev. C **84**, 045802 (2011).

[120] C. M. Deibel et al., to be published.